ROMA TRE
UNIVERSITÀ DEGLI STUDI

DEPARTMENT OF ENGINEERING

DOCTORATE IN APPLIED ELECTRONICS

30TH OF DOCTORATE CYCLE

STRUCTURAL AND TRANSPORT PROPERTIES OF SUPERCONDUCTORS SUITABLE FOR NUCLEAR FUSION MAGNETS BY COMPLEMENTARY EXPERIMENTAL TECHNIQUES

Candidate *Anna Frolova*

Tutor *Prof. Enrico Silva*

Co-tutor *Dr. Nicola Pompeo*

2017-2018

To whom it may concern

Contents

List of Figures

List of Tables

Introduction

Progressive research and constant development in technology lead to an increasing variety of possible applications of High-Temperature Superconductors (HTS), which have been already successfully produced by different manufacturers for the needs of electrical utility and magnet manufacturing sectors. Although a remarkable progress in the understanding of the theoretical and practical features and mechanisms of HTS has been made, many aspects have not yet been studied well enough to be able to control the whole preparation and fabrication processes for a proper optimization of the performances. The control of the superconducting and mechanical properties of tapes and wires is necessary to establish a solid position of HTS as alternative materials with respect to Low Temperature Superconductors, especially when high-power applications are concerned. Power applications, such as nuclear fusion magnets, demand very strong vortex pinning capable to yield high values of the critical current density (J_c) in high magnetic fields (H) and low temperatures (T).

Specific issues arise for the much sought-after fusion applications. The possible scenarios related to the increase in the operation temperature (> 4.2 K) and/or in the magnetic field strength (13 - 16 T) of superconducting magnets have been long debated in the fusion community. While higher magnetic field strengths would be mainly beneficial for the physics of plasma (plasma confinement and fusion power density), higher temperatures could have a relevant technological impact due to the higher efficiency in cooling and reduction in the reactor complexity. Moreover, helium free cryocooler-driven superconducting magnet technology operating at 20 – 50 K temperature range would be of great interest as demonstrated by the present Helium shortage and recent price rises. However, in spite of this interest, up to now there is a lack of knowledge and experimental studies of the fundamental properties of HTS superconducting materials in either intermediate temperature ranges (20 – 50 K) or extreme high field conditions at 4.2 K. An increase of the magnetic field performances at the same (low) operating temperatures could lead many benefits to

nuclear fusion reactors. This can be achieved by the continuous development of REBCO-based HTS (RE = rare Earth), including $YBa_2Cu_3O_{7-x}$ (YBCO).

Another technological challenge of fusion energy is the exposure of a fusion device to nuclear radiation, particularly neutrons and gamma rays. In operational conditions further defects in a material structure are expected due to fusion neutron bombardments. That also concerns HTS superconducting films. In order to identify precisely the effect of different defects, an accurate study of the pinning properties of nonirradiated sampes is in order. Of course, before a material can be definitely assessed for a use in fusion environment, the investigation of the radiation effects will be mandatory.

This thesis summarizes a three-year experimental research consisting in the measurements and study of vortex dynamics in different regimes in YBCO with different types of second phases at low temperatures (10 – 50 K) and high magnetic fields (up to 12 T). Although the magnetic field reached in fusion environment can be higher, a preliminary assessment at fields above 10 T is a founding ground for any subsequent study and a base for the magnetic field range chosen for the present research. This work has been carried out in part at the Superconductivity Section of ENEA Research Center (Frascati) and in part at the Department of Engineering of the Roma Tre University, within the framework of the EUROfusion Consortium research project.

Two different methods were used to grow YBCO thin films with different Artificial Pinning Centres (APCs) - Pulsed Laser Deposition (PLD) and Metal Organic Decomposition (MOD) techniques. Structural studies were performed by means of Transmission Electron Microscopy (TEM). Measurements by the standard DC electric transport technique (long-range vortex motion) have been performed in a cryostat provided with a 12 T superconducting magnet. High-frequency microwave measurements (small-displacement vortex motion) were made by using the dielectric resonator technique at 47.7 GHz, which allows measuring contactless and with high sensitivity. The role of different defects in PLD films and in MOD films has been reported. Through an accurate comparison of pristine MOD film with the behaviour of a PLD grown sample with BZO addition in form of self-assembled nano-

coloumns, the effect of twin boundaries as a field and temperature dependent crossover from vortex pinning to vortex channeling has been revealed. An overall increase of the J_c in-field performances for PLD doped samples with respect to pristine YBCO is clearly observed and it indicates the efficiency of the APCs with a stronger efficiency of the BYNTO nano-columns, especially at high fields ($\mu_0 H \geq 5$ T). Consistently with DC transport properties, the high efficiency of BYNTO columns was observed in microwave data analysis. Analysis of doping in MOD derived films has shown that BZO nanoparticles mainly act as isotropic pinning centres. The increase of pinning constant $k_p(H)$ for doped MOD sample indicated stronger pinning due to a higher pinning sites density.

This thesis has been divided into 5 chapters, the contents of which are described as follows:

Chapter 1 presents a discussion of the theoretical background of superconductivity with its basic theories, and focuses on the High Temperature superconductors and flux flow dynamics, which lay at the basis of the present thesis, and its application for nuclear fusion energy.

Chapter 2 introduces the techniques used for the growth of the YBCO thin films and presents the structural investigation in these samples, including the identification of the various defects originating from the introduction of the second phases.

Chapter 3 describes the DC current transport measurement technique and presents the obtained characteristic data, such as critical temperature and the temperature dependence of resistivity, angular and in-field dependences of critical current density and pinning force density as a function of the applied magnetic field. Preliminary analysis is given for all the samples under study.

Chapter 4 describes the microwave measurement technique and analyses the microwave complex resistivity in presence of the external magnetic field taken in several pristine and second phase-doped YBCO films. Based on the field dependence of the pinning parameters derived from microwave measurements, such as the

pinning parameter r and the pinning constant k_p, the vortex pinning regimes will be discussed in this Chapter.

Chapter 5 presents the main results concerning the vortex physics. It discusses in details some selected aspects of vortex flux pinning in YBCO thin films with and without second phases: (i) the effect of pinning and channeling in MOD pristine sample and its absence on MOD YBCO with introduced APCs; (ii) the effect of different secondary phases (BZO and BYNTO) in PLD films and (iii) of different concentration of APCs (0%, 5% and 8%) in MOD films. Finally, the experimental correlation between the microwave and DC parameters has been presented among the studied samples.

Chapter 1

Superconductivity

Superconductivity is the phenomenon, exhibited by various metals, alloys, and compounds, of conducting electrical current without resistance when cooled to low temperatures. The discovery of superconductivity occurred in 1911. A Dutch Physicist, Heike Kamerlingh Onnes, measured the mercury resistivity at low temperatures [1] and observed that the resistivity dropped to zero at 4.19 K (Fig. 1.1), the so-called critical, or transition, temperature T_c. At any temperature below T_c, superconducting materials gain their unique properties. Thus, the first fundamental and characteristic property of superconductors (SC) is the zero electrical resistance below a well-defined, material-specific T_c for all practical purposes.

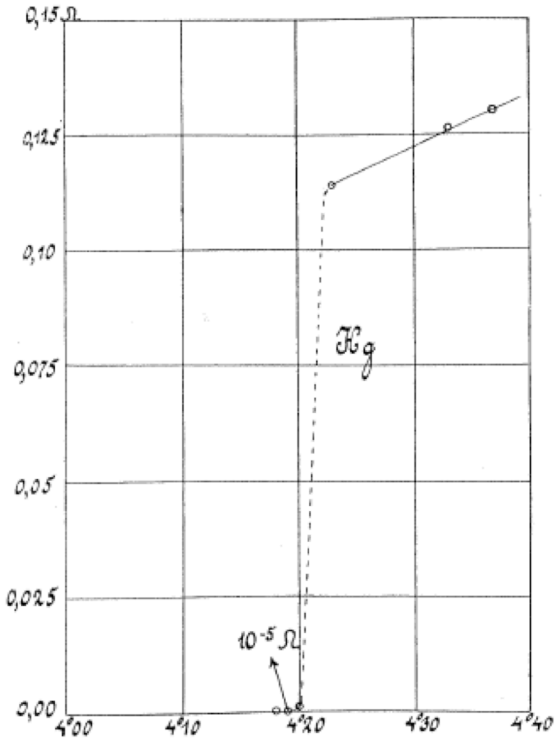

Fig. 1.1. Resistive transition of mercury, taken from [1].

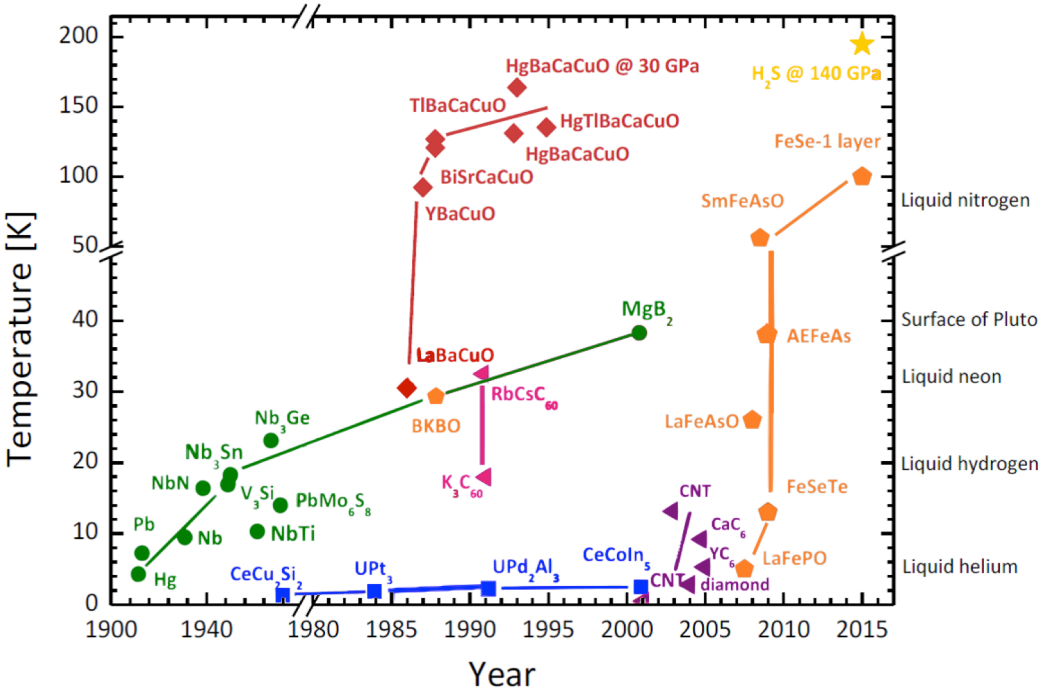

Fig. 1.2. The critical temperature T_c of superconductors plotted against the year of their discovery, taken from [2].

Since then, many metals, alloys, and compounds have been discovered to be superconducting materials with different T_c (Figure 1.2) [2]. In particular, a major discovery was made in 1986. While studying a compound produced from Lanthanum, Barium, Copper and Oxygen, Bednorz and Muller discovered that this ceramic compound could also become superconducting, and at much higher T_c than previously achieved [3]. This lead to the discovery of many more High Temperature Superconductors (HTS) over the following decades and the research into ceramic materials has thrust superconductor composites into the real world applications.

The other characteristic property of superconductors is the Meissner effect, or perfect diamagnetism (although, it was verified that it is perfect only in case of bulk materials) [4]. The Meissner effect (Figure 1.3) consists in the expulsion of the externally applied magnetic field by means of spontaneous supercurrents (currents flowing without dissipation) circulating in the surface layer. This effect indicates that the transition from the normal to superconducting state is a thermodynamic phase transition, since the flux expulsion arises irrespectively from the thermal and magnetic history. Superconductivity is destroyed by a critical magnetic field H_c,

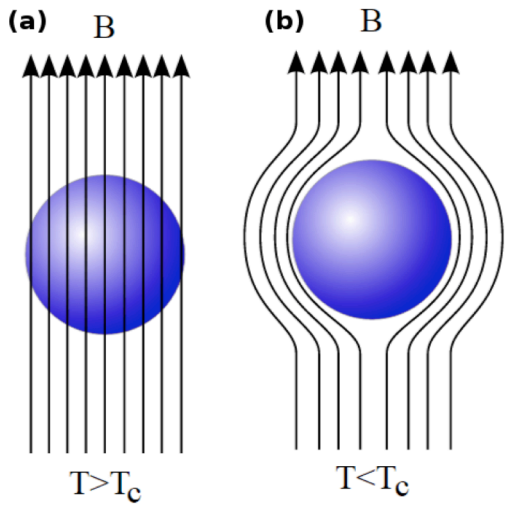

Fig. 1.3. The Meissner effect in a superconductor: (a) normal state; (b) superconducting state.

which is related thermodynamically to the free energy difference between the normal and superconducting states in zero field, the so-called condensation energy of the superconducting state. The critical field H_c above which the superconducting state disappears is dependent on the temperature: at zero temperature its maximum reaches zero at T_c in conventional superconductors, following $H_c(T) = H_c(0)(1 - (T/T_c)^2)$ [4]. In addition to T_c and H_c, the third important parameter is the critical value of the current flowing through the superconductor – critical current density J_c - above which the kinetic energy is higher than the condensation energy. All three critical

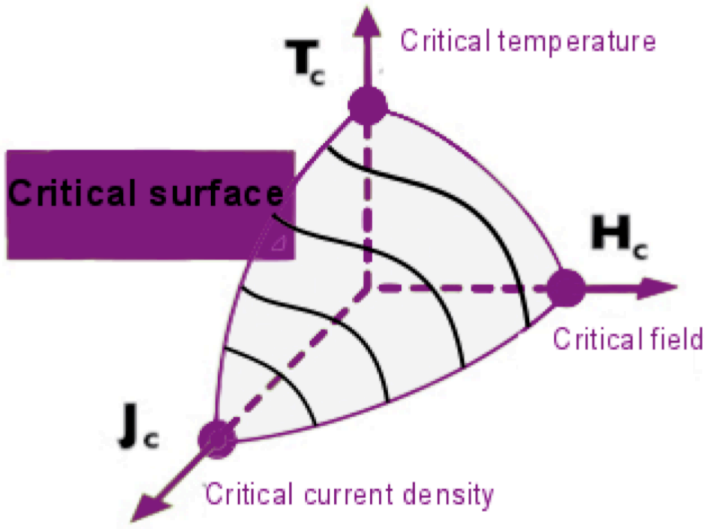

Fig. 1.4. Phase diagram with a critical surface of a superconductor.

parameters – critical temperature, critical magnetic field and critical current density – create the so-called critical surface of a superconductor. The classical schematic phase diagram is shown in Figure 1.4.

To describe the observed effects in new superconducting materials a theoretical description was needed. The first phenomenological theory was described by brothers H. and F. London in 1935; later, V. L. Ginzburg and L. D. Landau proposed a theoretical description in 1950, and in 1957 Bardeen, Cooper and Schrieffer developed their microscopic theory of superconductivity.

The following sections of this chapter briefly discuss the theoretical background of superconductivity with its basic theories, then will focus on the High Temperature superconductors and flux flow dynamics, which lay at the basis of the present thesis, and its application for nuclear fusion energy.

1.1 Theoretical background

1.1.1 The London Theory

The first attempt to develop the electrodynamics of superconductors belongs to the brothers F. London and H. London. The purpose of this phenomenological theory, well described in 1935, was to express in mathematical form the absence of resistance and the Meissner effect.

In a superconducting material, the superelectrons encounter no resistance to their motion. So, if a constant electric field E is maintained in the material, the electrons accelerate steadily under the action of this field:

$$m\dot{v_s} = eE \ , \tag{1.1}$$

where ν_s is the velocity of the superelectrons and m and e are their mass and charge, respectively. If there are n_s superelectrons per unit volume moving with velocity ν_s, there is a supercurrent density $J_s = n_s e v_s$. Substituting this into Eq. (1.1), an electric field produces a continuously increasing current with a rate of increase given by

$$\dot{J}_s = \frac{n_s e^2}{m} E \,, \tag{1.2}$$

Thus, the first London equation has a form of

$$\boldsymbol{E} = \frac{\partial}{\partial t}(\Lambda J_s), \tag{1.3}$$

where $\Lambda = \frac{m}{n_s e^2} = \mu_0 \lambda^2$, (1.4)

is the London parameter, and the last equality defines λ.

The second London's equation shows the relation between the magnetic field and the superconducting current. Inside a superconductor, the Maxwell's equations have the form of

$$\dot{\vec{B}} = -\vec{\nabla} \times \vec{E}, \tag{1.5}$$

$$\vec{\nabla} \times \vec{B} = \mu_0 \vec{J_s} \tag{1.6}$$

Substituting Eq. (1.2) into Eq. (1.5) gives

$$\dot{\vec{B}} = -\left(\frac{n_s e^2}{m}\right)^{-1} \vec{\nabla} \times \dot{\vec{J_s}} \,, \tag{1.7}$$

$\dot{J}_s$ can be eliminated by means of Eq. (1.6):

$$\dot{\vec{B}} = -\frac{m}{\mu_0 n_s e^2} \vec{\nabla} \times \vec{\nabla} \times \dot{\vec{B}} \tag{1.8}$$

Now

$$curl\ curl\ \boldsymbol{B} = grad\ div\ \boldsymbol{B} - \nabla^2 \boldsymbol{B},$$

But from Maxwell's equations div $\boldsymbol{B} = 0$ and then $\vec{\nabla} \cdot \dot{\vec{B}} = 0$, so Eq. (1.8) becomes

$$\dot{\vec{B}} = \frac{m}{\mu_0 n_s e^2} \nabla^2 \dot{\vec{B}}$$

or

$$\nabla^2 \dot{\vec{B}} = \frac{\mu_0 n_s e^2}{m} \dot{\vec{B}} = \frac{\dot{\vec{B}}}{\lambda^2}, \tag{1.9}$$

This implies that a magnetic field is exponentially screened from the interior of a superconductor, i.e., the Meissner effect. In other words, changes in flux density do not penetrate far below the surface, so at a sufficient distance inside the metal the flux density has a constant value, which does not change with time, irrespective of what is happening to the applied field.

Equation (1.7) is the second London's equation and λ in Eq. (1.4) and Eq. (1.9) is the London penetration depth - the characteristic length on which the magnetic field penetrates in superconductor and which is given by:

$$\lambda = \sqrt{\frac{\Lambda}{\mu_0}} = \sqrt{\frac{m}{\mu_0 n_s e^2}} \tag{1.10}$$

1.1.2 The BCS Theory

The theory developed by Bardeen, Cooper and Schrieffer (BCS) in 1957 [5] was the first capable of giving a microscopic explanation of how superconductivity emerged in traditional superconductors. The basic idea of BCS theory is that electrons bound in pairs, so-called Cooper pairs [6], and that an energy gap (Δ) appeared in the energy spectrum of the superconductor. In traditional superconductors the attractive interaction was found within the electron - phonon coupling through the local polarization of the crystal lattice in the vicinity of an electron. This makes the local positive charge capable to attract the second electron.

The Cooper problem [6] sets the pairing energy as 2Δ, where Δ is the lowest single-particle excitation energy. BCS theory introduces the size of the pair as $\xi \sim \hbar v_F \,/\, \Delta$ (the coherence length). In case of T = 0 K, all electrons in the superconductor are coupled in pairs and the energy 2Δ is needed to destroy a Cooper pair. At T ≠ 0, the thermal de-pairing arises and the quasiparticles state occupation is described by the Fermi function:

$$f(E_k) = \left(e^{\beta E_k} + 1\right)^{-1}, \tag{1.11}$$

where $\beta = 1 / k_B T$, $E_k = \sqrt{\xi_k^2 + |\Delta_k|^2}$ is the energy of the excitations, and ξ_k^2 is the kinetic energy of the electron with wave vector k .

In the BCS theory, the coherent effects in superconductor are connected to the density of the states of quasiparticles in the superconducting state. The density of states of the quasiparticles, $N(E)$, has the form of [4]:

$$N(E) = N_F \begin{cases} \frac{E}{\sqrt{E^2 - \Delta^2}} & (E > \Delta) \\ 0 & (E < \Delta) \end{cases}, \tag{1.12}$$

where N_F is the density of states near the Fermi level in the normal conductor.

The temperature dependence of the energy gap can be determined from the gap relation for Δ_k:

$$\Delta_k = -\frac{1}{2} \sum_{k'} V_{kk'} \frac{\tanh \frac{E_{k'}}{2k_B T}}{E_{k'}} \Delta_{k'} , \tag{1.13}$$

where $V_{kk'}$ is the matrix element of the interaction potential of the Cooper pairs with momenta $\hbar k$ and $\hbar k'$, which is considered as isotropic and constant near the Fermi surface and absent outside it.

For the isotropic case of s-wave superconductors, the temperature dependence of the energy gap can be obtained in implicit form as [4]:

$$\frac{1}{N(0)V} = \int_0^{\hbar\omega_c} \frac{\tanh\left(\frac{\sqrt{\xi_k^2 + \Delta^2}}{2k_B T}\right)}{\sqrt{\xi_k^2 + \Delta^2}} d\xi , \tag{1.14}$$

where V is the interaction potential, which is considered as isotropic and constant near the Fermi surface and absent outside it.

This relation determines the energy gap at zero temperature as:

$\Delta(0) = 2\hbar\omega_D \exp(-1/N(0)V)$ and the well known universal relation as: $\Delta(0) \approx 1.764 k_B T_c$. The temperature dependence of the energy gap can be determined from Eq. 1.14 [4].

1.1.3 The Ginzburg-Landau Theory

The theory proposed by Ginzburg and Landau in 1950 is the extension of the London phenomenological theory for the case of spatially varying superfluid density. It is based on the Landau theory for second order phase transitions. They pointed out that the London phenomenological theory is unsatisfactory from the two points of view. Firstly, it does not allow one to determine the surface tension at the boundary between the normal and the superconducting states. The surface energy connected with the field and supercurrent, as predicted from the solution of the London equation, is negative, contrary to the observed positive surface energy. Secondly, the theory does not enable the destruction of superconductivity by a current to be considered.

The Ginzburg-Landau (GL) theory describes the normal-superconducting transition by expressing the Gibbs free energy density g as a function of an effective wave-function of the superconducting electrons ψ, so-called a complex order parameter. The density of superconducting electrons (as defined in the London equations) was given by:

$$n_s = |\psi(x)|^2 \tag{1.15}$$

Then they assumed an expansion of the free energy in powers of ψ and $\nabla\psi$. Minimization of the free energy with respect to the order parameter leads then to a differential equation for ψ, which is analogous to a Schrodinger equation for a free particle but with a nonlinear term:

$$\frac{1}{2m^*}\left(\frac{\hbar}{i}\nabla - \frac{e^*}{c}A\right)^2\psi + \beta|\psi|^2\psi = -\alpha(T)\psi\ , \tag{1.16}$$

where $\alpha = -\mu_0 H_c^2 / |\psi_\infty|^2$ and $\beta = \mu_0 H_c^2 / |\psi_\infty|^4$ are coefficients with a smooth and regular temperature dependence and ψ_∞ is asymptotic order parameter, at $\vec{\hat{x}} \rightarrow \infty$.

The corresponding equation for the supercurrent turns out to be:

$$J_s = \frac{e^*\hbar}{i2m^*}(\psi^*\nabla\psi - \psi\nabla\psi^*) - \frac{e^{*2}}{m^*c}|\psi|^2 A \tag{1.17}$$

The major early results of the theory were in handling two features beyond the scope of the London theory, namely the spatial variation of n_s and the nonlinear effects in fields or currents strong enough to change n_s [4,7]. The theory defined the so-called intermediate state of superconductors, in which superconducting and normal domains coexist in the presence of $H \approx H_c$.

The equation for the GL penetration depth, with the same order of the London penetration depth, is:

$$\lambda_{GL} = \sqrt{\frac{m}{\mu_0 e^2 |\psi_\infty|^2}} \tag{1.18}$$

The GL theory also introduced another characteristic length – the GL coherence length:

$$\xi(T) = \frac{\hbar}{|2m^*\alpha(T)|^{1/2}} \tag{1.19}$$

The GL coherence length denotes the length over which the order parameter can vary significantly.

The ratio of the two characteristic lengths defines the GL parameter, which is independent from temperature:

$$k = \frac{\lambda}{\xi} \tag{1.20}$$

For typical, pure, so-called type I, classic superconductors, i.e. Hg, Pb, Ti etc., $\lambda \approx 500$ Å and $\xi \approx 3.000$ Å, thus $k << 1$. In this case, one can show that there is a positive surface energy associated with a domain wall between normal and

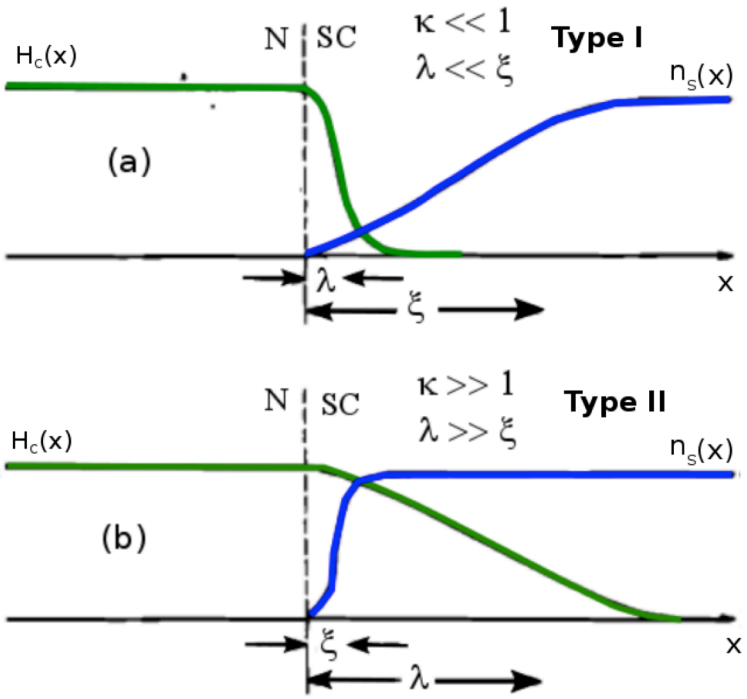

Fig. 1.5. Interface between normal and superconducting domains for (a) type I and (b) type II superconductors.

superconducting material [4]. A negative surface energy is associated with k >> 1. According to the value of the GL parameter the superconductors are divided in two classes: type I with $k < 1/\sqrt{2}$, in which a superconductor is characterized only by the Meissner state, and type II with $k > 1/\sqrt{2}$ (Fig. 1.5).

1.2 Vortex state

In 1957, A. Abrikosov published a remarkably significant paper, in which he studied the case when *k* would be large instead of small, i.e. $\xi < \lambda$ (Fig. 1.5).

Because this behaviour is so drastically different from the classic behaviour described earlier, Abrikosov distinguished it as another class, so-called type II superconductors [8]. He found that instead of discontinuous breakdown of superconductivity in a first-order transition at H_c, there was an increasing penetration of the flux starting at lower critical field H_{c1} and continuous to H_{c2}, when the superconductivity is interrupted. Thus, the phase diagram for type II superconductor consists of few regions (Fig. 1.6): below H_{c1} the Meissner state is present; an

increase of the field leads to the transition in the so-called mixed state. In this state, the magnetic field partially penetrates the volume of the superconductor. The region of the *H-T* diagram between $H_{c1}(T)$ and $H_{c2}(T)$ is known as "vortex state" or "Abrikosov state" (see section 1.2). Above the upper critical field H_{c2} the superconductor reverts to its normal state. From now on in this thesis, a term "superconductor" will refer only to type II superconductors.

In the ideal isotropic material, fluxons are round cylinders with a central normal region, or core, with the axis parallel to the externally applied magnetic field and are surrounded by circular supercurrents, which have brought fluxons to be also named "vortices". Within the core the magnetic field penetrates in form of a quantum of magnetic flux quantum [4]:

$$\Phi_0 = \frac{hc}{2e} = 2 \cdot 10^{-7}\ G \cdot cm^2\ , \tag{1.21}$$

The density of vortices within the superconductor in the mixed state is related to the magnetic field strength, by the relation $\mu_0 H = n\Phi_0$, where n is the areal density of vortices.

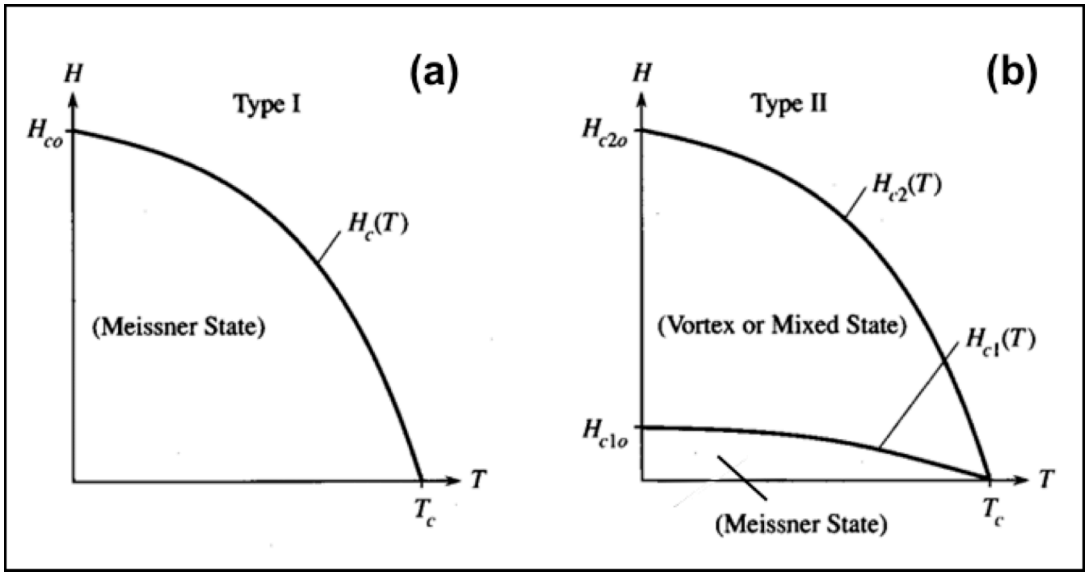

Fig. 1.6. Phase diagrams of (a) type I and (b) type II superconductors.

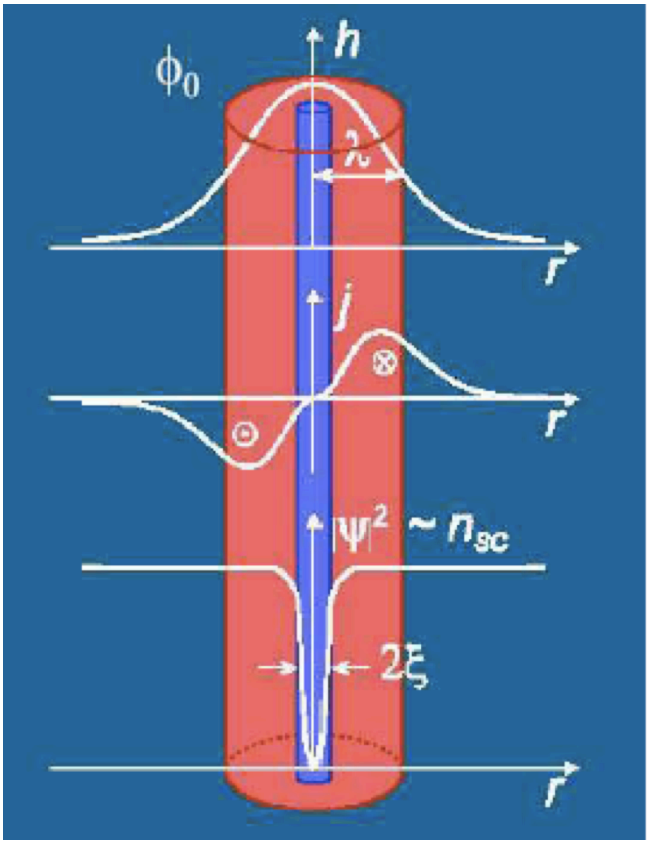

Fig. 1.7. A sketch of a fluxon structure

Within the GL framework, the structure of the fluxon can be represented as follows: it is made up of a normal core of the radius ξ where the magnetic field is focused by circular currents, which cancel the effect of the surface screening currents. Both, currents and field, decay exponentially away from the core over a distance of λ (Fig. 1.7).

The energy per unit area, ϵ_b, of the boundary between the normal and the superconducting regions is usually expressed in terms of a characteristic length δ_b:

$$\epsilon_b = \frac{1}{2\mu_0} H_c^2 \delta_b, \tag{1.22}$$

If the boundary is stable, the superconducting and normal regions must be in equilibrium, thus the free energy per unit volume must be the same. Due to the

presence of ordered electrons, the free energy density of the superconductive state is lowered by an amount $f_n - f_s = \frac{1}{2\mu_0} H_c^2$, and, in addition, because the superconducting region has acquired a magnetization which cancels the flux density inside, there is a positive magnetic contribution $\frac{1}{2\mu_0} H_c^2$. At equilibrium, the free energy density of a neighboring normal region is the same because these two contributions cancel each other. At the boundary, however, the superconductivity increases only gradually over a distance determined by ξ, and the magnetic contribution decreases over a distance λ. Roughly speaking, one can consider the change in flux density and superelectron density within the superconductor as occurring sharply at distances λ and ξ, respectively, from the edge of the normal region. In this way the value of the surface energy is:

$$\epsilon_b \simeq \frac{1}{2\mu_0} H_c^2 (\xi - \lambda), \tag{1.23}$$

and the characteristic length δ_b can be identified as $(\xi - \lambda)$. If $\xi < \lambda$, like in type-II superconductors, the surface energy is negative and nucleation of normal regions becomes favorable when the magnetic field overcomes the lower critical field H_{c1}. The surface energy allows the determination of the lower critical field value:

$$H_{c1} = \frac{\Phi_0}{4\pi\lambda^2} \ln k \,, \tag{1.24}$$

It can be also shown that the upper critical field H_{c2} is related to the microscopic parameters by:

$$H_{c2} = \frac{\Phi_0}{2\pi\xi^2} \,, \tag{1.25}$$

For anisotropic superconductors, such as High Temperature Superconductors (HTS, see section 1.3), the situation is more complex. Both, the coherence length ξ, and the penetration depth λ, exhibit an anisotropic character with $\xi_c < \xi_{ab}$ and $\lambda_c > \lambda_{ab}$, so that both H_c and $k = \frac{\lambda_{ab}}{\xi_c} = \frac{\lambda_c}{\xi_{ab}}$ remain unaffected, where the suffix refers to the crystallographic *ab*-axes and the *c*-axis. As consequence, while in an

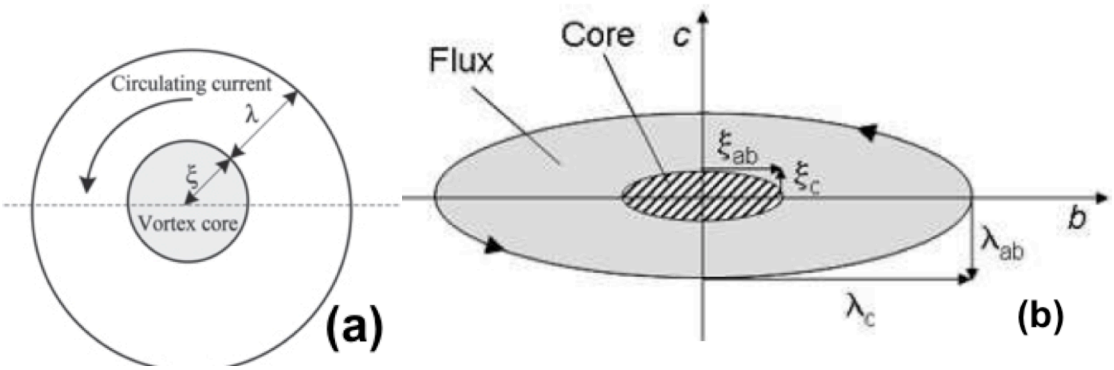

Fig. 1.8. Schematic representation of a vortex cross section: (a) in isotropic superconductor (b) in an anisotropic superconductor.

isotropic superconductor the vortices have a circular symmetry as was described earlier, in an anisotropic superconductor the shape of fluxons depends on the orientation of the magnetic field with respect to the crystallographic axes. When the magnetic field penetrates normal to the c-axis, the core radius along the plane direction will be ξ_{ab}, while the core radius along the *c*-axis will be $\xi_c << \xi_{ab}$. On the other hand, the flux penetration radius will be λ_c along the plane whereas it will be the smaller value λ_{ab} in the *c*-axis direction (Fig. 1.8) [4].

The application of field $H > H_{c1}$ determines the creation of many vortices that arrange on regular patterns. Abrikosov identified the possible regular patterns as a triangular lattice having a hexagonal basic unit cell, so-called Abrikosov lattice (Fig. 1.9), where the distance between two vortices is given by $a = 1.072\sqrt{\Phi_0 / B}$. The vortex distance decreases with increasing the magnetic field.

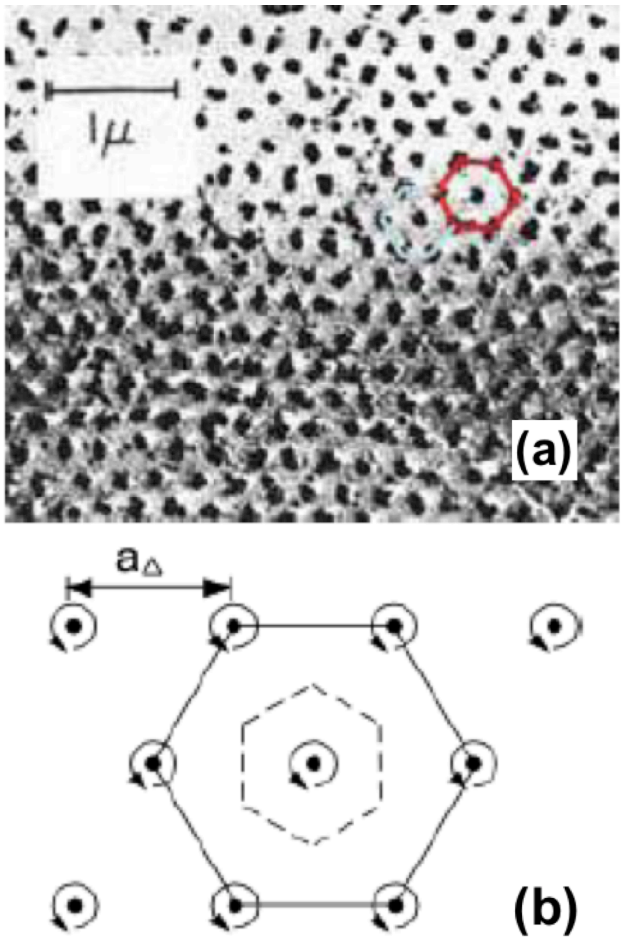

Fig. 1.9. (a) Triangular (Abrikosov) lattice of flux lines in clean Nb sample evidenced by magnetic decoration technique; (b) a sketch of hexagonal unit cell in fluxon lattice, viewed along a section normal to vortices lattices. Vortex supercurrents are indicated by circular arrows.

In the mixed state of HTS interplay of vortex-vortex interactions, thermal fluctuations, different kind of disorder and the anisotropic behaviour create different phases, referred as vortex matter [9]. However, the main characteristic of a HTS phase diagram is the existence of two states: a magnetically irreversible zero-resistance state, called vortex solid phase, and a reversible state with dissipative transport properties, called vortex liquid state [10] (Fig. 1.10). In the absence of disorder, as in the systems free of defects, the solid phase presents topological order (forming the Abrikosov lattice) and it is separated from the liquid phase by a first order transition (melting line) [9]. In the presence of disorder (defects), the second order transition, irreversibility line, is found between the solid and the liquid phases [11,12]. YBCO material (see section 1.4.1) has a variety of disordered vortex solid

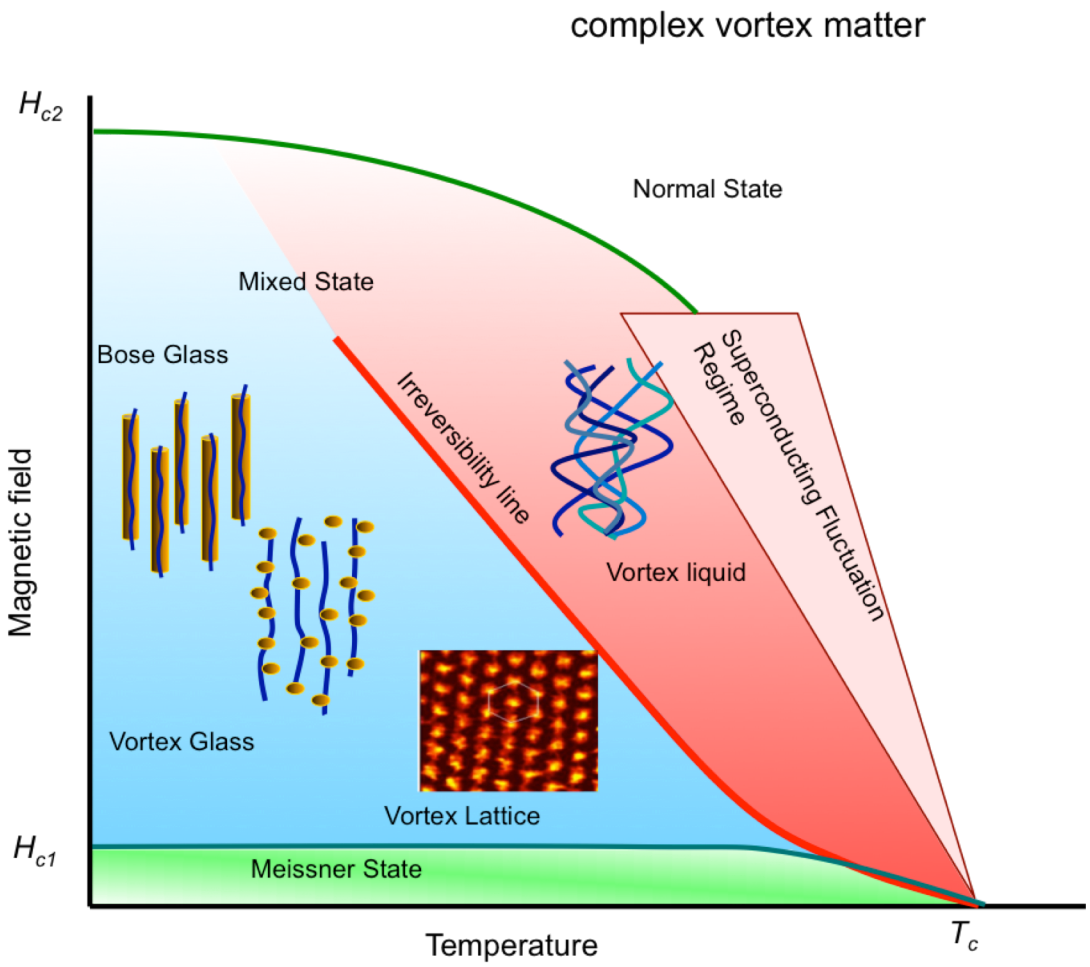

Fig. 1.10. A schematic illustration of the different phases of vortex matter on a phase diagram.

states, depending on the type and dimensionality of the defects. In the presence of isotropic weak random point disorder, like oxygen vacancies or electron irradiation (see Section 1.5), a vortex glass phase has been predicted [11]. In the presence of correlated disorder, such as dimensional elongated columnar defects or planar defects (twin boundaries), Bose glass phase is expected [13,14] (Fig. 1.10).

It can also be shown, that most of the macroscopic superconductive properties have an anisotropic character. For example, both the upper and the lower critical fields depend on the direction of the magnetic field as $\propto 1/\xi^2$ and $\propto 1/\lambda^2$, respectively. When the field is perpendicular to the *c*-axis, i.e. when the angle θ between the field direction and the *c*-axis is $\theta = 90°$, H_{c2} is increased and H_{c1} is decreased with respect to the $\theta = 0°$ configuration (Fig. 1.11).

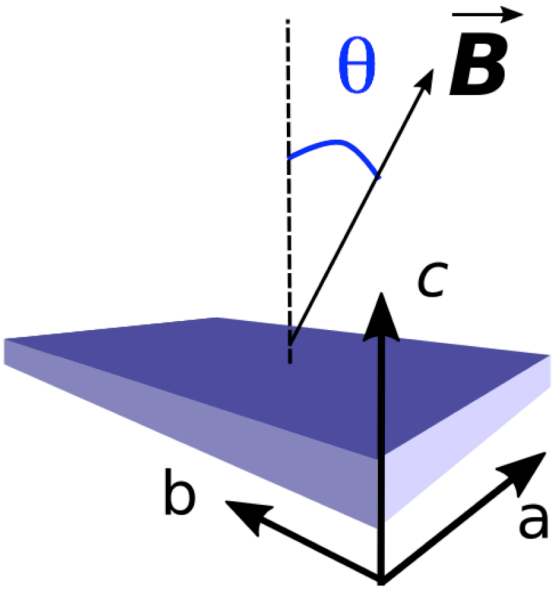

Fig. 1.11. Reference coordinate system used in the description of the parameters in anisotropic superconductors.

Thus, the anisotropy increases the width of the Meissner state at $\theta = 90°$ allowing the nucleation of flux lines along the *ab*-planes at almost vanishing values of the field. The anisotropy degree of the superconductor can be quantified using the anisotropy parameter γ:

$$\gamma = \frac{\lambda_c}{\lambda_{ab}} = \frac{\xi_{ab}}{\xi_c} = \left(\frac{H_{c2\|ab}}{H_{c2\|c}}\right) = \left(\frac{H_{c1\|c}}{H_{c1\|ab}}\right), \tag{1.26}$$

The anisotropy of H_{c2} can be interpreted in a more general scaling approach, derived from the GL equations and proposed by Blatter et. al. [15]. According to this model, any physical quantity Q for which the isotropic result $\tilde{Q}$ is known, can be determined through the scaling rule:

$$Q(\theta, H, T, \xi, \lambda, \gamma) = s_Q \tilde{Q}(\epsilon(\theta)H, \gamma, T, \xi, \lambda)\,, \tag{1.27}$$

where θ is the angle between the applied magnetic field and the *c*-axis, γ is the anisotropy parameter, ξ and λ refer to the value on the *ab*-plane, s_Q is a scaling factor, and $\epsilon(\theta)$ is given by:

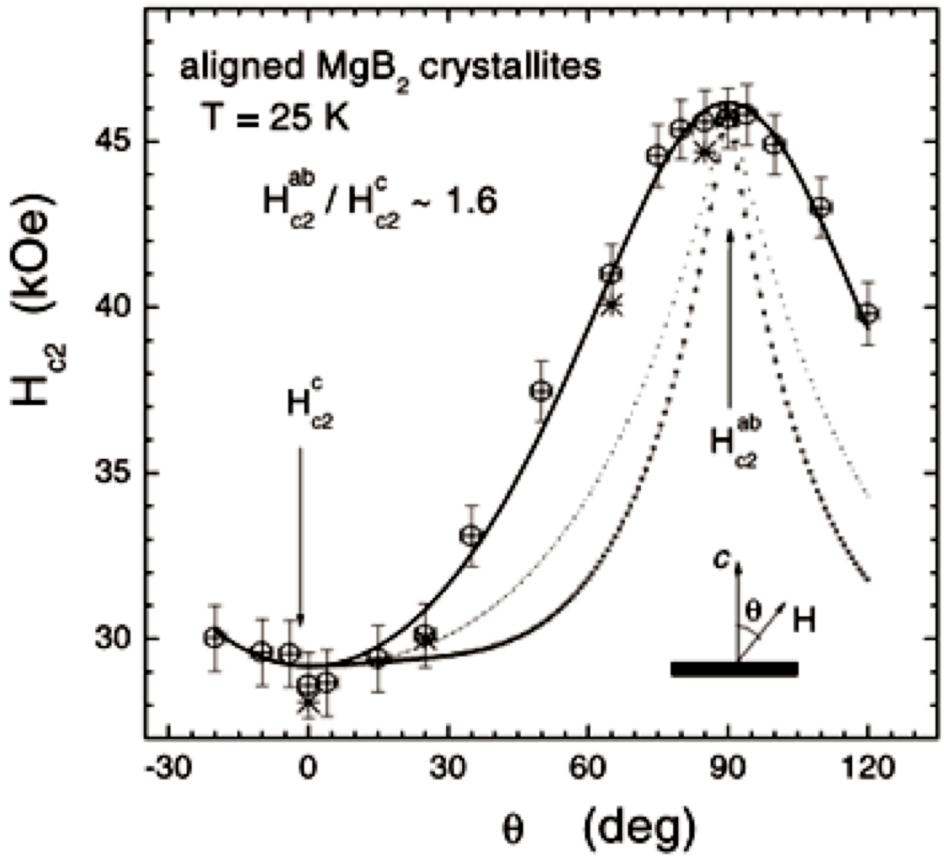

Fig. 1.12. An example of upper critical magnetic field as a fuction of the angle θ, in anisotropic MgB_2 superconductor.

$$\epsilon(\theta) = \sqrt{cos^2\theta + \frac{1}{\gamma^2}\, sin^2\theta}, \tag{1.28}$$

In this way, the angular dependence, interpolating H_{c2} between the limiting values 0° (H // c) and 90° (H // *ab*), can be worked out from Eq. (1.27) giving the simple ellipsoidal form (Fig. 1.12):

$$H_{c2}(\theta) = \frac{\tilde{H}_{c2}}{\epsilon(\theta)} = \frac{H_{c2}^{\parallel c}}{\sqrt{cos^2\theta + \frac{1}{\gamma^2} sin^2\theta}}, \tag{1.29}$$

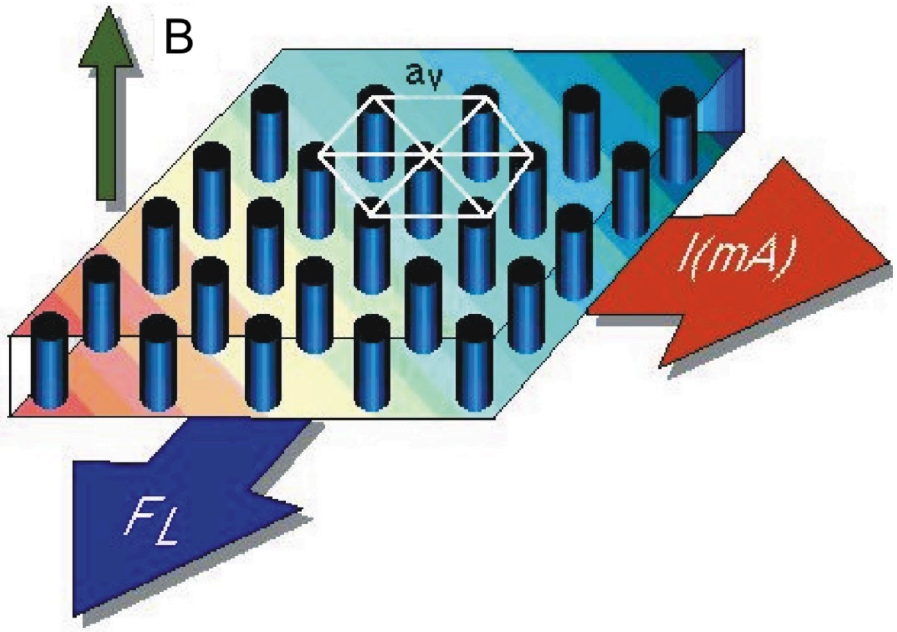

Fig. 1.13. Lorentz force F_L exerted on a vortices and created by applied magnetic field and transport current J.

1.3 Vortex dynamics

1.3.1 Vortex motion

When a transport current is passed along the superconductor in the presence of an applied magnetic field, which drives the superconductor into the vortex state, the current flows through its whole volume. Considering a length of the superconductor, at every point there will be a certain transport current density, *J*. Thus, there will be an electromagnetic force, Lorentz force F_L, between the flux and the current, (Fig. 1.13), which drives the vortex movement in a direction perpendicular to the direction of the applied current [4]:

$$\vec{f}_L = \vec{J} \times \hat{n}\Phi_0 = \vec{J} \times \vec{B}\,, \tag{1.30}$$

where Φ_0 is the flux quantum; $\hat{n}$ is the unit vector yielding the magnetic field direction; $\vec{J}$ is the current density and $\vec{B}$ is the magnetic field induction (within the London limit $B = \mu_0 H$).

Vortex motion has a strong impact on conducting properties of the superconductors in the mixed state, since the vortex movement generates the electric field $\vec{E} = \overrightarrow{v_L} \times \vec{B}$, where B is a magnetic induction and v_L is the flux lattice velocity.

In presence of the DC current, a vortex starts to move only at $J > J_c$, where J_c is the so-called depinning critical current density, yielding $F_L > F_p^{max}$. The balance of the fields acting on the vortex can be obtained in the following form:

$$\vec{F} + \overrightarrow{F_H} + \overrightarrow{F_p} = \overrightarrow{F_L} + \overrightarrow{F_t}\,, \tag{1.30}$$

where F_t represents the force of the thermally activated vortex movement; $\overrightarrow{F_H} = \alpha_H \hat{n} \times \overrightarrow{v_L}$ is the perpendicular force on a moving vortex (Hall force), which subtends the Hall angle $\Theta = arctan\,(\alpha_H/\eta)$. Usually $\alpha_H << \eta$ and the Hall angle is small, thus it can be neglected [9].

The drag force compensates the Lorentz force. The electric field generated by vortex motion can be divided in the two components: longitudinal to the current, which produces the dissipation, and transversal, which determines the Hall effect. Two mechanisms of the dissipation due to vortex motion can be considered. The first is related to the condensation energy during movement: the Cooper pairs on the vortex front side are transformed to quasi-particles with energy loss; the inverse transformation occurs on the rear side, but due to the finite relaxation time only part of the energy is recovered [8]. In the free flux-flow regime, the flux flow resistivity can be rewritten in the form, given by Bardeen and Stephen [16]:

$$\rho_{ff} = \frac{\mu_0 H_{c2} \Phi_0}{\eta}, \tag{1.31}$$

The second mechanism is due to the Joule dissipation by the normal currents moving through the vortex core [16]. The power dissipated per unit length is related to η through $W = F v_L = \eta v_L^2$. In [9,17] the vortex viscosity is determined in the general case:

$$\eta = \pi hn \frac{\omega_0 \tau}{1+(\omega_0 \tau)^2} \quad (1.32)$$

where $\omega_0 = e\mu_0 H_{c2}/m$ is the cyclotron frequency given by the level separation of the quasi-particle states within the vortex core [18]. Two regimes can be identified: superclean $\omega_0 \tau \gg 1$ and moderately clean, when $\omega_0 \tau \ll 1$. In the latter limit, in absence of the Hall effect the Bardeen and Stephen (BS) relation [16] can be obtained as:

$$\eta = \pi hn \omega_c \tau = \frac{\mu_0 H_{c2} \Phi_0}{\rho_n}, \quad (1.33)$$

where $\rho_n = m^*/ne\tau$ is the normal state conductivity.

At $\omega_0 \tau \gg 1$ the Hall contribution dominates and the viscosity can be determined as [17]:

$$\eta \approx \frac{\pi hn}{\omega_c \tau} \quad (1.34)$$

This corresponds to the superclean limit [19]. In this limit, there are well-separated bound states in the vortex core.

1.3.2 Vortex pinning

In a real superconductor, defects in the crystal structure are always present. They represent the preferable sites for vortices, so-called pinning centres, since they allow minimizing the total condensation energy cost. Core pinning arises whenever a local depression of ψ (caused by impurities, lattice defects – point-like or extended - or thickness non uniformities along a fluxon) entails a loss of condensation energy, which can be partially restored if a fluxon pins to it. Considering the whole fluxon system, it is important to recognize that if it were perfectly periodic and rigid the average effects of random pinning centers would be vanishingly small. Pinning forces therefore arise from both, the fluxon elasticity and from the interaction between fluxons and pinning sites [6, 64]. The pinning effectiveness is influenced by the vortex phases, direction and intensity of *H*, kind and distribution of pinning sites and also flux line tension: rigid flux line can be pinned by a single pinning center, but weakly correlated ("pancake") vortices (Fig. 1.14) require to be individually pinned

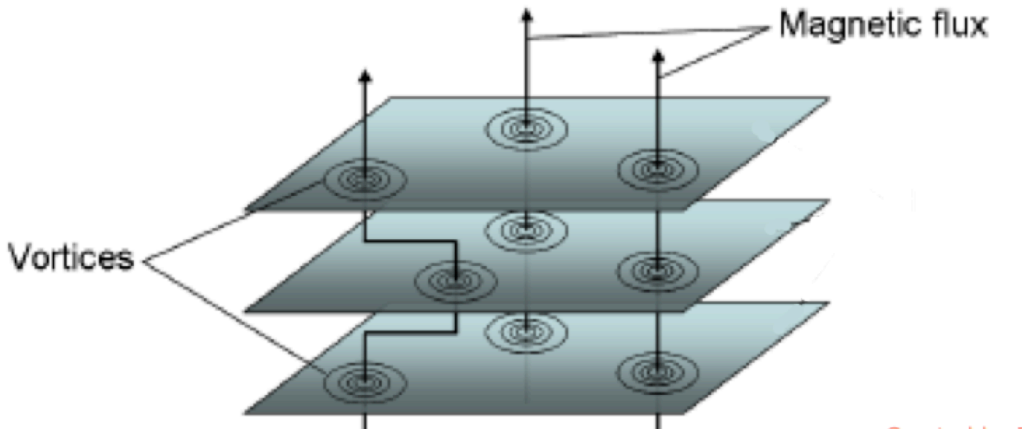

Fig. 1.14. Schematic representation of a pancake vortices stack forming straight and distorted flux lines.

on each distinct layer in the layered superconductors, e.g. YBCO (see Section 1.4). Clusters of entangled flux lines, on the other hand, would present lower mobility with respect to independent flux lines or pancakes.

The overall pinning effect can be described in terms of a local pinning potential *U (r,H)*. Fluxons prefer to occupy the pinning potential minima (potential well) (Fig. 1.15 (a)): any small displacement from these equilibrium positions gives rise to a restoring force on the fluxon. The *H*-dependence of the pinning potential *U* can be appreciated by resorting to the distinction between individual and collective pinning, following [17]. The individual pinning is present at very low fields, giving low fluxon concentrations: in this case there are more pinning sites than fluxons so the latter do not interact with each other and the pinning potential do not depend on the fluxon concentration, i.e. on the field. The collective pinning, related to higher fields, arises when many close-packed fluxons collectively interact with the same pinning site: in this case the intensity of the interaction depends on their number, which is field dependent. The rate of the vortex jump (The Anderson and Kim model for *flux creep* [20]) is determined as $\overline{\omega} = \omega_t e^{-U_0/k_B T}$, where ω_t is the characteristic frequency in the range 10^5 - 10^{11} s^{-1}. DC external current produces the tilt of the pinning potential as shown in Fig. 1.15. Along the Lorentz force direction the energy well height is lowered by the Lorentz force energy with respect to the unperturbed

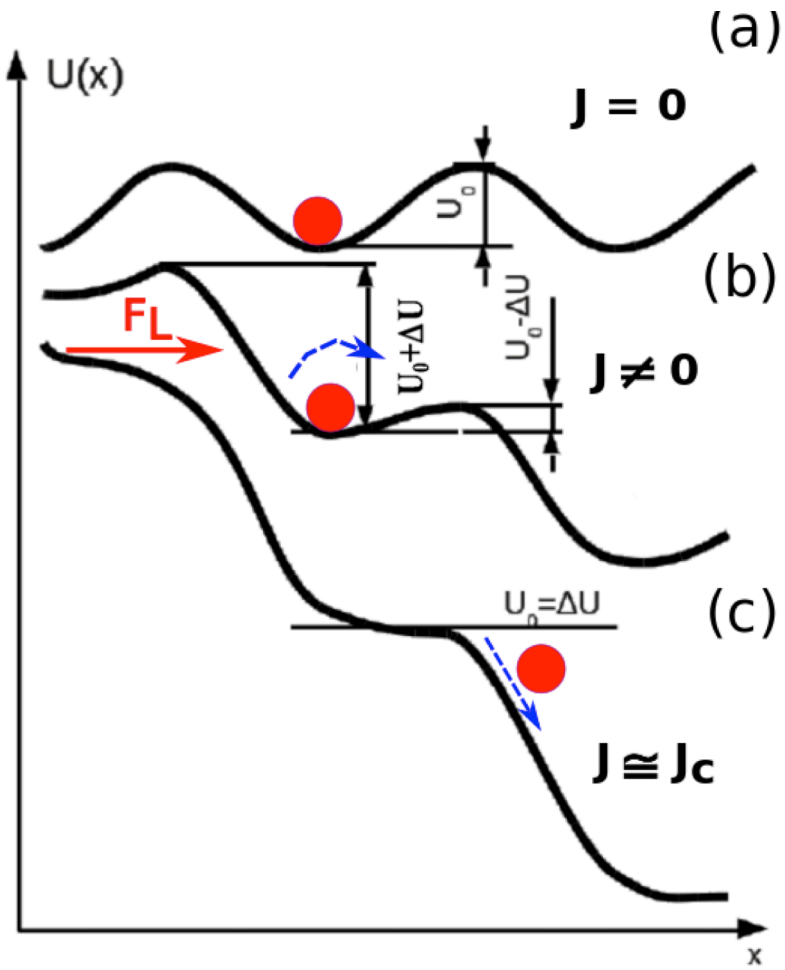

Fig. 1.15. (a) fluxon in a minimum of the pinning potential U in absence of external current; (b): pinning potential U tilting due to external DC current density J; (c) pinning potential U unidirectional leveled by J ~ J_c: free flux flow.

pinning potential and equals to $U_0 - U$, and thus, flux movement or jumping is favoured.

The energy barrier can be written as $U_0 = 0.5\mu_0 H_c^2 l^3$, where H_c is the thermodynamic critical field and l is the linear dimension of the point-like defects [20].

The presence of pinning is the cause of the additional force (the pinning force F_p) that reduces the mobility of the vortex. The pinning of a fluxon core of radius ξ is more effective when the linear dimension l of the point-like defects $l \simeq \xi$ (strong pinning). In this case the pinning force can be determined as $F_p \sim \mu_0 H_c^2 \xi^3$. The

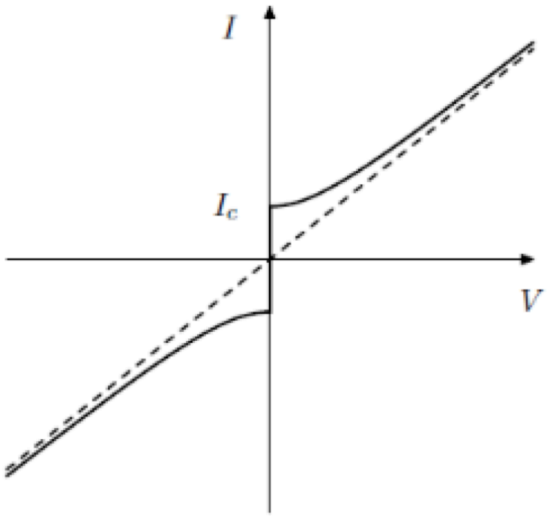

Fig. 1.16. Schematic representation of an ohmic *I* - *V* curve.

condition $l < \xi$ gives lower pinning force due to smaller energy gain of smaller defects; the condition $l > \xi$ gives the residual movement freedom to a fluxon and the pinning force is determined as: $F_p \sim 1/l$.

The critical current density J_c is that current per unit volume of a superconductor at which a detectable voltage is produced across the superconductor, and is therefore that current, which causes the vortices to move. If the current density is such that the Lorentz force is less than the pinning force, no movement of vortices will occur, and no voltage will be detected in the superconductor. If the current is increased to a value at which the Lorentz force exceeds the pinning force, vortices will move and a voltage will be detected. The critical current density is that value of the current density at which the vortices will begin to move, thus giving $J_c = F_p / B$: when current density J approaches its critical value, J_c, the potential is tilted enough for fluxons to freely flow in the current direction, reaching the flux flow regime (Fig. 1.15 (c)). The dissipation takes the form of an ohmic *I* - *V* curve (Fig. 1.16).

Typically, the critical current density as a function of applied magnetic field for a high-temperature superconductor shows three regimes: an initial region in which the critical current decreases rapidly as soon as the field is turned on; a region, which can

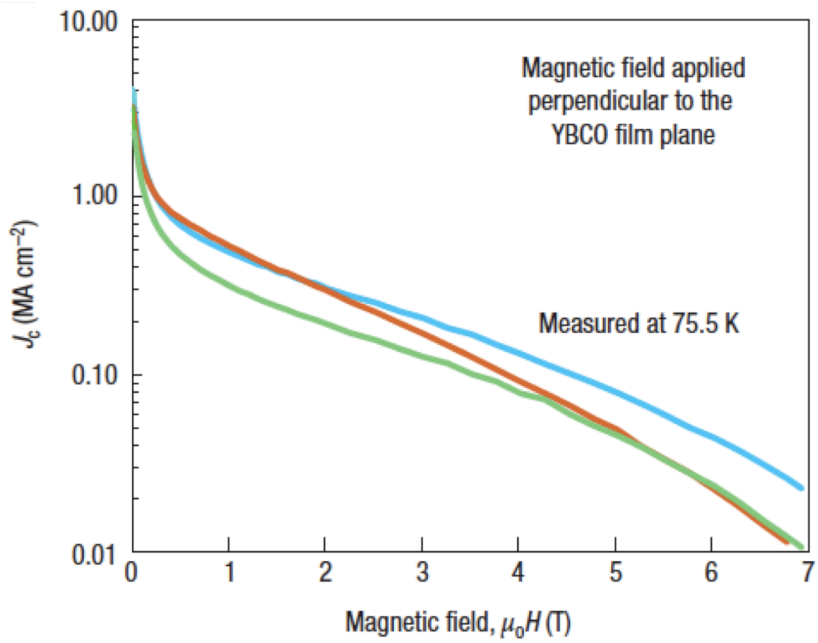

Fig. 1.17. A typical critical current dependence on the magnetic field shown for different samples of YBCO superconductors.

be linear, falling slowly with increasing field, and a third region in which the critical current falls to zero [21] (Fig. 1.17).

As mentioned earlier, the macroscopic superconductive properties have an anisotropic character. The pinning strength is a function of the direction of an external magnetic field relative to the *ab*-planes of the superconductor. The critical current density is much higher with the field parallel to the *ab*-planes than when it is perpendicular to them (i.e., H // *c*-axis of the planes). In typical angular dependence plots like presented on Figure 1.18, YBCO superconductor almost always has a strong peak at 90° (the applied field is parallel to the YBCO *ab*-planes). In addition to this intrinsic peak, superconductor might have a second peak at 0° (parallel to the YBCO *c*-axis), which is correlated with linear defects related to columnar growth.

This type of measurement of J_c is essential for elucidating the types of important flux-pinning defects present in films and must ultimately become a routine part of enhancement research.

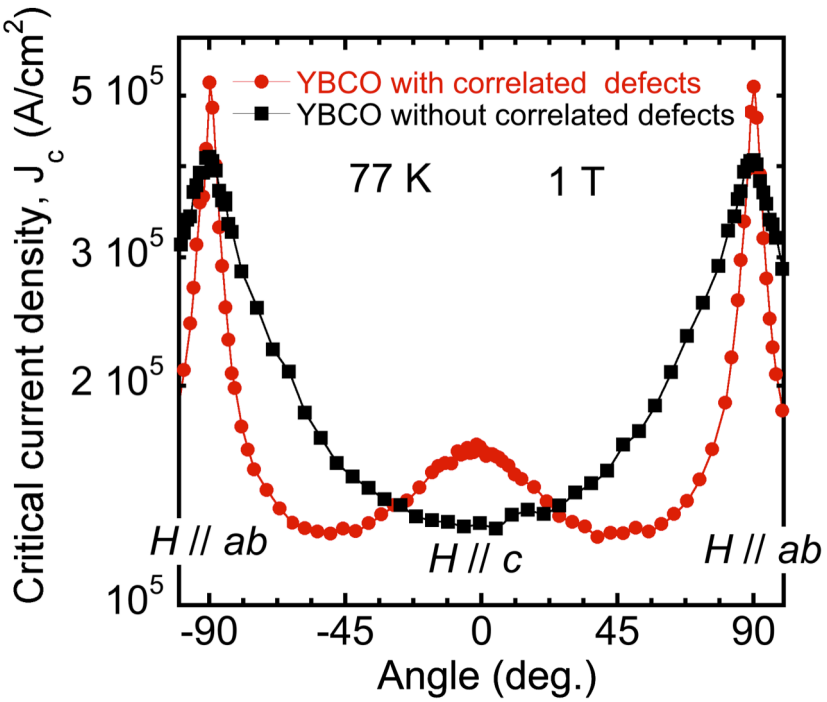

Fig. 1.18. A typical angular critical current density dependence of YBCO superconductor with only intrinsic pinning corresponding to the peak at 90° (full black squares) and with additional correlated pinning at 0° (full red circles).

1.3.3 AC electrodynamics in the mixed state

The pinning force contribution is related to the spatial variation of the pinning potential as $\overrightarrow{F_p} = -\nabla U$. When a small displacement of the vortices occurs, the vortex does not interact with nearby ones (single vortex approximation). Considering the harmonic regime $J \propto e^{i\omega t}$ and sufficiently high angular frequency ω, the vortex oscillates around the equilibrium position with small amplitude. In the limit of small displacement $u = v_L/(i\omega)$, the pinning force is elastic and can be written as:

$$\overrightarrow{F_p} = -\nabla U \simeq -k_p u\,, \tag{1.35}$$

where $k_p = \nabla^2 U$ is the pinning constant (also known as Labusch parameter, α_L).

Considering an electromagnetic field incident on a flat interface between a generic medium and a superconductor, the response to the field is given by the surface impedance, Z_s [22] (see Chapter 4). In case of a bulk sample (thick with respect to

the field penetration depth) in the local limit, this quantity can be written in the two equivalent forms:

$$Z_s = i\omega\mu_0\tilde{\lambda} = \sqrt{i\omega\mu_0\tilde{\rho}} \tag{1.36}$$

where $\tilde{\lambda}$ is an appropriate complex screening length and $\tilde{\rho} = i\omega\mu_0\tilde{\lambda}^2$ is the complex resistivity. The complex resistivity $\tilde{\rho}$ (or equivalently Z_s or $\tilde{\lambda}$) of a superconductor in the mixed state includes contributions from the moving vortex lattice and from the two types of charge carriers, normal and superconducting.

Many models have been developed in order to capture the overall AC vortex dynamics, having various degrees of complexity [23–25]. Basically, they take into account the relation in Eq. (1.30).

One of the models, the Gittleman and Rosemblum (GR) model [26], is valid for the superconductor at the temperatures $T << T_c$, where the effect of the thermally activated movement is negligible. Neglecting the Hall and thermal forces leads to the relation:

$$\eta\overrightarrow{v_L} + \frac{k_p\,\overrightarrow{v_L}}{i\omega} = \vec{J} \times \hat{n}\Phi_0 \tag{1.37}$$

For current $\vec{J} \perp \vec{B}$ in the scalar form one obtains:

$$\left[\eta + \frac{k_p}{i\omega}\right] v_L = JB\Phi_0 \tag{1.38}$$

The vortex motion resistivity can be obtained from Eq. (1.38) using the relations $\vec{E} = \rho_{vm}\vec{J}$ and $\vec{E} = \vec{B} \times \overrightarrow{v_L}$ (with the London limit $B = \mu_0 H$):

$$\rho_{vm} = \frac{B\Phi_0}{\eta}\frac{1}{1 - i\frac{k_p}{\eta\omega}} \tag{1.39}$$

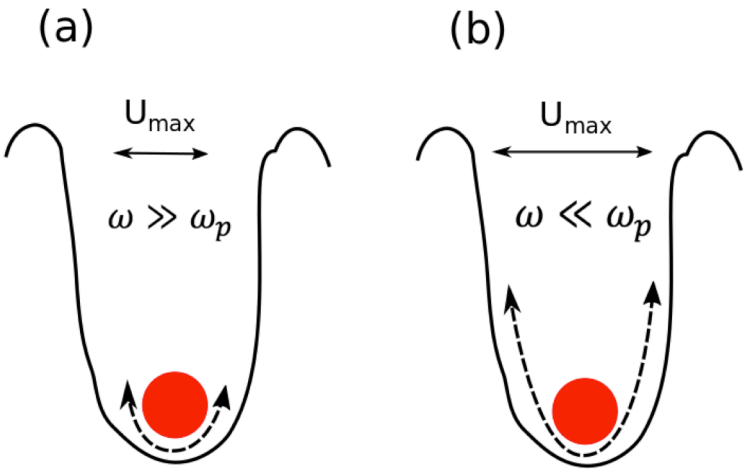

Fig. 1.19. (a) Fluxon small oscillations inside pinning potential well with high frequency; (b) Fluxon wide oscillations inside pinning potential well with low frequency.

Two important parameters are included in Eq. (1.39): the flux-flow resistivity $\rho_{ff} = \frac{B\Phi_0}{\eta}$ and the so-called depinning angular frequency $\omega_p = \frac{k_p}{\eta}$, which define the crossover between elastic and dissipative motion. At lower frequencies $\omega \ll \omega_p$, the flux-flow resistivity is imaginary. At high frequencies $\omega \gg \omega_p$, it is fully dissipative end equal to the flux-flow resistivity $\rho_{vm} = \rho_{ff} = \frac{B\Phi_0}{\eta}$, where the movement of the vortices is not affected by pinning. In this regime, it is possible to determine directly the flux-flow resistivity without the application of large current densities.

On a contrary, with respect to the DC applied current described in previous section, the AC vortex dynamics and displacement of vortices is assumed to be a linear function of the current density *J*. This assumption, justified by the small vortex displacement at microwave frequencies (Fig. 1.19), implies also a pinning potential independent from the driving current intensity, thus excluding flux creep which arises for $J \lesssim J_c$ (as was shown in Fig. 1.15 (b)).

In this work, the high-frequency regime (Fig. 1.19 (a)) for microwave measurements has been used to study the pinning parameters (see Chapter 4).

1.4 High-Temperature Superconductors (HTS)

As was mentioned in the beginning of this Chapter, a discovery of High-Temperature Superconductors (HTS) by Bednorz and Muller lead to the whole new world of superconductors with T_c well above liquid nitrogen temperature, usually around 100 K, which meant the the new area of superconductor applications, since cooling would be provided by liquid nitrogen and not liquid helium. HTS are type II superconductors, which means the presence of vortex (mixed) state in the phase diagram and most of HTS are ceramic copper oxide (cuprate) compounds.

1.4.1 $YBa_2Cu_3O_{7-x}$

One of the most technologically relevant and well studied since its discovery HTS is $YBa_2Cu_3O_{7-x}$ (YBCO), which is a subject of a study in the present thesis.

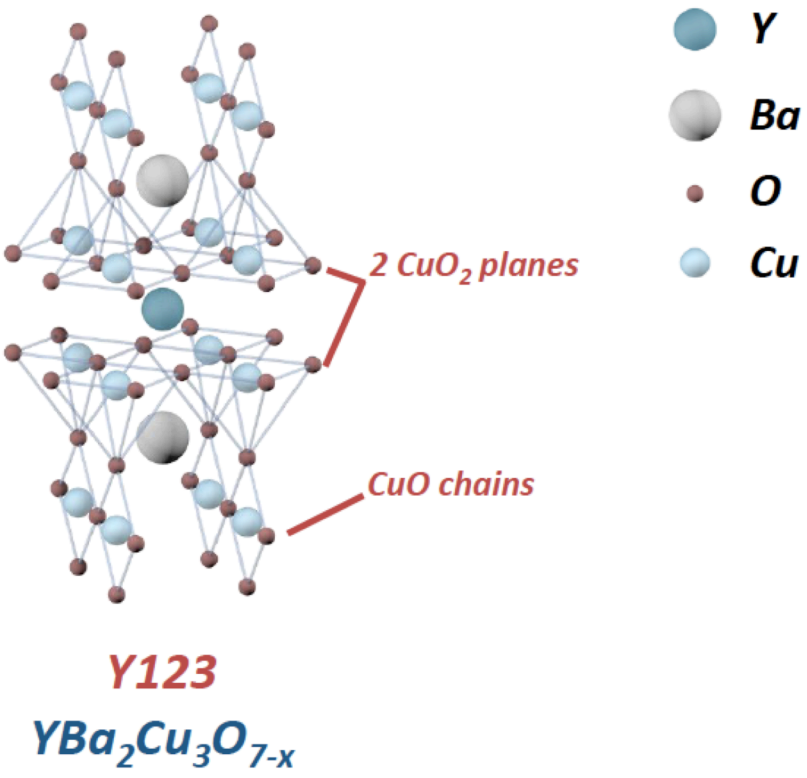

Fig. 1.20. Crystallographic structure of $YBa_2Cu_3O_{7-x}$ unit cell.

.

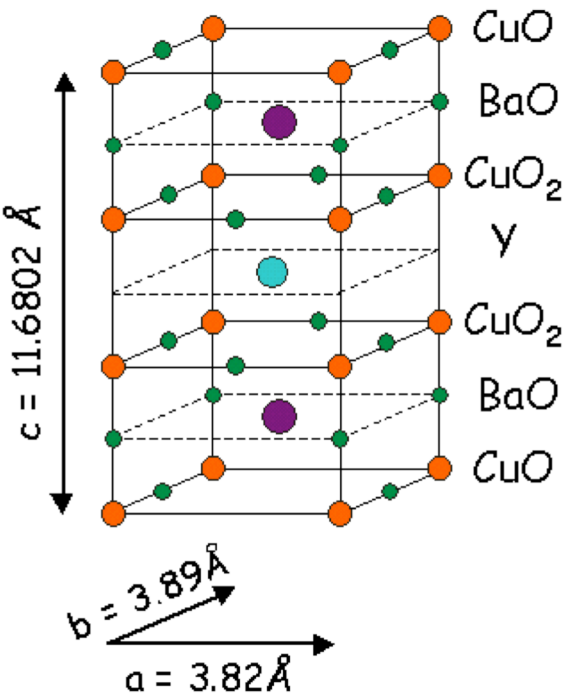

Fig. 1.21. Layered structure of YBCO with lattice parameters.

.

YBCO exhibits a complicated crystallographic structure, which is often referred to as perovskite-type. This is because the YBCO unit cell (Fig. 1.20) can be viewed as the series of perovskite cells aligned along the c-axis of the compound. The complex unit cell of YBCO can be also viewed as a series of CuO_2 planes lying normal to the c-axis and creating the so-called layered structure (Fig. 1.21), which determine the superconducting properties of this material. These CuO_2 planes are the superconducting planes containing mobile charge carriers and providing the supercurrents flow. CuO_2 planes are separated by charge-reservoir interleaved layers, which contain CuO chains. These charge reservoir layers are responsible for a proper carrier density the superconducting CuO_2 planes. In YBCO, the superconductivity is controlled by oxygen content in the structure, which modifies the final T_c of YBCO [27] (Fig. 1.22).

Due to the planar (layered) structure, YBCO exhibits anisotropic properties along *ab*-axes and *c*-axis. The critical current density parallel to the CuO_2 planes (*ab*-plane) is much higher than that flowing through *c*-axis. Therefore, it is crucial to grow YBCO layers highly epitaxial with c-axis normal to the substrate and study angular transport properties of the films.

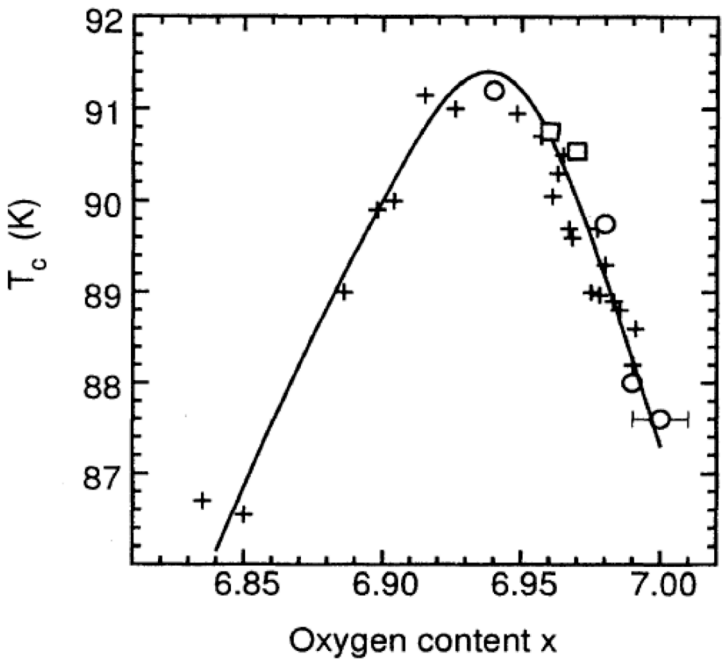

Fig. 1.22. Critical temperature dependence on the oxygen content [20].

1.4.2 Vortex pinning centres

Pinning centres (sites) in a superconductor arise from the presence of localized material defects or crystalline imperfections that reduce the vortex energy such that vortices tend to remain pinned at the bottom of these potential energy wells. Important properties are the size, shape and density of pinning sites. These defects can appear spontaneously during the growth process of a superconductor (natural defects) or could be artificially introduced (Artificial Pinning Centres, APCs) with the aim of enhancing the pinning properties and, hence, superconducting transport properties. To maximize J_c, one needs to engineer the optimum vortex-pinning landscape. It has been known since that J_c in YBCO film could be 10–100 times higher than YBCO crystals because of the large density of defects inherent in thin-film growth [28].

There are a number of defect types that can act as pinning centres, which are represented in Figure 1.23 [29]. Different criterions can be used to classify the pinning centres. One of the most common criterions is dimensionality: zero-

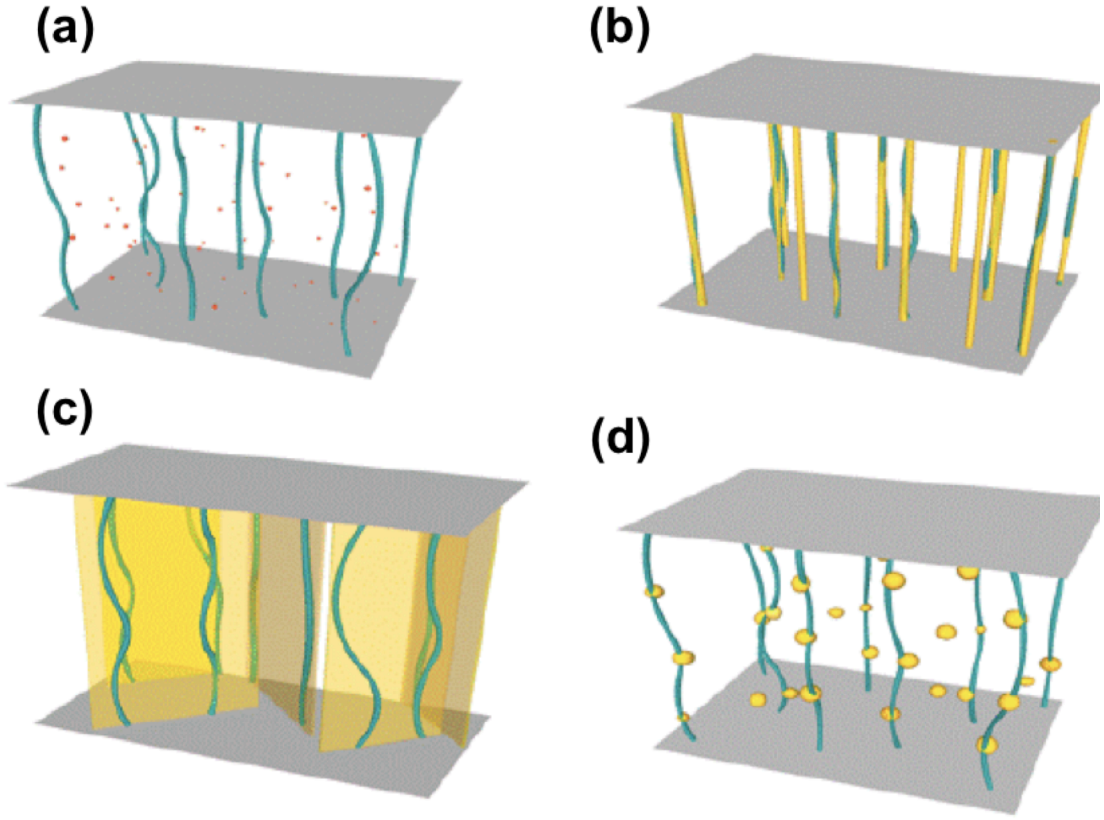

Fig. 1.23. A sketch of defects with different dimensionality, acting as pinning centres, taken from [22]: (a) 0 – D defects; (b) 1 - D defects; (c) 2 – D defects; (d) 3 – D defects. Curved lines represent the fluxons.

.

dimensional (0 - D) defects (oxygen vacancies, point defects);one-dimensional (1 - D) defects (dislocations, columnar defects) [30–34]; two-dimensional (2 - D) defects (low-angle grain boundaries, twin boundaries, stacking faults, intergrowths) [28,35–39]; and three-dimensional (3 - D) defects (nanoparticles, local strained regions) [40–42]. Usually, different type and size of defects are simultaneously present in the material.

The pinning itself can be divided into two categories: *Correlated pinning* and *random pinning*. Correlated pinning arises from approximately parallel arrays of extended linear or planar defects. Their effect is strongest when the applied magnetic field (which determines the orientation of the vortices) is aligned with them, and it decreases as the misalignment between defects and vortices increases. The signature of correlated pinning is a peak in the angular dependence of J_c. Random uncorrelated pinning is due to randomly distributed localized defects, and in this case the

influence is relatively uniform for all magnetic field orientations. Thus, the pinning sites can be also classified as isotropic or anisotropic pinning centres, depending on the orientation of the applied magnetic field and anisotropy of the defects.

1.5 Superconductors for nuclear fusion energy

Progressive research and constant development in technology lead to an increasing variety of possible applications of High-Temperature Superconductors, which have been already successfully produced by different manufacturers for the needs of electrical utility sector [43]. As such a remarkable progress in the understanding of the theoretical and practical features and mechanisms of HTS has been made, although many more of them have not yet been studied well enough to be able to control the whole preparation and fabrication processes.

The European fusion programme is based on the roadmap to the realisation of fusion energy. ITER will be the first fusion device to produce net energy and to maintain fusion for long periods of time, as well as testing the integrated technologies, materials, and physics regimes necessary for the commercial production of fusion-based electricity. It is designed to generate 500 MW fusion

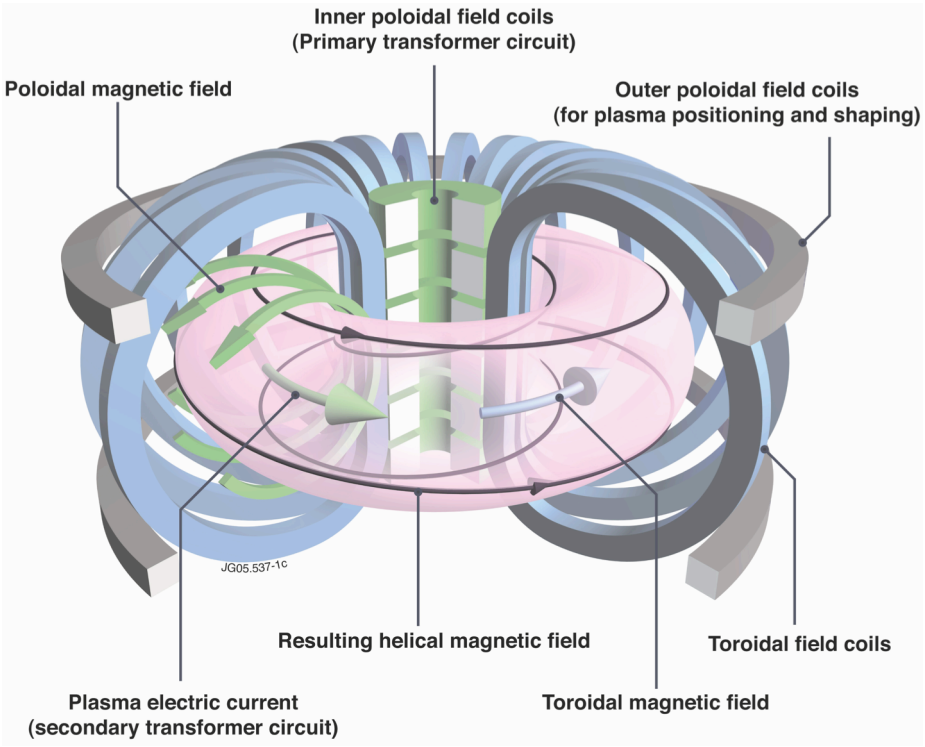

Fig. 1.24. Illustration of the nuclear fusion magnet principle: arrangement of magnetic field coils and the resulting magnetic field that confines the plasma.

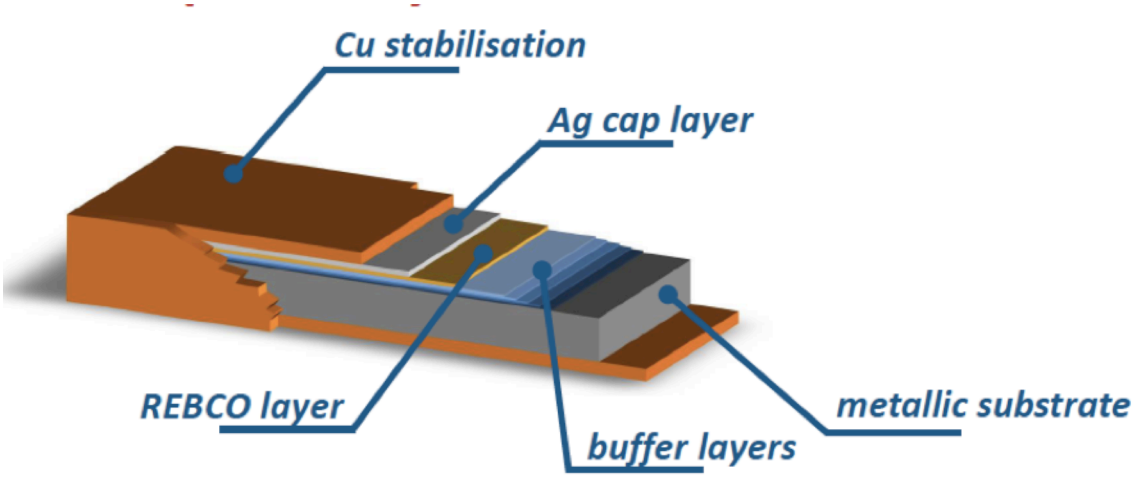

Fig. 1.25. Typical structure of coated conductor with YBCO layer on a metallic substrate.

power which is equivalent to the capacity of a medium size power plant. ITER laying the foundation for a Demonstration Fusion Power Reactor (DEMO) to follow ITER by 2050.

The control of the superconducting and mechanical properties of tapes and wires is necessary to establish a solid position of HTS as alternative materials with respect to Low Temperature Superconductors (LTS), especially when high-power applications are concerned. Many projects are being run for developing hybrid systems where HTS are used along with low-temperature superconductors to generate magnetic fields well above 23.5 T, which is the technological limit of LTS Nb_3Sn-based magnets [44,45]. Power applications, such as nuclear fusion magnets (Fig. 1.24), demand very strong vortex pinning capable to yield high values of the critical current density in high magnetic fields and low temperatures.

The second generation (2G) HTS coated conductors (CCs) consist of a metallic tape upon which the growth of oriented superconducting YBCO film is achieved through the epitaxial growth on an oriented buffer layer (Fig. 1.25). The thickness of YBCO layer is about ~ 1 μm in a ~ 100 μm thick tape. The metallic substrate ensures good flexibility to the tape, which, otherwise, would be damaged by bending, since YBCO is a ceramic material. Moreover, the metallic tape guarantees an alternative path for the current in case of quench. Since the YBCO film is grown replicating the

texture of the under-lying buffer layer, the latter must be highly biaxial textured (within < 3°) in order to avoid high misorientation angle grain boundaries in the superconducting film.

One of the methods to grow an oriented buffer layer is called IBAD (Ion Beam Assisted Deposition). In this process, a ceramic layer is deposited on a non-textured metallic tape in presence of an argon ion beam directed along a particular axis of the substrate. The resulting layer is highly textured and can be used as a template for the YBCO growth. A less expensive and faster method is called RABiTS (Rolling Assisted Bi-axially Textured Substrate). In this process the oriented buffer layer is obtained by epitaxial growth on textured tapes. The high degree of texture is obtained by rolling and recrystallization thermal treatment process [46].

Kilometer lengths of CCs have been successfully demonstrated and lengths of 150+ m with a minimum critical current of 350Acm^{-1} width at 77K and in self-field are currently available.

The improvement of YBCO-based Coated Conductors transport properties necessary for the increase of magnetic field performances at the same (low) operating temperatures [43,47], which will lead to many benefits of nuclear fusion reactors [48]. This can be achieved by the continuous development of epitaxial YBCO thin films.

The technological challenges of fusion energy are linked with the availability of suitable materials capable of reliably withstanding the extremely severe operational conditions of fusion reactors. Structural and functional materials of plasma-facing components of ITER and DEMO are exposed to intense neutron irradiation. In operational conditions further defects in a material structure are expected due to fusion neutron bombardments. Irradiation with 14.1MeV deuterium–tritium fusion neutrons releases significant amounts of hydrogen and helium as transmutation products that might lead to a degradation of structural materials after a few years of operation [49].

A lack of a fusion-relevant neutron source for materials testing is a major critical issue of the international fusion materials research. Conventional fission reactors, which produce neutrons with an average energy around 1-2 MeV, are used in order to the study the influence of irradiation, but they cannot adequately match the testing requirements for fusion materials [50], [51]. Neutrons with suitable fluxes and spectra for fusion materials testing, generated through Li nuclear reactions, are expected to be available by the middle of the next decade through International Fusion Materials Irradiation Facility (IFMIF) [50].

As a general rule, substantial damage production will only be made by "fast neutrons," which are generally defined as those neutrons of the entire spectrum having energies larger than 0.1 MeV. Lower energy neutrons ("epithermal" and "thermal" neutrons) do not generally lead to extended defects, but may create point defects or point defect clusters, which produce some disorder [52].

The experimental results over the last decades revealed that irradiation by fast neutrons can introduce pinning sites into high temperature superconductors, which enhance the critical current densities [51]-[55]. The introduced defects are randomly distributed within the volume of the superconductor, but only neutrons above certain energy will lead to defects, which are effective pinning centers. The study [51] shows that the neutron induced pinning centers might interact with the original pinning sites and the efficiency of the random pinning centers is varying not only with magnetic field, but also with its orientation. The number of pinning centers created by these neutrons or secondary radiation could be negligible compared to the density of defects created by fast neutrons. Yet the neutrons with lower energy can contribute to the formation of defects, mostly in the form of point defects or clusters of point defects (which may also be able to contribute to flux pinning). Since oxygen is the lightest atom in all HTS, oxygen displacements lead to two undesired side effects of neutron irradiation: firstly to a depression of T_c due to oxygen displacement from its chain or plane position, and secondly to the introduction of disorder in the CuO_2 planes resulting in a weakening of the intrinsic pinning effect [52], [56].

The study [51] shows that the influence of the fast neutron on J_c might vary with the neutron fluence. Whereas fluences of up to $4 \cdot 10^{21}$ m^{-2} improved J_c, higher

fluences start reducing J_c. However, coated conductors in that study show better J_c after irradiation to the ITER lifetime fluence than without irradiation. The experimental results in [57] revealed that the superconducting characteristics did not deteriorate upon irradiation.

One can conclude that unless neutrons do not severely damage the HTS material, this issue is not severe for what concerns pinning. The radiation effects will not present a serious challenge for the ITER magnets under the present design and construction specifications [52]. The neutron flux at the superconducting magnet is not so high (around 0.01 dpa), but the lifetime of the fusion reactor is limited by the irradiation damage of the superconducting materials and the insulator of the superconducting magnet [50]. Thus, knowledge of the radiation effects on superconducting fusion magnet components and potential materials damage is mandatory for a successful development of fusion energy applications and should be included in the further study of superconducting materials under operation conditions.

Chapter 2

YBCO growth and structural characterization

As it was mentioned in Chapter 1, only about a one hundredth of coated conductor volume is an YBCO superconducting layer and yet it provides all the superconducting properties for the whole tape. Thus, only advanced control of growth process, structure, transport properties, architecture and fabrication will guarantee a secure and unaltered performance of YBCO over a long period of time and compliance to the requirements for HTS applications. This Chapter discusses substrate and techniques used for growing the YBCO thin films and the main structural features of these samples. All the samples were grown in ENEA Research Centre (Frascati) within a long–term collaboration.

2.1 Growth of YBCO

2.1.1 Substrate

YBCO superconducting films show the highest critical current performance when the films are epitaxially grown on a substrate. The epitaxial growth process ensures a defined structural orientation of the film. For the present study, only samples grown by the epitaxial deposition of a thin film on a single crystal substrate were considered.

The choice of the substrate is crucial since the quality of the epitaxial growth directly depends on it and the substrate must satisfy several requirements [58]:

- **High chemical compatibility**

The substrate and the film should not chemically react with each other, especially at high temperatures typical of YBCO growing process (up to 850 °C) [58,59]. The substrate must also be unreactive in the oxygen-rich ambient, which is used for the growth [58].

- **High surface quality and substrate homogeneity**

The quality of the surface is one of the most important properties of a substrate since it is where the film–substrate interaction occurs. A uniform substrate surface is necessary to obtain homogeneous and uniform films. Hence, the surface roughness, cleanliness and smoothness are important parameters: they may have a significant impact on film nucleation. Consequently, morphology and structure of the resulting film may be affected.

- **High structural quality and compatibility**

One needs a high structural quality of the substrate in order to achieve high structural quality of the film grown on top of it. Impurity phase inclusions in the substrate will very likely affect the surface quality and ultimately the epitaxial quality as well. Thereby only single crystal substrates were used for this work.

- **High thermodynamic stability**

Any suitable substrate must be thermodynamically stable within a wide temperature range in order to prevent losses of adhesion or the formation of thermally induced cracks since the YBCO films are deposited at high temperatures (~ 850 °C), and then they work at very low temperatures (77 K and below).

- **Compatibility with microwave frequencies**

  Since in this study a complementary microwave measurement technique has been used to investigate in depth the flux pinning properties of YBCO (see Chapter 4), the compatibility of a substrate with microwaves should be considered. The substrate contribution becomes more and more important as YBCO layer thickness decreases since reduction of the thickness makes it partially transparent to a microwave electromagnetic field, which can reach the underlying material of a substrate. The substrate can therefore heavily influence the overall microwave response. Operation at microwave frequencies imposes the need for low substrate loss.

The most studied and most matching substrates for YBCO materials are typically oxides with the perovskite crystal structure, since the crystal structure of the YBCO compounds is closely related to the perovskite structure and it gives a large number of coincidence sites, thus making epitaxial growth likely (Fig. 2.1).

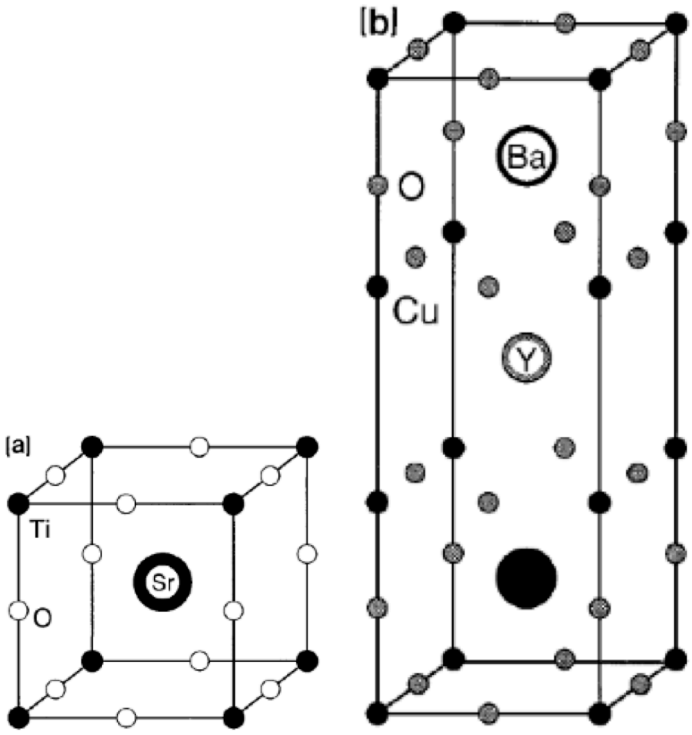

Fig. 2.1. (a) The perovskite crystal structure of $SrTiO_3$; (b) The crystal structure of $YBa_2Cu_3O_7$. $SrTiO_3$ has a small lattice mismatch with YBCO.

Strontium titanate ($SrTiO_3$, STO) is, perhaps, the most widely used substrate for YBCO films. It meets all the requirements mentioned above apart from full microwave compatibility (see Chapter 4), and it has a ready availability. It has a small mismatch with YBCO lattice parameters, defined as $(a_s - a_f) / a_s$, where a_s and a_f are substrate and film lattice parameters, respectively (Table 2.1). Its unit cell, shown in Figure 2.1, is cubic and persistent over the whole temperature range of interest.

Table 2.1 Lattice parameters and lattice mismatches $SrTiO_3$ with YBCO

	a (Å)	b (Å)	Δa/a (%)	Δb/b (%)	Crystalline structure
YBCO	3.8227	3.8872	\	\	cubic
$SrTiO_3$	3.905	3.905	+2.1	+0.46	cubic (perovskite-like)

In the present work all the samples were grown on $SrTiO_3$ substrates using two different techniques, which will be discussed next.

2.1.2 Pulsed Laser Deposition (PLD)

The deposition of HTS thin films can be achieved by means of several physical or chemical techniques. The first physical technique is: Pulsed Laser Deposition (PLD), which has proven to be a method of choice in the fabrication of high-T_c thin films, as the stoichiometric transfer of material from target to film gives precise control of the cation ratio [59,60]. Deposition and formation occur simultaneously during this *in situ* process. This technique utilizes the local heating produced by a laser beam focused on a quasi-stoichiometric target of the material to be deposited, and the resulting evaporation of the material. The vapor (plume) is collected on a substrate, placed at short distance (few centimeters) from the target, where it condenses (Fig.2.2).

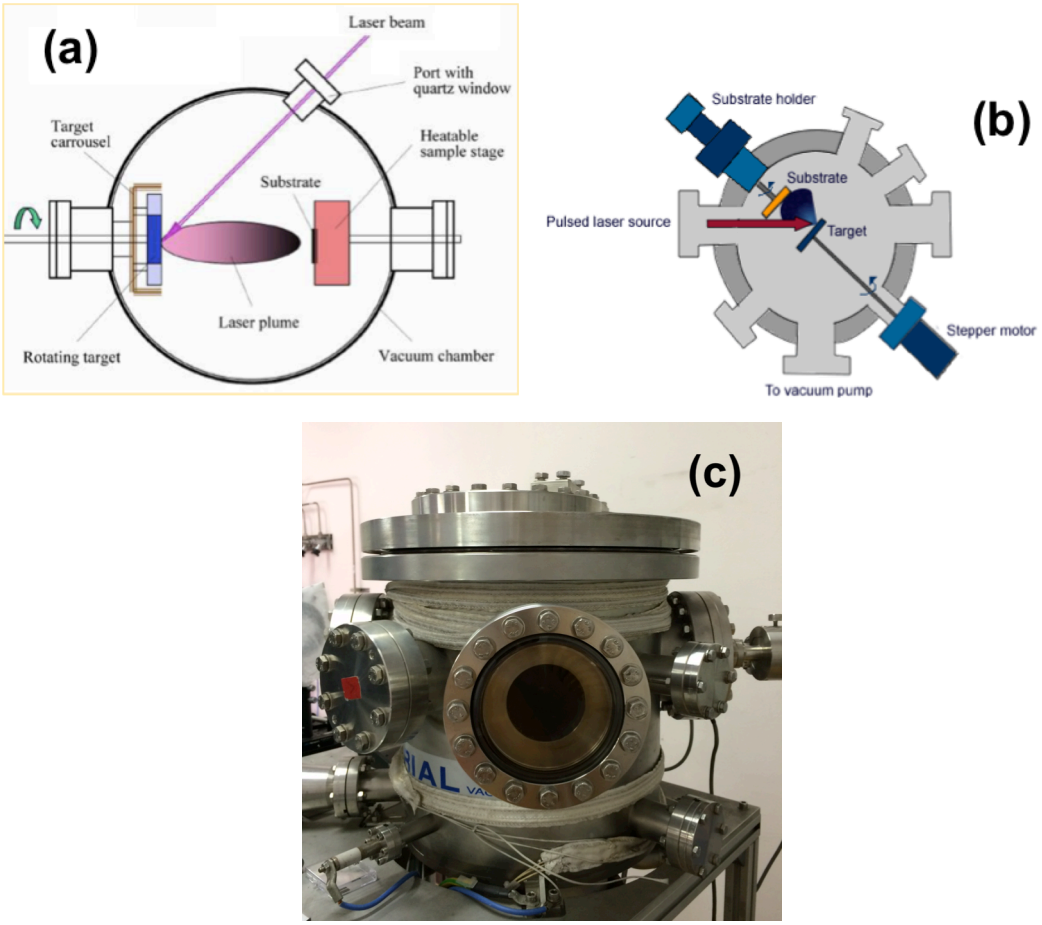

Figure 2.2 (a), (b) Sketch of the inside of the vacuum chamber for PLD process. (c) PLD setup used in the ENEA research Center (Frascati).

Pulsed laser deposition has been successfully applied to an extremely wide range of materials [61–64]. It is, however, a complex method with many experimental parameters. The optimal laser energy and spot size, target–substrate distance and ambient gas pressure are interdependent quantities, which must be chosen to give an ablation plume of an appropriate size, shape and composition. It is also important to ensure that the substrate is positioned correctly in this plume. More details about the PLD method can be found elsewhere [59], [60], [65–67].

As it was observed in recent works [62], [28], a repetition rate of the laser has an effect on some of the properties, such as critical temperature. T_c decreases for higher repetition rates (Fig. 2.3). The reduction in T_c might be avoidable by adjusting other

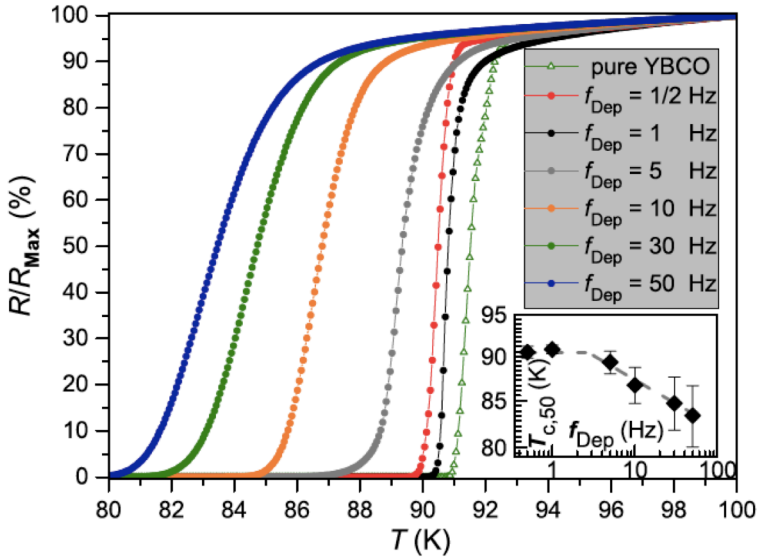

Fig. 2.3. Relative resistance over applied temperature for BYNTO: YBCO films grown at laser repetition rates between 0.5 Hz and 50 Hz, as taken from [28].

PLD parameters, such as deposition temperature, energy density, oxygen partial pressure and target-substrate distance.

Samples for present work were obtained by the PLD technique using mixed YBCO targets with addition of 5 mol. % $BaZrO_3$, 7 mol.% $BaZrO_3$ (BZO), and 5 mol.% $Ba_2Y(Nb/Ta)O_6$ (i.e 2.5 mol.% Ba_2YTaO_6 + 2.5 mol.% Ba_2YNbO_6, BYNTO). All thin films were epitaxially grown on (001) $SrTiO_3$ (STO) single-crystal substrates. Targets were ablated using a 308 nm XeCl excimer Laser (Lambda Physik 110i cc) adjusting the laser energy in the range 100 ÷ 130 mJoule with fluence of ~ 2 J/cm^2 and the repetition rate f_L of 10 Hz in a 300 mTorr oxygen

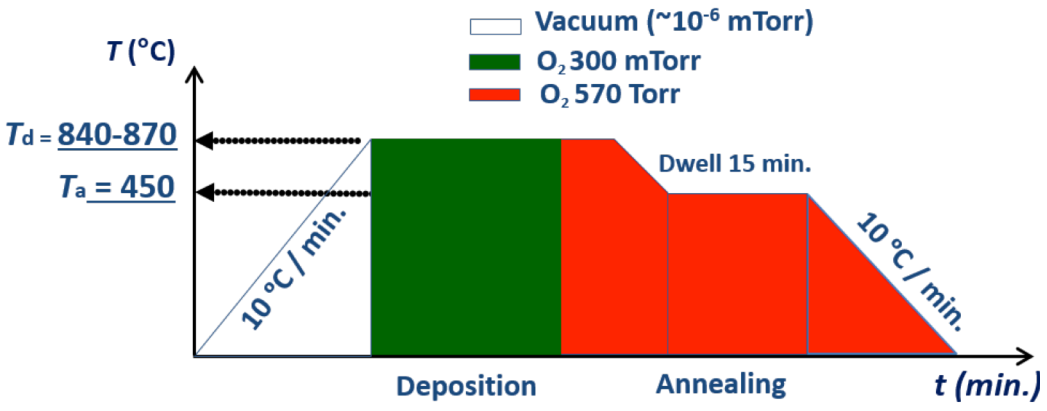

Fig. 2.4. A schematic diagram of deposition and heat treatment processes of YBCO with BZO and BYNTO inclusions.

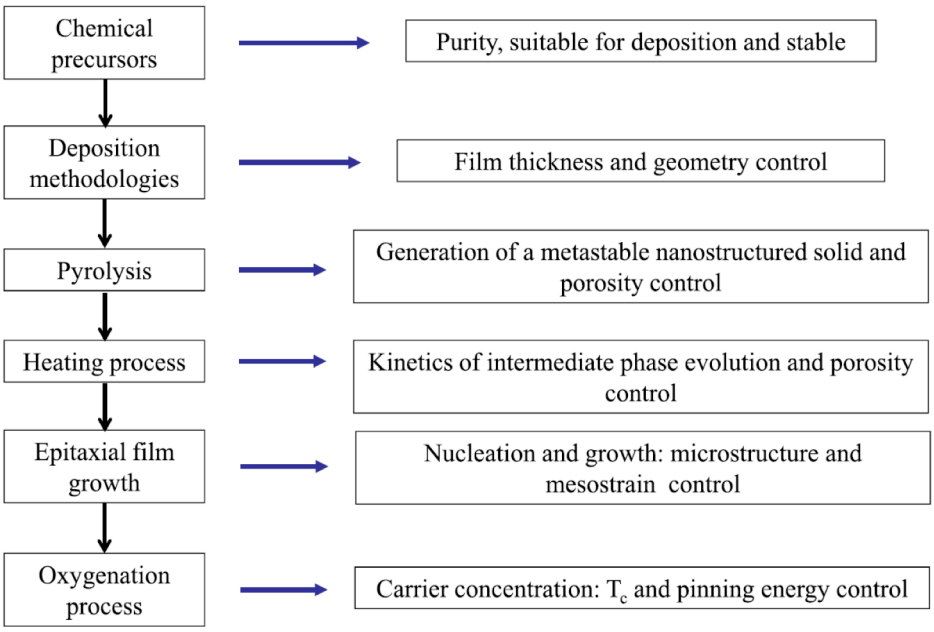

Fig. 2.5. General scheme of the CSD different technique with the processing steps required to prepare YBCO thin films and the main parameters controlled in each step.

atmosphere at temperature 840 °C and 870 °C for BYNTO and BZO inclusions, respectively, with following annealing at 450 °C (Fig. 2.4). The thickness of the films was in the range of 200-300 nm.

2.1.3 Metal Organic Decomposition (MOD)

The way to commercialization of HTS, in particular YBCO, relies on the production process by Chemical solution deposition (CSD) methods. One of them is Metal Organic Decomposition (MOD) technique [69–70]. This *ex situ* (the YBCO crystal structure is grown after the film deposition) method has become one of the most promising alternatives towards successful development of long length YBCO coated conductors.

The greatest progress has been achieved based on the use of trifluoroacetate (TFA) solutions as metal–organic precursors in the growth of YBCO [71]. A fluorine coating solution contains a stoichiometric mixture of Y, Ba and Cu trifluoroacetates, obtained by the reaction of the corresponding acetates with trifluoroacetic acid. These precursors permit the formation of BaF_2, instead of $BaCO_3$. The BaF_2 phase is

stable at high temperatures (T ~ 1200 °C) but can react at lower temperatures (about 700-800 °C) even in a humidified oxygen atmosphere. The phase reactivity is better than in the $BaCO_3$ phase when it is mixed with CuO and Y_2O_3 to form the YBCO phase [73].

A general scheme of the YBCO film growing process from TFA precursors is presented in Figure 2.5. The first step is to prepare TFA precursors of adequate purity, with the rheological parameters adapted to the selected deposition technique, which remain stable, i.e. no precipitates are formed. Several solution deposition methods can be used nowadays in CSD, allowing one to achieve a close control of the film thickness where the rheological properties of the solutions are properly tuned through the use of suitable additives. The next important step is to pyrolyze properly the deposited solutions. Pyrolysis temperatures are usually relatively low (T ~ 300–400 °C). This step leads to a metastable solid, which should maintain homogeneity to allow the growth of high-quality epitaxial film. To allow that, the films are further treated at about 800 °C in a humid oxygen–nitrogen mixture. Another fundamental processing step is the nucleation and growth of the YBCO layer, including the control of the growth rate and a high epitaxial quality. A final parameter which has been shown to be effective in achieving some control of the thermo-oxidative decomposition kinetics of the YBCO–TFA precursors is the oxygen partial pressure. Obtaining large-area uniform YBCO films with this process is difficult because the temperature and partial oxygen pressure must be simultaneously controlled precisely in order to decompose $BaCO_3$ [29], [76].

The thermal treatment time of the pyrolysis process, as long as 20 hours, is considered as one of the main drawbacks for the scaling-up of the process for coated conductors with the TFA-MOD method. A remarkable decrease of the pyrolysis time can be obtained through a reduction of the amount of water in the precursor solution using anhydrides of TFA and operation at reduced oxygen pressure. Since the rate of hydrofluoridric acid elimination is one of the parameters influencing the pyrolysis time, modified TFA YBCO precursors with low fluorine content have been successfully proposed for short pyrolysis processes [77–79]. They also allow one to minimize the environmental concerns and reduce the processing time [29], [80].

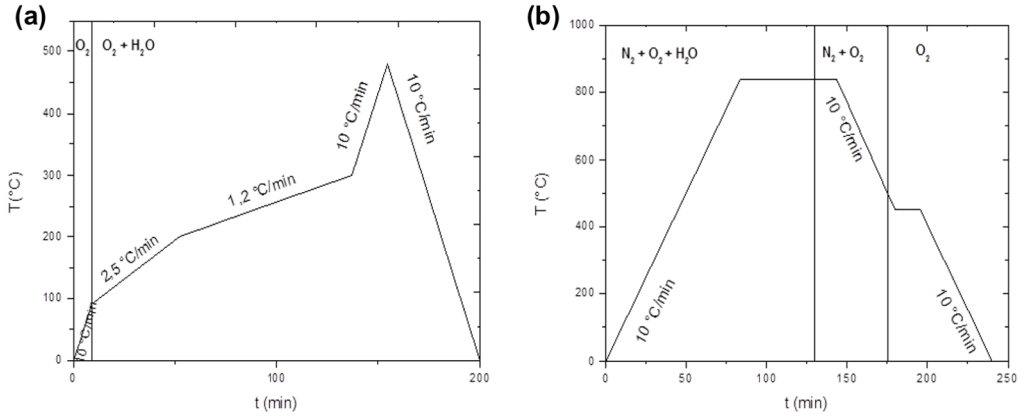

Fig. 2.6. (a) A schematic diagram of pyrolysis process and (b) heat treatment process of YBCO by MOD.

For this study, pristine YBCO samples were grown by MOD chemical method using low fluorine coating solution, which included yttrium acetate $Y(CH_3COO)_3 \cdot 4H_2O$, barium trifluoroacetate $Ba(CF_3COO)_2 \cdot H_2O$, and copper acetate $Cu(CH_3COO)_2 \cdot H_2O$ and corresponded to the 1:2:3 stoichiometry. The final solution concentration of YBCO was 0.2 M (M = mol·l^{-1}) and the total metal concentration was C = 1.2 M. Propanoic acid was used as solvent. YBCO solution with addition of $BaZrO_3$ was prepared by adding barium trifluoroacetate and zirconium acetylacetonate precursors, in stoichiometric proportion to reach 5 mol.% of doping. YBCO precursor solutions were spin-coated at a spinning rate of 3000 RPM for 60 s on the $SrTiO_3$ single crystal substrates. To obtain epitaxial YBCO film growth, samples were pyrolyzed at 480 °C under flowing humid oxygen, then heated to 840 °C for 50 min using a rate of 10 °C · min^{-1} in a humid mixture of nitrogen and oxygen ($N_2 : O_2$ = 2400 : 1) and for the last 10 min - in the same dry mixture (Fig. 2.6). Further details on precursors solution preparation, pyrolysis, firing processing conditions, and BZO solution preparation are described elsewhere [34], [68], [80], [81]. The films thickness was ~ 100 nm.

2.2 Structural analysis

Extensive theoretical and technological efforts have led to the development of composite $YBa_2Cu_3O_{7-x}$ films with improved vortex pinning strength and increased J_c by means of different heteroepitaxial second-phase additions. Very effective and

controllable APCs were obtained by nanoinclusions in YBCO films grown by both Pulsed Laser Deposition and Metal Organic Deposition techniques.

As mentioned in Chapter 1, Artificial Pinning Centres (APCs) are very effective to increase pinning properties. For that reason, different compositions could be used to produce YBCO films with secondary phases, such as $BaZrO_3$ and $Ba_2Y(Nb/Ta)O_6$ to generate columnar defects or isotropic nanoparticles.

Scanning Transmission Electron Microscopy (STEM) images, used for structural analysis, have been done by Dr. Sergey Rubanov (The University of Melbourne, Australia) for PLD YBCO 5% BZO, MOD pristine YBCO and MOD YBCO 5% BZO. STEM characterization of PLD YBCO 7% BZO and PLD YBCO 5% BYNTO samples has been done by A. Meledin, M. Pfannmoller and G.Van Tendeloo (EMAT Research Group, University of Antwerp, Belgium).

In the following, the structural features of the grown two sets (PLD and MOD) of samples will be discussed.

2.2.1 PLD samples

Figure 2.7 presents the cross-sectional dark-field Scanning Transmission Electron Microscopy (STEM) images of YBCO thin films with addition of 5 mol. % $BaZrO_3$, 7 mol.% $BaZrO_3$, and 5 mol.% $Ba_2Y(Nb/Ta)O_6$.

The self-organized columns of BZO nanoparticles can be clearly observed in the YBCO film with 5 mol. % BZO content (Fig. 2.7 (a)). From the planar view (Fig. 2.7 (b)), the average size of BZO particles can be evaluated as 5–10 nm, while the density of columnar defects was ~ 600 μm^{-2}. One part of the columns grows from bottom to top of the YBCO film, the other part is either relatively short and does not go through the whole film or tilted and crossed by the sample plane and thus just partially visible on the image. The YBCO layer is approximately 130 nm thick.

High-Angle Annular Dark Field Scanning Transmission Electron Microscopy (HAADF STEM) for YBCO – 7% BZO was performed on an FEI Titan electron microscope operated at 300 kV.

Before the TEM experiments the specimen was cleaned by plasma cleaner. The sample was prepared via Focused Ion Beam (FIB). During the preparation process the Au protective layer was deposited on top of the film. The morphology of this thin film (Fig. 2.7 (c) and Fig. 2.7 (d)) shows the YBCO matrix containing self-assembled *c*-axis elongated BZO nano-columns, which can be seen as lighter features elongated parallel to the YBCO film growth direction and marked with red arrows (Fig. 2.7 (c)). This is a typical feature when YBCO is grown by PLD technique with the addition of perovskite compounds, such as $BaZrO_3$ [36], [82], [83].

The STO/YBCO interface (~20 nm) has a highly distorted YBCO layer and mainly consists of Y124 and Y247 phases. These phases form short intergrowths. The BZO columns start after this layer and grow through the whole YBCO layer. However, in some areas the nanocolumns are interrupted by the YBCO matrix. In a few cases BZO columns start with Y_2O_3 particles (indicated by white arrows on Fig. 2.7 (d)). BZO columns are ~7 nm thick and are distributed with ~ 1 column per 20-22 nm density in the cross section as evaluated from TEM images. The thickness of the YBCO film is around 200 nm.

For YBCO/BYNTO sample, HAADF STEM was performed on an FEI Titan electron microscope operated at 120 kV and Bright Field Transmission Electron Microscopy (BFTEM) was performed on an Osiris FEI microscope operated at 200 kV. The sample was prepared via Focused Ion Beam (FIB). During the preparation process Pt protective layer weas deposited on top of the film. The specimen was cleaned by plasma cleaner before TEM.

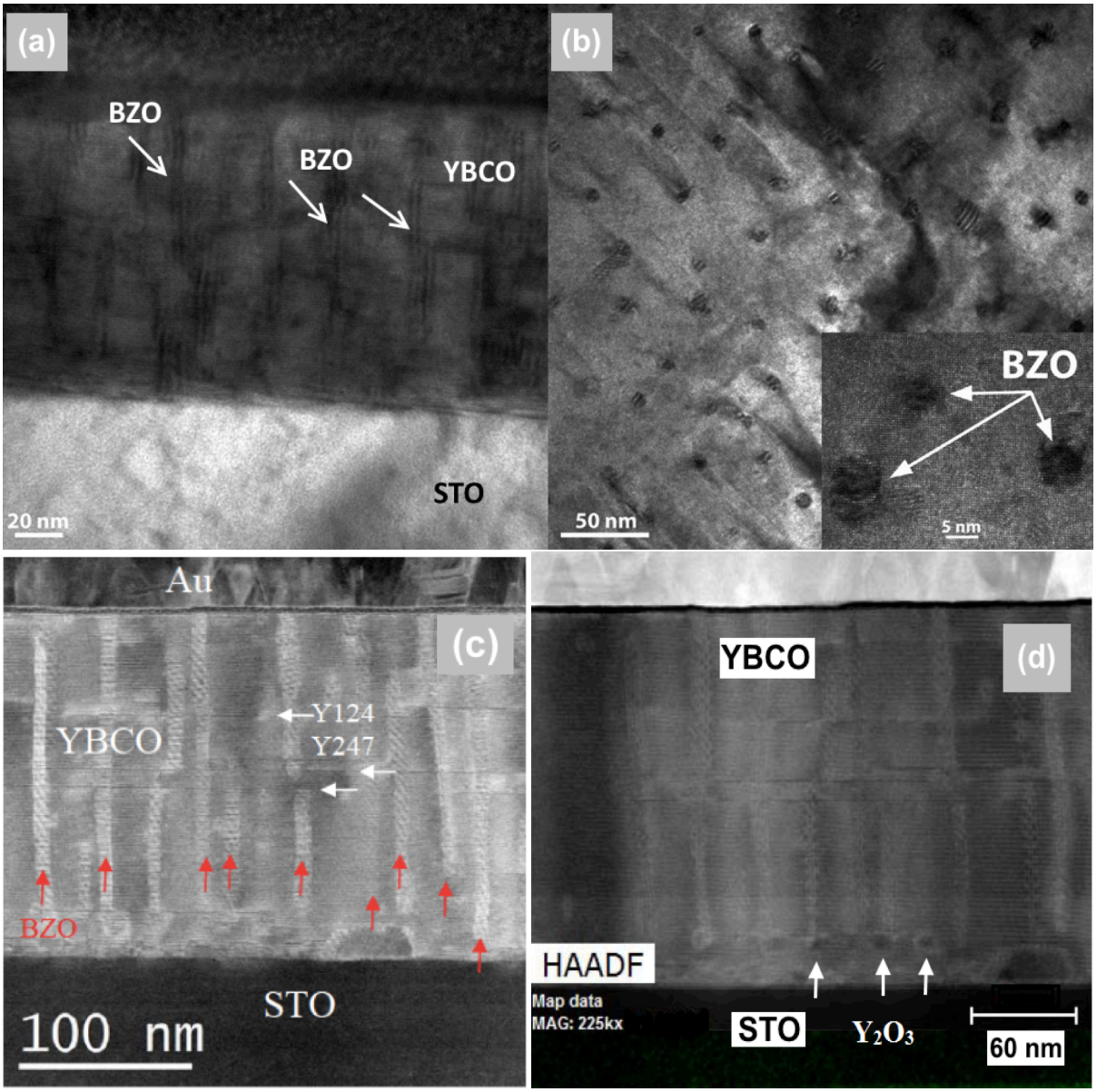

Fig. 2.7 Scanning transmission electron microscope (STEM) dark field cross-sectional view (a) and planar view (b) for PLD YBCO - 5 mol % BZO film. Inset in (b) shows a magnified planar view of BZO nanocolumns terminations. (c) ADF STEM image and (d) high-resolution HAADF STEM image of the PLD YBCO-7 mol.% BZO thin film.

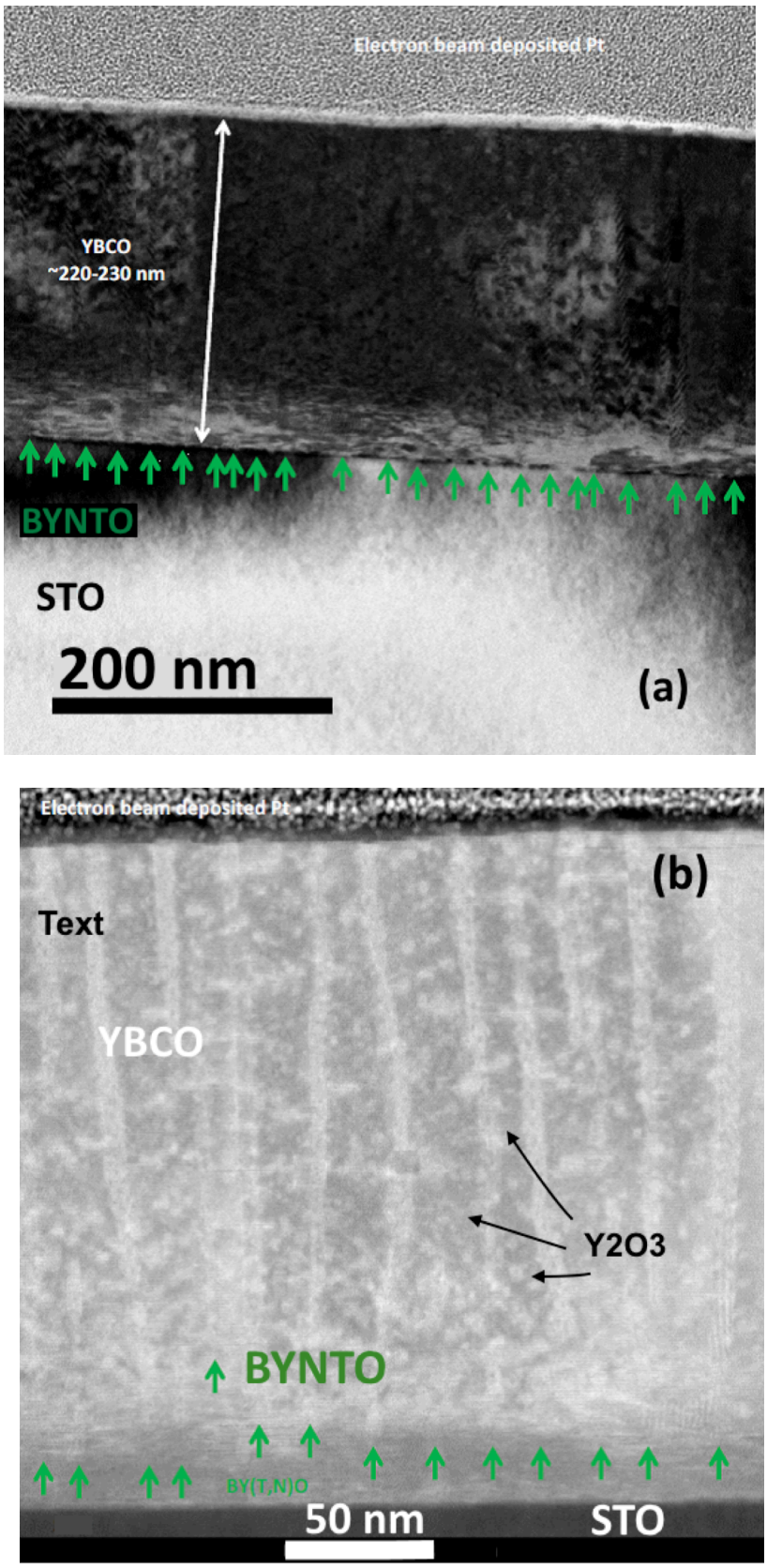

Fig. 2.8 (a) BFTEM cross-section image of the PLD YBCO/BYNTO film on STO substrate. The BYNTO columns are marked by green arrows. (b) HAADF STEM image of the YBCO layer of the film. The BYNTO column size is about 5 nm.

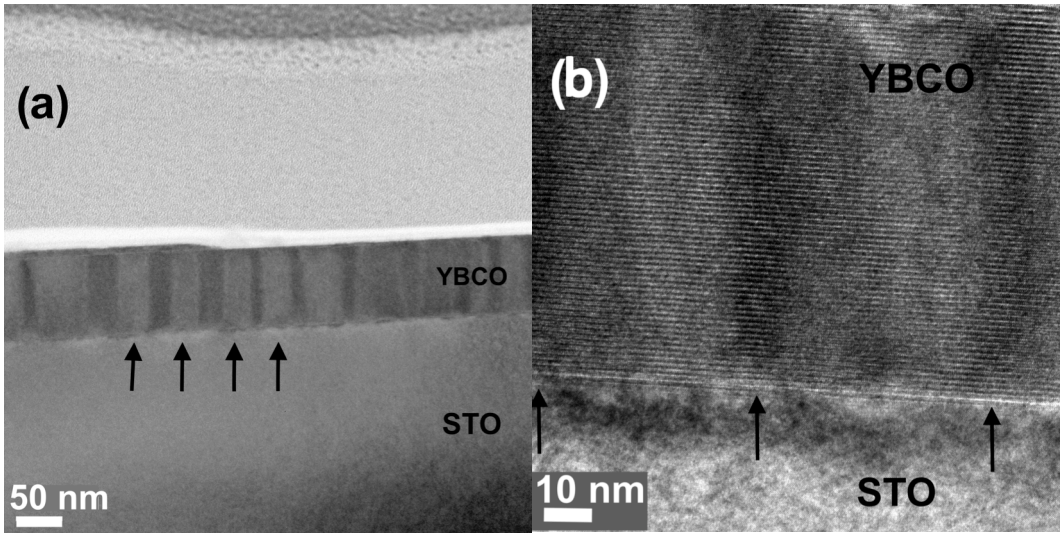

Fig. 2.9 (a) A cross-sectional bright-field TEM image of the pristine MOD YBCO. Black arrows indicate twin domains, which are visually similar to the structure of BZO nano-columns, but represent sections of planar (2D) defects. (b) High-resolution TEM image of the pristine MOD YBCO. Twin boundaries (black arrows) are created by the interaction of twin domains along (110) plane.

Figure 2.8 presents the cross-section images of typical YBCO/BYNTO structure [28], [62]. The YBCO matrix contains the *c*-axis oriented BYNTO nano-columns with a thickness of ~ 5 nm, which are distributed with ~ 1 column per 20 nm density (Fig. 2.8 (a)). However, a thin layer of highly distorted YBCO is present on some interface regions. In these areas, BYNTO columns are starting above the distorted YBCO layer. The HAADF-STEM contrast image (Fig. 2.8 (b)) visualizes the presence of Y_2O_3 particles and indicates that the columns are continuous and one dimensional in the YBCO matrix without any sign of segmentation. They start at the YBCO/STO interface and run through the whole YBCO layer. The thickness of the YBCO film is around 220-230 nm.

2.2.2 MOD samples

Cross-sectional TEM images, presented in Figure 2.9, reveal a compact, almost defect-free morphology of the pristine MOD YBCO thin film. The observed contrast

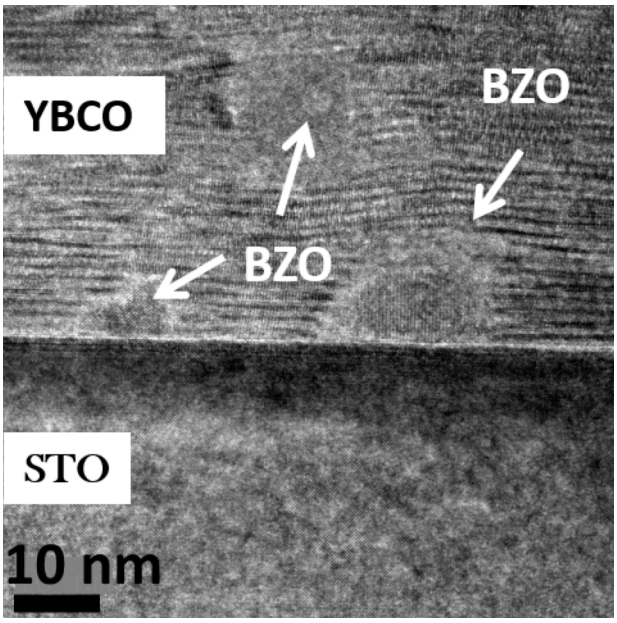

Fig. 2.10 A cross-sectional high-resolution TEM image of the MOD YBCO 5% BZO. White arrows indicate BZO nanoparticles.

in Fig. 2.9 (a) and (b) is the result of a mutual interaction of twin domains of ~ 30 nm size along (110) plane and corresponds to twin boundaries (TBs). They can be noticed throughout the film thickness as they are formed during the tetragonal-orthorhombic phase transition that takes place in the film at 480 ˚C upon oxygenation process. Similar pristine YBCO structures containing TBs have been found in many previous studies [35], [84-89], for samples grown on different substrates. As it has been discussed in earlier studies [84], [85], [89–91], TBs can act as extended defects trapping vortices along the TBs length. The twin planes structure, e.g. its vertical coherence, density and spacing, needs to be considered in the analysis of flux pinning. The TBs width in the studied film was ~ 9-10 nm (Fig. 2.9 (b)), which is an average size and consistent with other studies [35], [84], [85], [87]. The thickness of the YBCO film is around 100 nm.

The YBCO 5% BZO film shows the typical morphology of samples produced by MOD technique [29], [87], [91]. In this sample, a high density of nanoparticles is found with the size of ~ 10-15 nm.

The High-resolution TEM image shows that some of the BZO nanoparticles grow at the interface with the single-crystal substrate (Fig.2.10). The thickness of the YBCO film is around 100 nm.

2.3 Summary

In this Chapter, the YBCO growth processes and the structural features of grown samples have been analyzed. It was shown that the choice of a substrate is crucial since the quality of the epitaxial growth directly depends on it and that the substrate must satisfy several requirements. Strontium titanate $SrTiO_3$ with the perovskite crystal structure is a substrate of choice for the present study and all the samples have been grown on it.

Two methods have been used to grow the samples - Pulsed Laser Deposition (PLD) and Metal Organic Decomposition (MOD) techniques. The first technique has proven to be a method of choice in the fabrication of high-T_c thin films, as the stoichiometric transfer of material from target to film gives precise control. The second method, MOD, is one of the most promising alternatives towards successful development of long length YBCO coated conductors.

Structural analysis of PLD samples reveals YBCO films with successfully introduced secondary phases, such as $BaZrO_3$ and $Ba_2Y(Nb/Ta)O_6$, which produce columnar defects or isotropic nanoparticles.

Cross-sectional TEM images of a pristine MOD YBCO thin film reveal a compact, almost defect-free structure with noticeable twin boundaries throughout the film thickness. YBCO 5% BZO film shows the typical morphology of the samples produced by MOD technique with introduced nanoparticles with the size of ~ 10-15 nm.

In the next chapters I will present and discuss an extensive electrical characterization of all the samples shown here.

Chapter 3

DC electric transport properties

In this Chapter, I present the most important and extensive part of my results. In order to explore the different pinning properties of different nanoinclusions, the detailed experimental study of $YBa_2Cu_3O_{7-x}$ transport properties by the DC current transport measurement technique has been done. The obtained characteristic data, such as the critical temperature and the temperature dependence of resistivity, angular and in-field dependences of critical current density, and the pinning force density as a function of the applied magnetic field are discussed in this Chapter. Preliminary analysis is given for all the samples under study.

The DC electric transport properties of the PLD and MOD derived films with different introduced second phases have been investigated by means of a standard four-point measurement method. The critical current was obtained by recording the $I - V$ characteristics, i.e. ramping a bias current up and recording the induced voltage drop until a limiting value is reached. This method requires photolithography patterning to obtain a four-point bridge geometry. Low contact resistance is required to avoid sample heating during the measurements. This Chapter describes the pattern preparation of the YBCO thin films and the DC current transport measurement technique, following by the description of the obtained DC electric transport characteristics. All the pattern preparation and DC electric transport measurements were performed at the ENEA Research Centre (Frascati).

3.1 Pattern preparation

Since electrical transport measurements consist of the application of an external DC current along the film and the measurement of its voltage drop, one needs to minimize the electrical resistance between the sample and the external wires, e.g. by

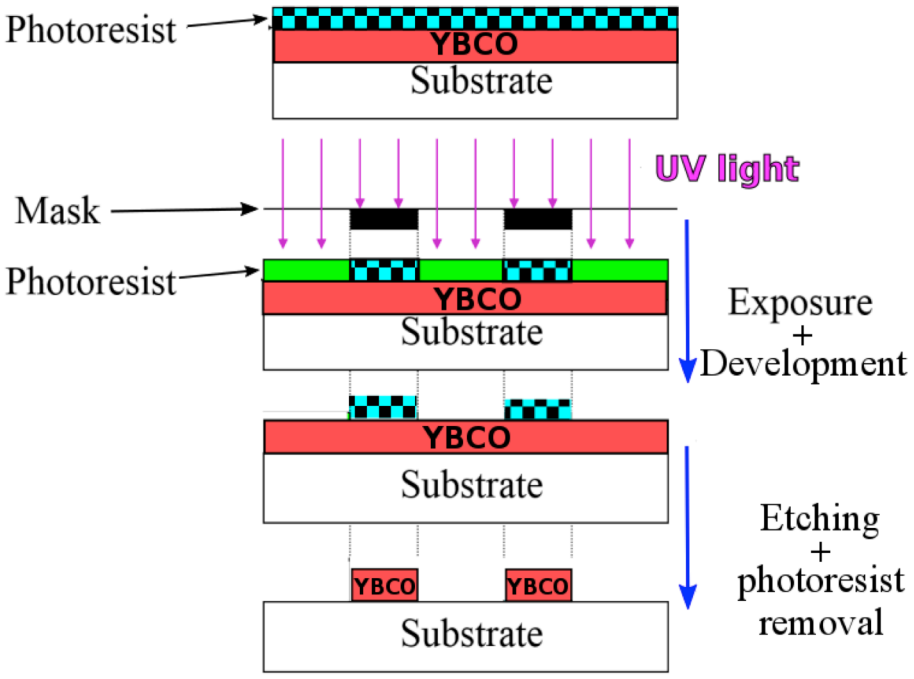

Fig. 3.1 A sketch of the photolithographic patterning process of an YBCO film with positive photoresist

preparing suitable electrical contacts with a deposition of a noble metal on top. Prior to that procedure, samples have to be patterned. The patterned bridges of YBCO films on a substrate need to have a small cross-section, which help to confine the electrical current. Thus, the transport properties could be easily measured at relatively low applied currents, and the sample under study can reach its critical current density ($J_c = I_c / S$, where I_c is the critical current and S is the cross-section of the bridge).

The patterning process includes two stages: the definition of the pattern geometry on the surface of the film by means of the optical projection of a designed mask, and the etching process in order to remove the film out of the pattern. The process is carried out with the standard UV photolithography, which consists of transferring geometric shapes obtained on a mask to the film surface.

The UV photolithography includes few steps, as schematically shown in Figure. 3.1:

1. The film surface is chemically cleaned to remove any impurities and particulates. Then, a special material, the photoresist, is deposited to the film surface by spin coating in a thin uniform layer.
2. A following heating (soft-baking process) of the sample at ~ 100 ^{o}C for 150 seconds allows removing almost all of the organic solvent of the photoresist, which enables the photoresist coating to be photosensitive.
3. In the present case, so-called positive photoresist has been used, and the area, corresponding to the film material to be removed, is exposed to UV light. The UV light changes the chemical structure of the photoresist so that it will be more soluble on the next step. In this work, samples have been patterned using only the positive photoresist AZ 5214 E, which was spun for 30 s at 3000 rpm in order to obtain a ~2 μm thin layer.
4. The exposed photoresist is then washed off by the developing solution (sodium hydroxide based Microposit 351 developer in deionized water with 1:4 ratio). The remaining part is an exact copy of the pattern for the YBCO film.
5. The following step is a hard-baking process at 110 ^{o}C for 300 s, which hardens the photoresist and improves adhesion of the photoresist to the YBCO film surface.
6. At the etching stage, the uncovered material is removed. There are two major kinds of etching: dry etching and wet etching. Wet etching utilizes liquid chemicals or etchants to remove materials from the substrate. The samples in this study were wet etched with the solution of 0.3% nitric acid in deionized water.
7. Finally, the rest of the photoresist is removed with acetone. The obtained film pattern is shown in Figure 3.2.

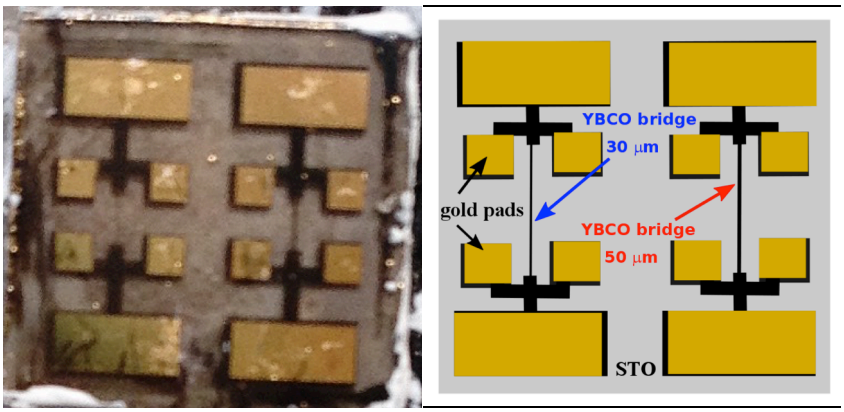

Fig. 3.2 (Left) A photograph of a real patterned YBCO film. (Right) A detailed schematic representation of the patterned YBCO film.

Each final patterned film, presented on Fig.3.2, has two YBCO bridges with the length of 1 mm and the width of 30 μm and 50 μm. The bridge is provided with four voltage contact pads and two current contact pads. The ~ 0.5 μm thick gold pads were deposited by e-beam in order to improve the contact electrical resistance.

3.2 DC electric transport measurement technique

A standard DC four-point contact method for current-voltage (I–V) measurements was used to study the electric transport properties. The patterned samples were mounted on a one-axis-angle variable sample holder (Fig. 3.3) and loaded in a helium gas flow cryostat provided with a 12 T superconducting magnet (Fig. 3.4). The magnet consists of a number of concentric solenoids sections. Each section is wound with a combination of multifilamentary superconducting wires of niobium titanium (NbTi) in the low field region followed with inner coil sections wound of

Fig. 3.3. A photograph of the sample holder used in the DC transport measurements.

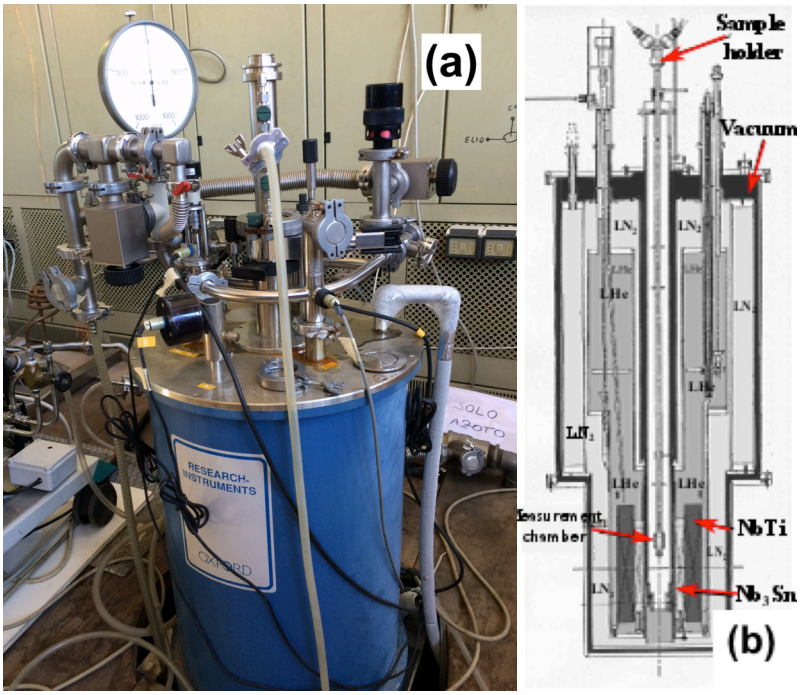

Fig. 3.4. (a) A photograph of the cryostat at ENEA Research Centre (Frascati). (b) A schematic representation of the cryostat section.

niobium tin (Nb_3Sn) in the high field region (up to 12 T). A variable temperature insert (VTI) in the cryostat provides centre location for the sample holder inside the magnet. The temperature inside can be varied over the range of typically from 4.2 K to 300 K, using helium gas flow. The magnetic field was applied at different angles θ to the surface of the films. Here θ is defined as the angle between a magnetic field

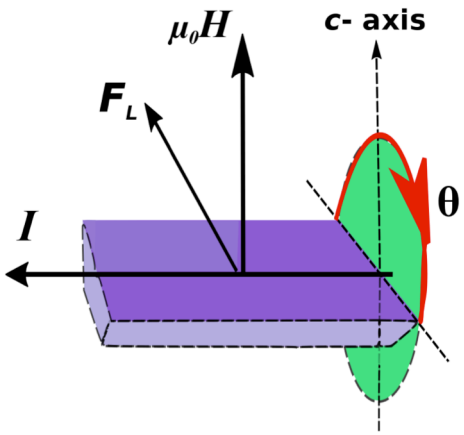

Fig. 3.5. A scheme representing the angle θ between a magnetic field H and the c-axis of a sample

orientation and the *c*-axis of a sample (Fig. 3.5). A sample is always mounted in such a way that at any θ the angle between the applied field and the transport current is fixed at 90° (maximum-Lorentz-force configuration). Critical current values have been obtained from the *I-V* curves using the 1 $\mu V \cdot cm^{-1}$ criterion.

3.3 Transport properties of PLD films

In this section, the description of obtained DC transport measurement results is given for PLD samples prepared according to the procedure described earlier in this Chapter. All the measurements of critical current density dependence on the applied magnetic field were performed at a fixed field orientation, H // *c*-axis of the film ($\theta = 0^o$). All the angular dependencies of J_c were obtained at fixed fields and angles varied from - 100º to + 100º degrees (Fig. 3.5).

A summary of the characteristic parameters obtained for all the samples in this thesis is given in Table 3.1.

Table 3.1 The characteristic parameters of the studied samples

Sample	**T_c, K**	**$J_{c\,(0)}$ @ 77 K (MA/cm^2)**	**F_p^{max} @ 77K (GN/m^3)**	**H_{irr}, T**	**α @ 77 K**
PLD YBCO – 5% BZO	89.7	1.59	6.2	8.5	0.23
PLD YBCO – 7% BZO	89.5	1.16	3.7	9.5	0.30
PLD - 5%BYNTO	88.5	3.18	11.5	11.1	0.28
MOD pristine YBCO	90.1	2.07	1.78	7.0	0.6
MOD YBCO - 5% BZO	89.7	0.92	1.63	6.6	-
MOD YBCO - 8% BZO	87.5	0.70	1.33	5.3	-

3.3.1 PLD YBCO films with $BaZrO_3$ nano-columns

The temperature dependence of the PLD YBCO – 5% BZO sample resistivity ρ is plotted in Fig. 3.6. The curve exhibits a linear dependence as a function of the temperature and the resistive transition is quite steep. The sample with introduced BZO APCs exhibits a critical temperature value T_c = 89.7 K, which has been evaluated from the zero resistance temperature. These results indicate homogeneous and high-quality film.

Figure 3.7 presents the field dependences of the critical current density, $J_c(H)$, at different temperatures. At 77 K the doped PLD sample exhibits the typical features of PLD YBCO described in different previous studies [33], [92], [93], [97]: a plateau region up to about μ_0H = 0.01 T, that corresponds to a region where J_c is independent on H, and that is usually linked with a single-vortex pinning regime. This plateau is usually observed in PLD films. In the following region $J_c(H)$ follows a power-law with $J_c \sim H^{-\alpha}$. Then, after a kink at approximately 1.5 T, a sharper decrease in J_c appears.

A power-law $J_c \sim H^{-\alpha}$ is often observed, depending on the pinning regime. The theoretical value of the coefficient α in case of pinning from planar defects is

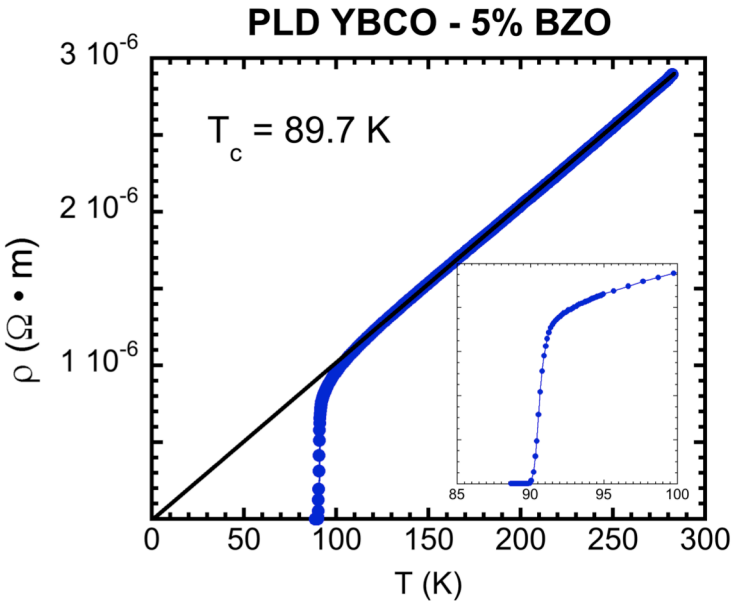

Fig. 3.6. Temperature T dependence of the resistivity ρ measured for PLD YBCO – 5% BZO film. T_c has been evaluated as the zero resistance temperature. The black straight line represents the normal state resistivity. In the inset the resistive transition region has been magnified.

reported as $\alpha = 0.5$ for pristine YBCO [88], [89], [94], [95], [97]. In case of YBCO containing artificial pinning centres (APCs), the coefficient α is usually smaller. In the present PLD YBCO – 5% BZO sample, the coefficient $\alpha = 0.23$ at 77 K, which is consistent with previous findings in PLD grown samples with $BaZrO_3$ nano-columns [88], [92], [97]. A J_c enhancement is observed as the temperature decreases, especially at high fields $\mu_0 H > 3$ T.

The normalized pinning force density ($F_p = \mu_0 H J_c$) dependence on the applied magnetic field at 77 K and 65 K is presented on Figure 3.8. One can see the difference in F_p peaks: the peak corresponding to the maximum F_p value ($F_p^{max} = 6.2$ GN/m^3 at 77 K) is much broader at 65 K, than at 77 K. This indicates the increasing effectiveness of pinning due to BZO nano-columns, as the temperature decreases.

The irreversibility field H_{irr} was evaluated as the field value above which the pinning force density decreases to 1/100 of its maximum. For this sample, at 77 K we get $H_{irr} = 8.5$ T.

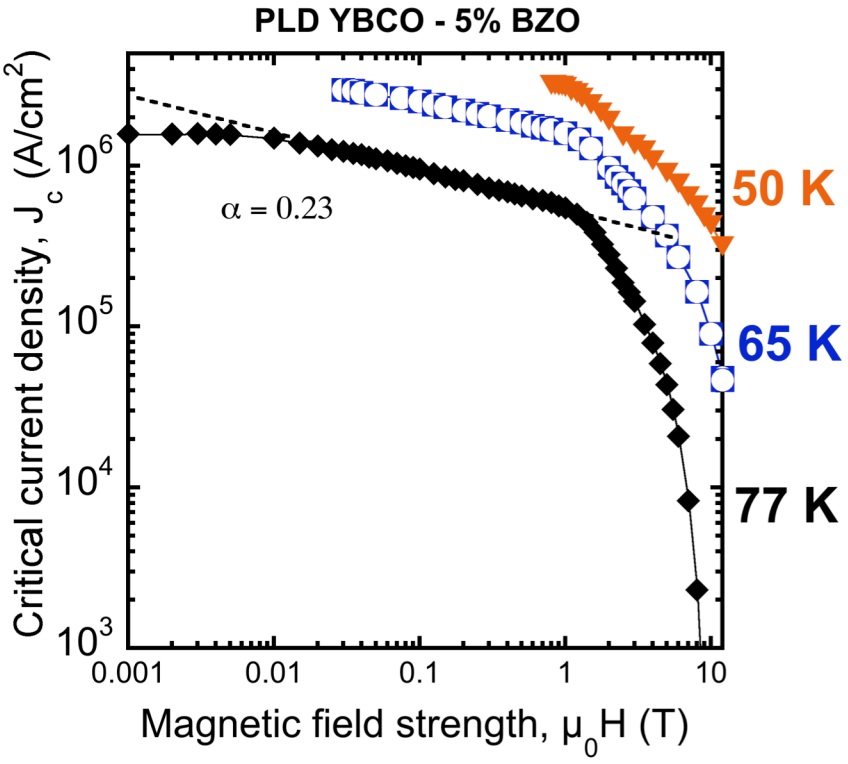

Fig. 3.7. Critical current density as a function of the applied magnetic field at several temperatures for YBCO – 5% BZO film.

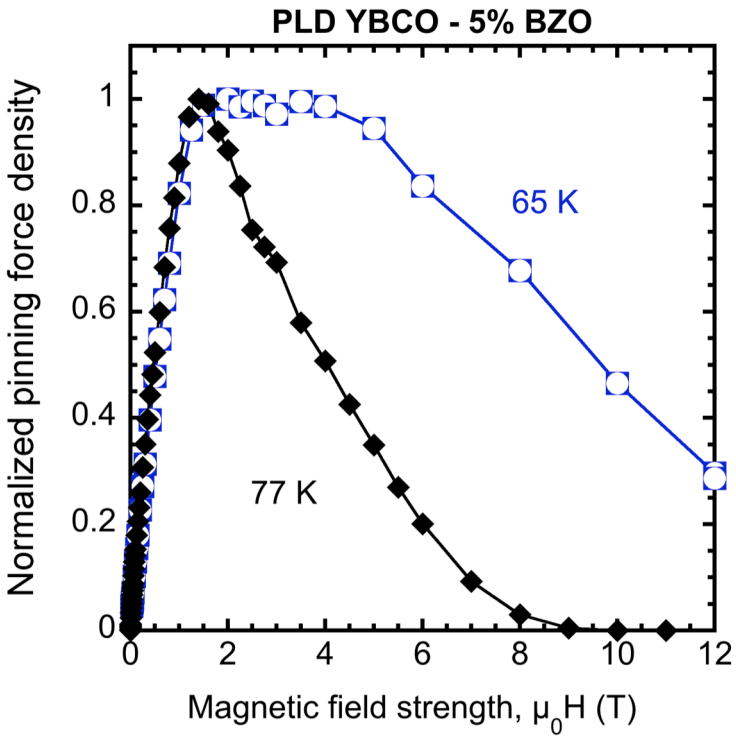

Fig. 3.8. Pinning force density dependence on the applied magnetic field at 77 K and 65 K for YBCO – 5% BZO film.

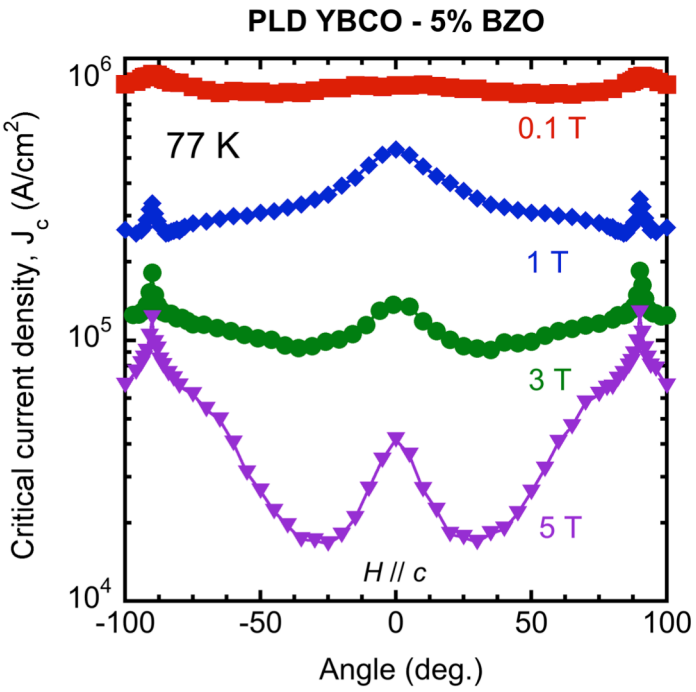

Fig. 3.9. Angular dependence of the critical current density at 77 K for YBCO – 5% BZO sample.

The critical current dependence on the angle of the applied magnetic field is shown in Figure 3.9. An evident correlated contribution (strong *c*-axis peaks at $\theta = 0°$) of the pinning centres is present with its maximum at $\mu_0 H = 1$ T. As the magnetic field increases, one can see a decrease in critical current density values at intermediate angles. At $\theta = 0°$ there is a strong peak in J_c due to the correlated pinning arising from the presence of elongated BZO columns, which act as strong pinning sites even at the highest magnetic fields. The in-field angular pinning efficiency depends on the pinning landscape - intergrowth presence, columns density, its continuity and splay. The further comparison of PLD samples will reveal the most efficient pinning given by the presence of introduced second phases.

A second PLD sample, with 7 mol.% BZO addition, has been studied by DC measurements.

The resistivity ρ dependence on the temperature, reported in Figure 3.10, exhibits a linear behaviour with a steep resistive transition. The critical temperature for this sample is $T_c = 89.5$ K. Again, it indicates homogeneous and high-quality film,

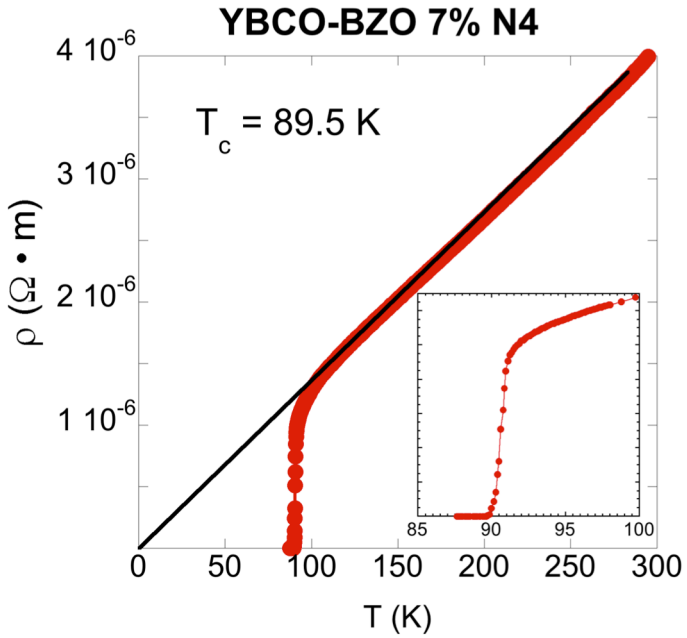

Fig. 3.10. Temperature *T* dependence of resistivity ρ measured for PLD YBCO – 7% BZO film. T_c has been evaluated as zero resistance temperature. Black straight line represents normal state resistivity. In the inset the resistive transition region has been magnified.

similar to the PLD YBCO – 5% BZO.

The field dependence of the critical current density for this sample has a similar behaviour to the one with 5% BZO doping. It has three characteristic features of BZO doped YBCO films: a plateau, a kink (more evident at 77K and 65K) and, most importantly, a power-law dependence, usually related to the presence of correlated defects (Fig. 3.11, (a)). In this sample, the coefficient α is also consistent with previous findings in PLD grown samples with $BaZrO_3$ [32], [88], [92], [97]. However, in this sample $\alpha = 0.30$ at 77 K, different from $\alpha = 0.23$ in YBCO – 5% BZO (see Fig. 3.6). It is known [28], that the reduction of α values, corresponding to a more effective in-field performance, depends on the specific defect engineering. In this case, stronger pinning is observed in PLD – 5% BZO film.

In fact, it was shown in some earlier studies that this coefficient changes with different doping percentage of BZO [96]. The coefficient usually first decreases with increasing % of BZO, then it reaches a minimum (which refers to the best pinning properties), and then it increases with further increase of % BZO. This means that there are limits to the introduction of efficient artificial defects; a higher percentage of BZO does not necessarily correspond to higher transport properties, primarily due to the detrimental problems caused by excess BZO doping [97].

(a)

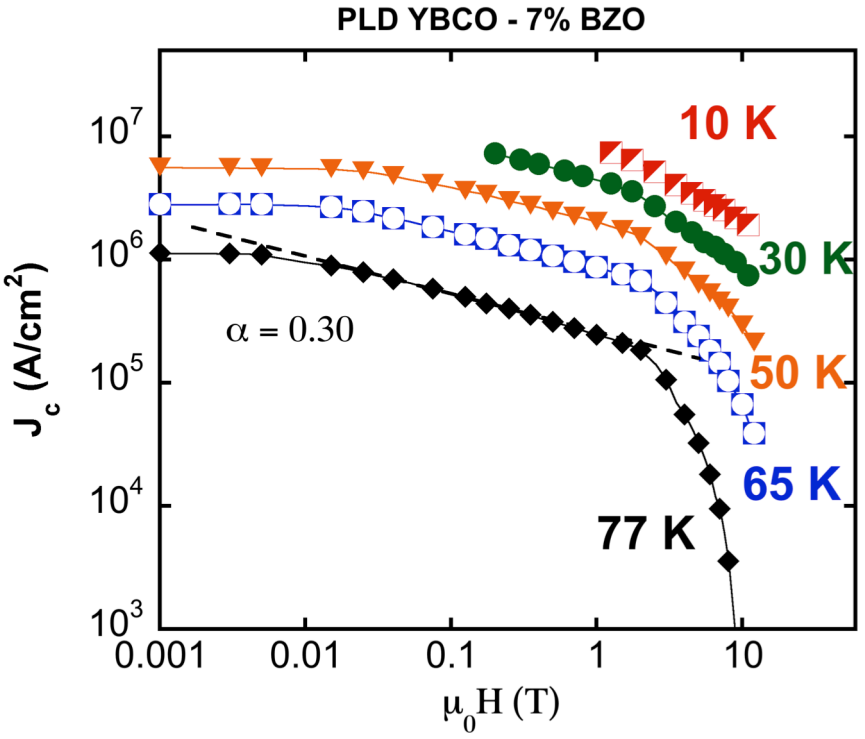

(b)

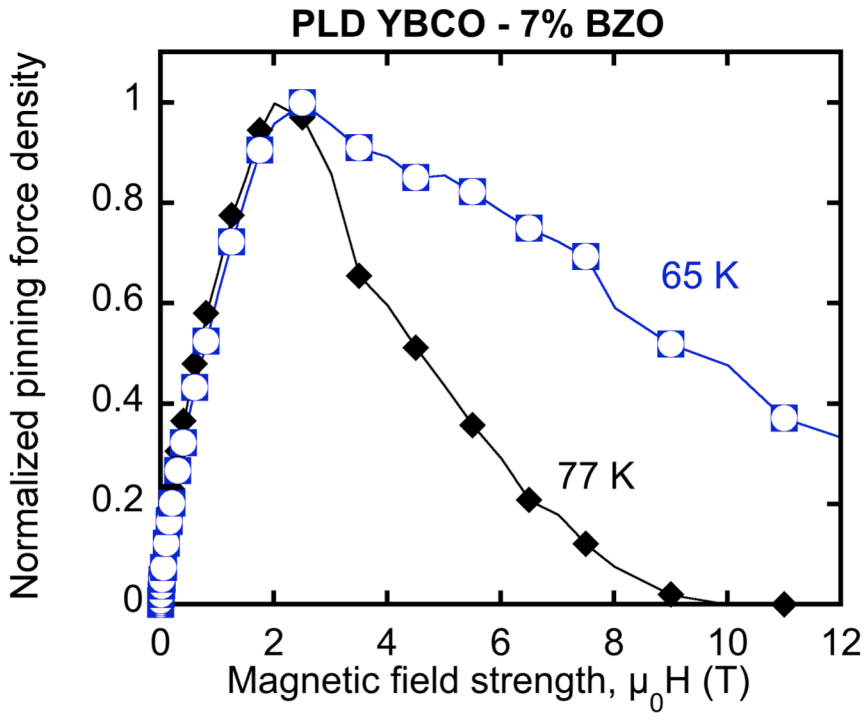

Fig. 3.11. (a) Critical current density J_c as a function of the applied magnetic field H at several temperatures. (b) Normalized pinning force density dependence on applied magnetic field at 77 K and 65 K for YBCO – 7% BZO film.

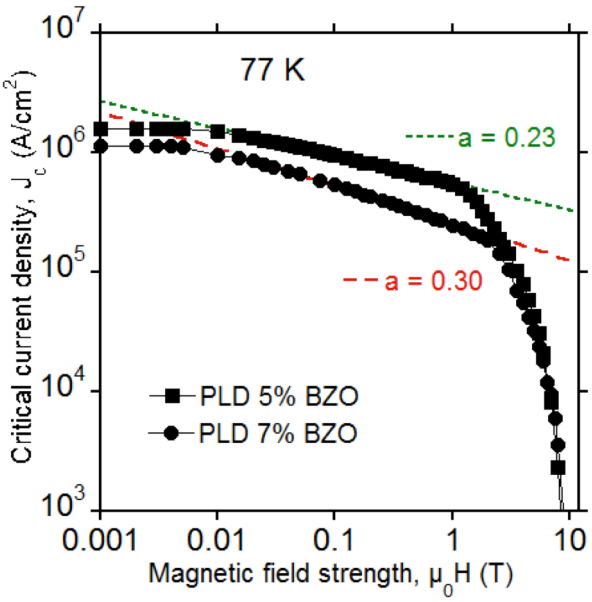

Fig. 3.12. Critical current density dependence on the applied magnetic field at 77 K for YBCO – 5% BZO (full squares) and YBCO – 7% BZO (full circles) films.

Even though the transport properties of the two doped samples are dominated by the artificial nanocolumns of BZO, and the behaviour of F_p *(H)* curves is similar (see Fig. 3.7 and 3.11 (b)), the defects have a different impact on the pinning properties at different temperatures. Although the absolute values of critical current are higher for YBCO – 5% BZO up to 2 T (as seen on Fig. 3.12), the pinning force density of 7% doped sample has a broader peak and a maximum at higher magnetic field with respect to the 5% - BZO film, 2 T and 1.4 T, respectively (Fig. 3.8 and 3.11 (b)). The irreversibility field value for this sample was H_{irr} = 9.5 T at 77 K.

The angular behaviour of J_c for this sample (Fig. 3.13) is very similar to J_c *(θ)* for

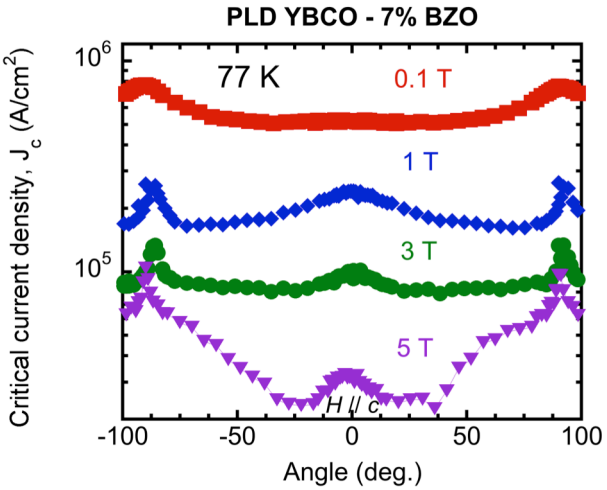

Fig. 3.13. Angular dependence of critical current density in a range of the magnetic fields at 77 K for YBCO - 7% BZO sample.

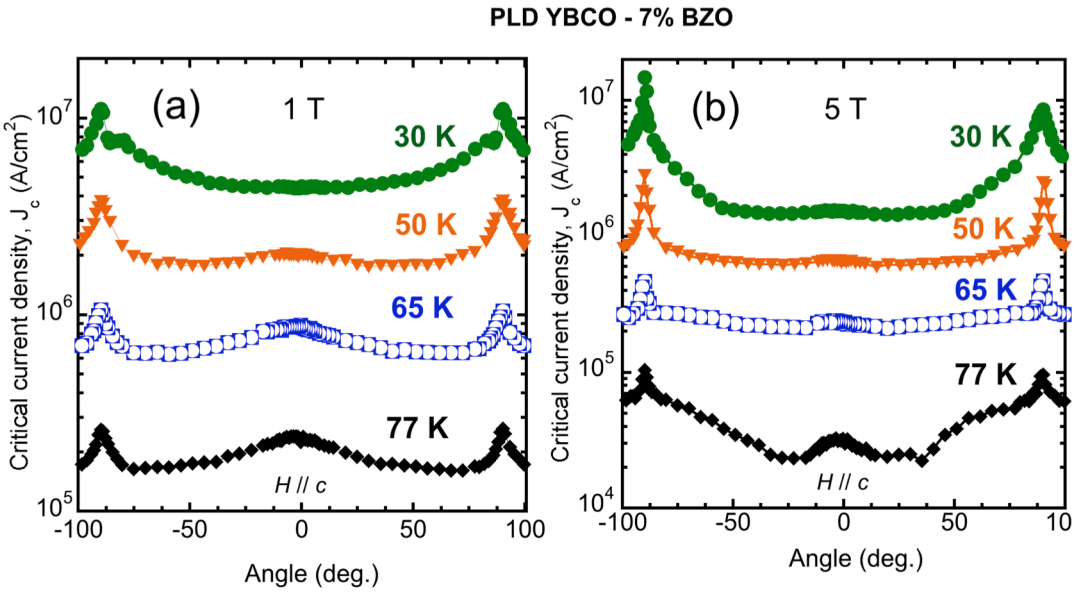

Fig. 3.14. Anisotropic behaviour of critical current density at (a) 1 T and (b) 5 T for YBCO - 7% BZO sample.

YBCO - 5% BZO sample. As the only difference, the peak at H // c-axis (related to the correlated pinning contribution).

In this sample, $J_c(\theta)$ has been also measured at different temperatures in he range of 30-77 K. (Fig. 3.14). The contribution of correlated pinning (θ = 0°) decreases with decreasing the temperature and disappears at 30 K, suggesting that the effectiveness of extended defects (BZO nanocolumns) is progressively reduced on lowering the temperature and that at low temperatures the dominant pinning contribution arises from isotropic pinning centers.

3.3.2 PLD YBCO film with $Ba_2Y(Nb/Ta)O_6$ nano-columns

Since $BaZrO_3$ nano-inclusions have proved to be effective APCs, several nano-scale pinning additions as the double perovskite-like Ba_2YNbO_6 (BYNO) or Ba_2YTaO_6 (BYTO) have been studied. One of the most intriguing features of such phases is the easy development of a complex landscape of defects by mixed doping. A proper combination of columnar, planar and nanoparticle defects in BYTO + BYNO doped-YBCO films have been reported as a very effective pinning source with a high potential for pinning improvement. A deeper investigation of the material system YBCO / BYNTO is needed to provide a better understanding of its complex

pinning landscape and the resulting effects on J_c *(H,T,θ)*. For this reason, I extended my investigations to critical current properties in YBCO film with Ba_2YTaO_6 + Ba_2YNbO_6 ($Ba_2Y(Nb/Ta)O_6$, BYNTO) nano-inclusions.

The electrical resistivity ρ as a function of temperature is plotted on Figure 3.15. The resistivity transition is not as steep as in BZO doped samples, with a slightly lower critical temperature value T_c = 88.5 K. As mentioned in Chapter 2, T_c might decrease as repetition rate increasing in the PLD deposition process. Relatively high repetition rate used in PLD growth process of this BYNTO sample could have caused a slight reduction in T_c for this particular sample. Nevertheless, the sample is indicated as homogeneous and high-quality film. For the PLD growth repetition rate of 10 Hz used for this sample, T_c value is actually higher than that reported recently in another study ($T_c \sim 85$ K) [67], where YBCO with BYNTO were grown with the same (10 Hz) repetition rate.

Figure 3.16 (a) presents the field dependences of the critical current density in the temperature range 10 K – 77 K for the YBCO/BYNTO film. Whereas the J_c behaviour is similar for both types of doped samples, the YBCO/BYNTO film has a better J_c retention as magnetic field increases not only in comparison with BZO films from this study, but also with results reported previously for other BYNTO doped films [67]. In fact, the YBCO/BYNTO sample shows an extended power-law-like region up to around 5 T (inset in Fig. 3.16 (a)) with coefficient $\alpha = 0.28$, whereas a kink with a pronounced J_c drop is observed in YBCO/BZO films at about 1 T.

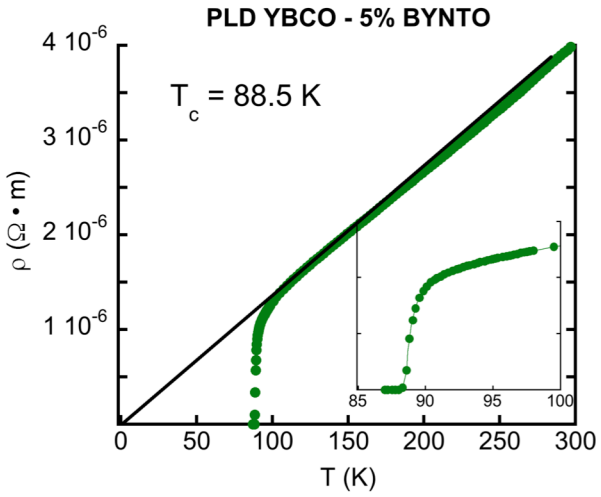

Fig. 3.15. Temperature T dependence of the resistivity ρ measured for the PLD YBCO – 5% BYNTO film. T_c has been evaluated as the zero resistance temperature. The black straight line represents the normal state resistivity. In the inset the resistive transition region has been magnified.

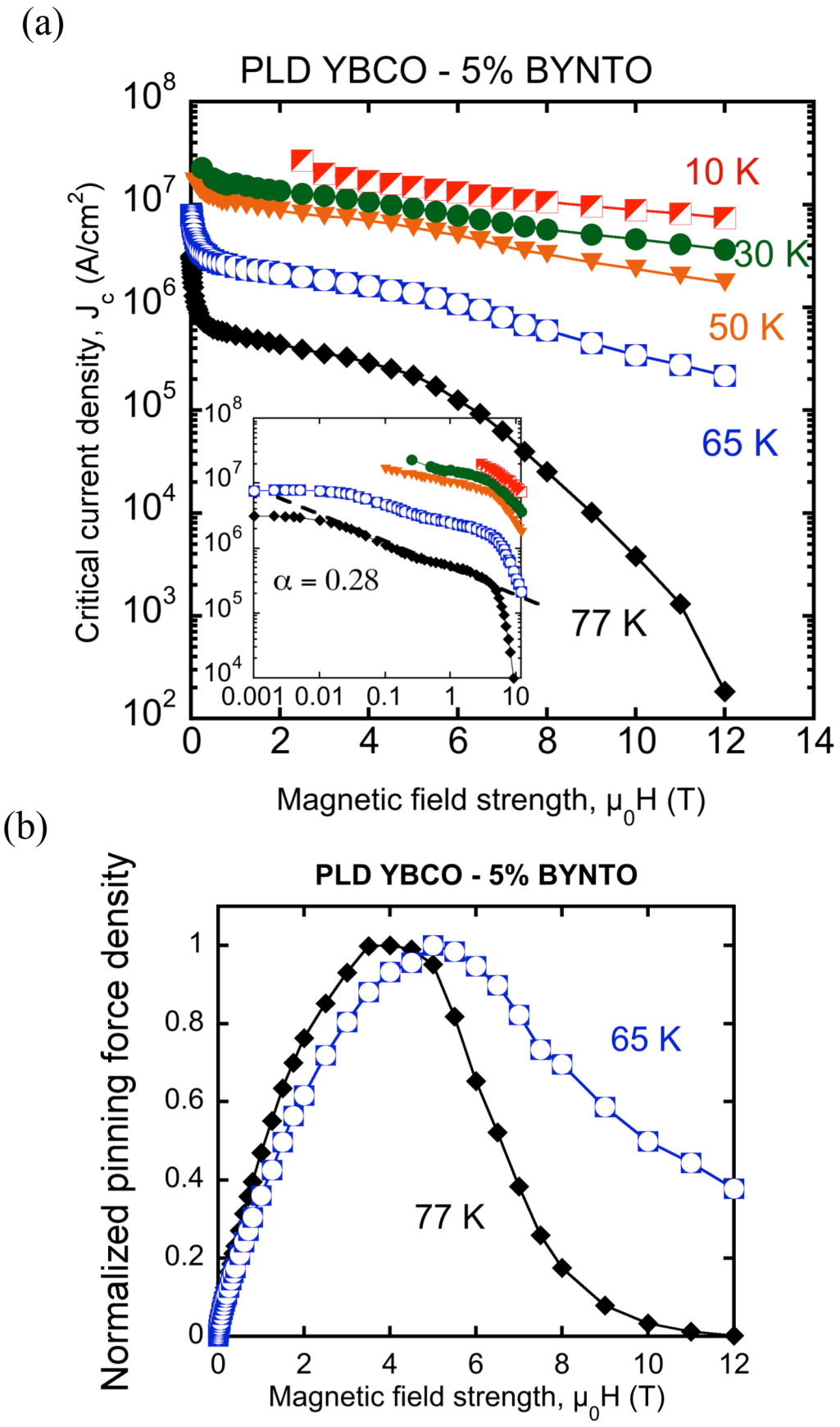

Fig. 3.16. (a) Critical current density as a function of the applied magnetic field at several temperatures; (b) Normalized pinning force density as a function of applied magnetic field at 77 K and 65 K for the YBCO – 5% BYNTO film. The inset in (a) is a log-log plot of $J_c(H)$.

Field normalized pinning force density is presented in Figure 3.16 (b). The $F_p\,(H)$ behaviour is significantly improved in comparison with the BZO doped samples: the peak corresponding to the maximum value is much broader. The maximum value for the YBCO/BYNTO sample is significantly increased - $F_p{}^{max} = 11.5$ GN/m^3. The irreversibility field value for this sample was $\mu_0 H_{irr} = 11.1$ T at 77 K.

The anisotropy of the critical current density $J_c\,(\theta)$ at different magnetic fields and 77 K (Fig. 3.17) and at fixed magnetic field (1 T and 5 T) with variation of the temperature (Fig. 3.18) shows a typical maximum at 90° due to the electronic mass anisotropy of YBCO structure [62] and another strong peak at 0° due to the strong *c*-axis correlated pinning by introduced BYNTO nano-columns [98]. On a contrary with the YBCO/BZO sample (Fig. 3.14), correlated pinning in YBCO/BYNTO sample is very strong even at lower temperatures (Fig. 3.18). The combination of *c*-axis aligned BYNTO continuous columns and Y_2O_3 nanoparticles provides a strong pinning source for vortices at high magnetic fields, which results in a J_c improvement in a wider angular range in comparison with YBCO/BZO.

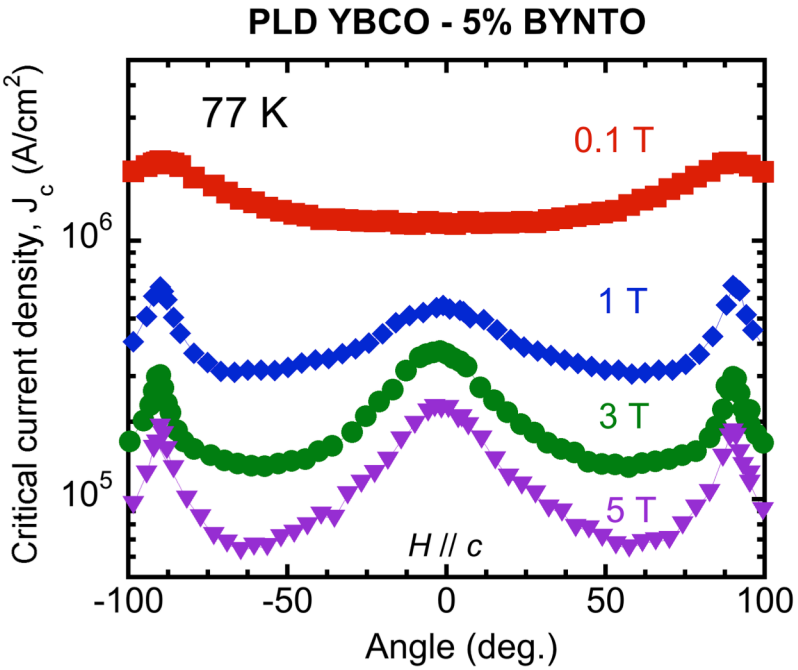

Fig. 3.17. Angular dependence of critical current density in a range of the magnetic fields at 77 K for YBCO - 5% BYNTO sample.

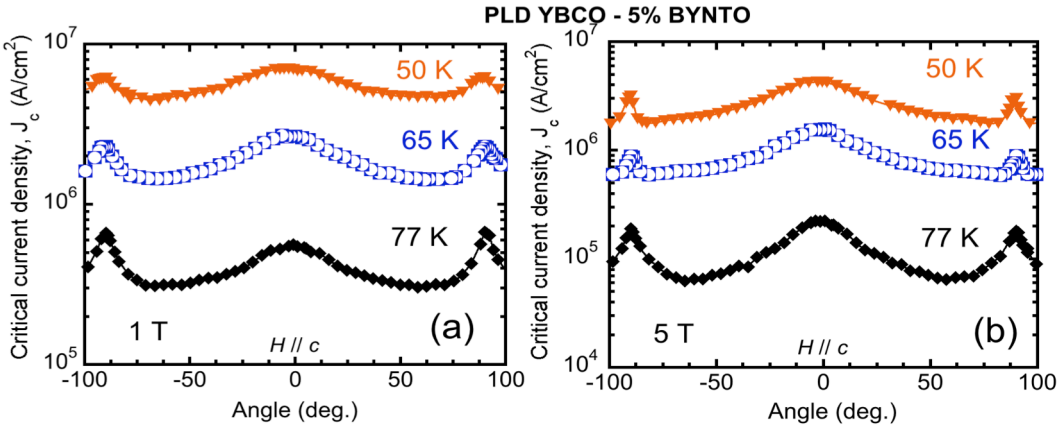

Fig. 3.18. Anisotropic behaviour of critical current density at (a) 1 T and (b) 5 T for YBCO - 5% BYNTO sample.

3.4 Transport properties of MOD films

This section presents the transport properties of YBCO nanocomposite films with and without $BaZrO_3$ inclusions as artificial pinning centres grown on $SrTiO_3$ single crystal substrate by Metal Organic Decomposition (MOD) technique. All measurements of J_c dependence on the applied magnetic field were performed at

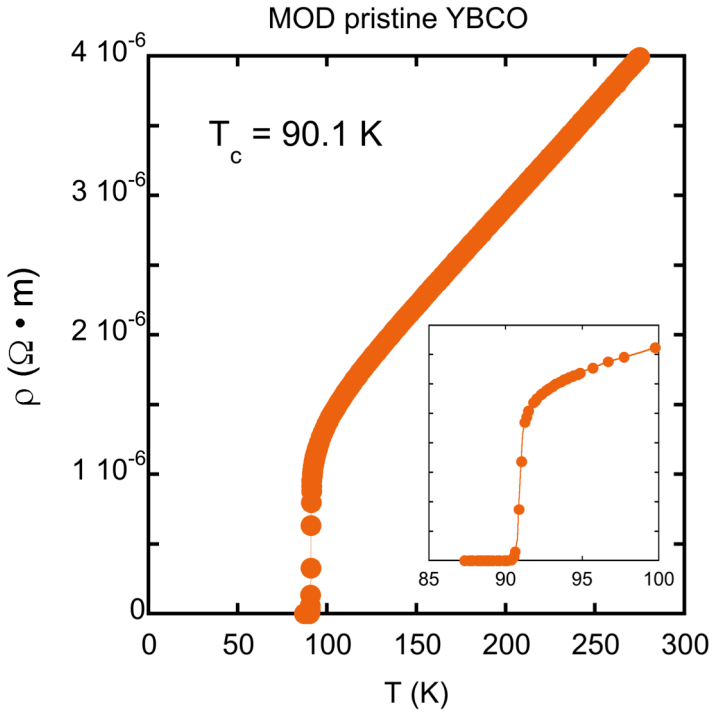

Fig. 3.19. Temperature T dependence of the resistivity ρ measured for the pristine MOD YBCO film. T_c has been evaluated as the zero resistance temperature. In the inset the resistive transition region has been magnified.

fixed field orientation H // *c*-axis of the film (θ = 0º). All the angular dependences of J_c were obtained at fixed fields and angles varied from - 100º to + 100º degrees.

3.4.1 Pristine MOD YBCO film

A pristine YBCO film was grown by MOD technique. It exhibits a good superconducting transition and the high critical temperature T_c = 90.1 K, typical for

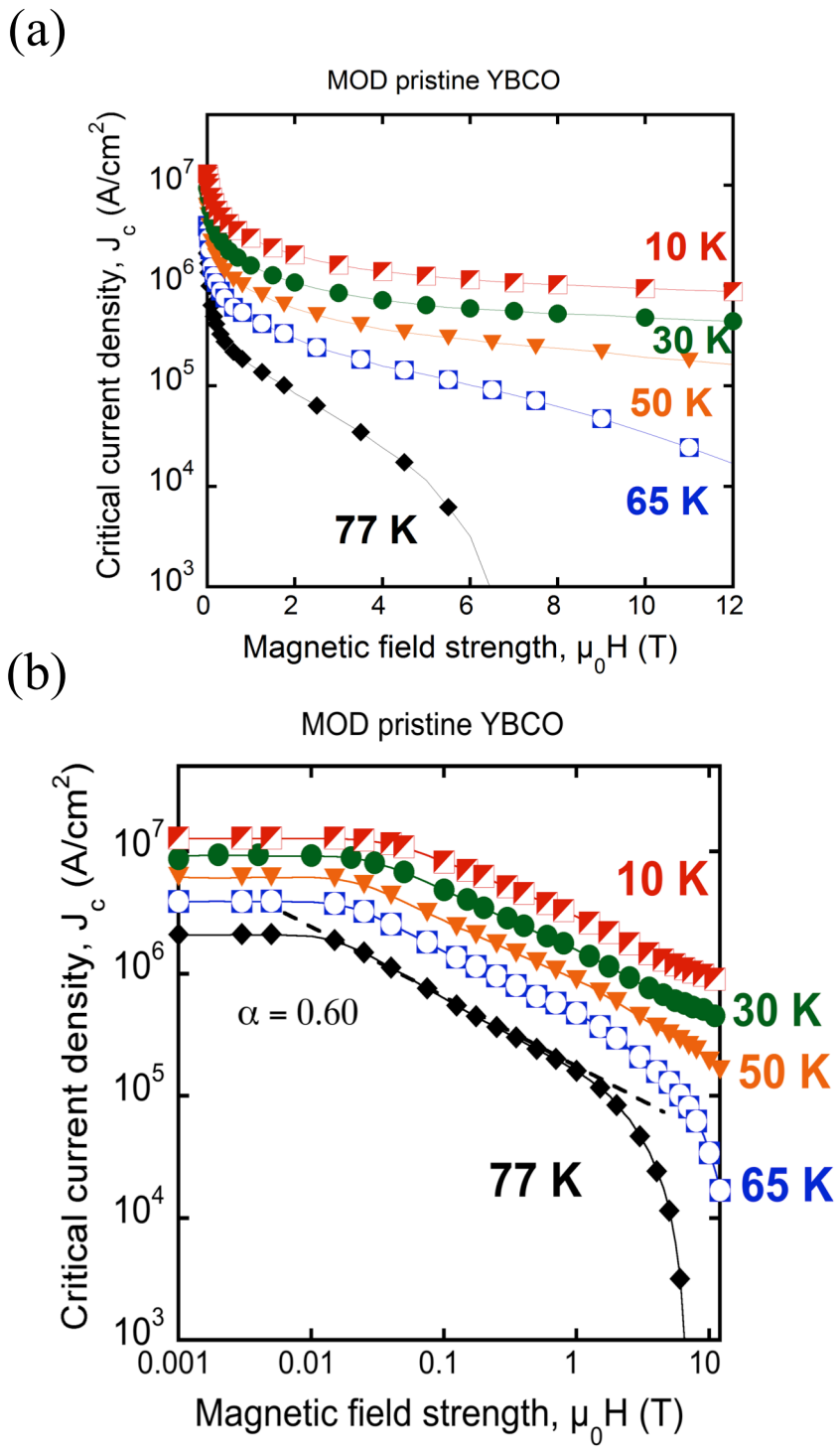

Fig. 3.20. Critical current density as a function of the applied magnetic field at veral temperatures for the pristine MOD YBCO film. (b) A log-log plot of $J_c(H)$.

non-doped YBCO films [47], [83] (Fig. 3.19).

This sample shows the typical behaviour of MOD-grown pristine YBCO films, consistently with previous studies [47], [83], [99], with a quite good J_c retention in field even in comparison with some previously reported similar YBCO samples [47] (Fig. 3.20). $J_c(H)$ in this MOD sample shows three regions – a plateau, a kink (more evident at 77K), and a power-law dependence $J_c \sim H^{-\alpha}$, usually related to the presence of correlated defects, which has a coefficient α close to the theoretical value $\alpha = 0.5$. This finding hints to the planar nature of correlated defects in this sample. At 77 K $\alpha = 0.6$, but approaches $\alpha = 0.5$ as temperature goes down.

As it can be seen on Figure 3.21, the pinning force improves with decreasing the temperature: the maximum value (F_p^{max} = 1.78 GN/m^3 at 77 K) peak is much broader at 65 K. Nevertheless, the H_{max} (marked as dashed red line) in this sample is temperature dependent: $\mu_0 H_{max}$ = 1.75 T at 77 K and $\mu_0 H_{max}$ = 4.5 T at 65 K. The irreversibility field value for this sample was $\mu_0 H_{irr}$ = 7 T at 77 K.

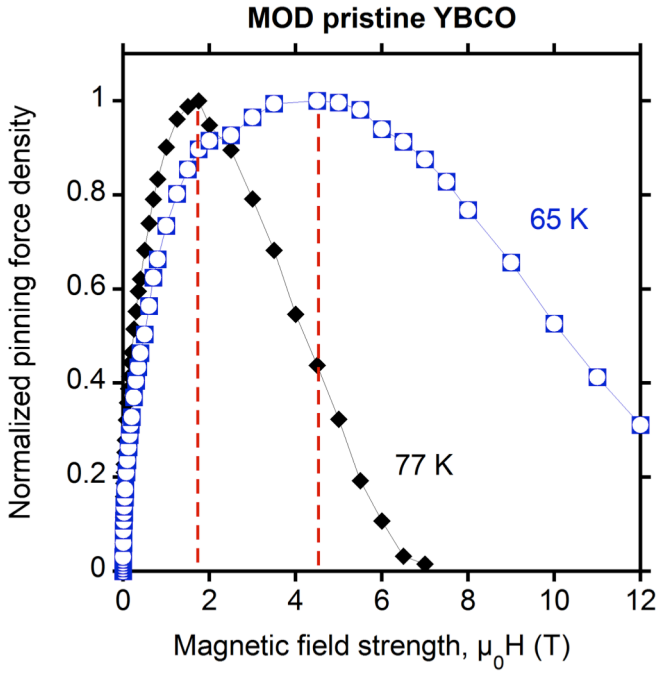

Fig. 3.21. Pinning force density dependence on the applied magnetic field at 77 K and 65 K for the pristine YBCO film.

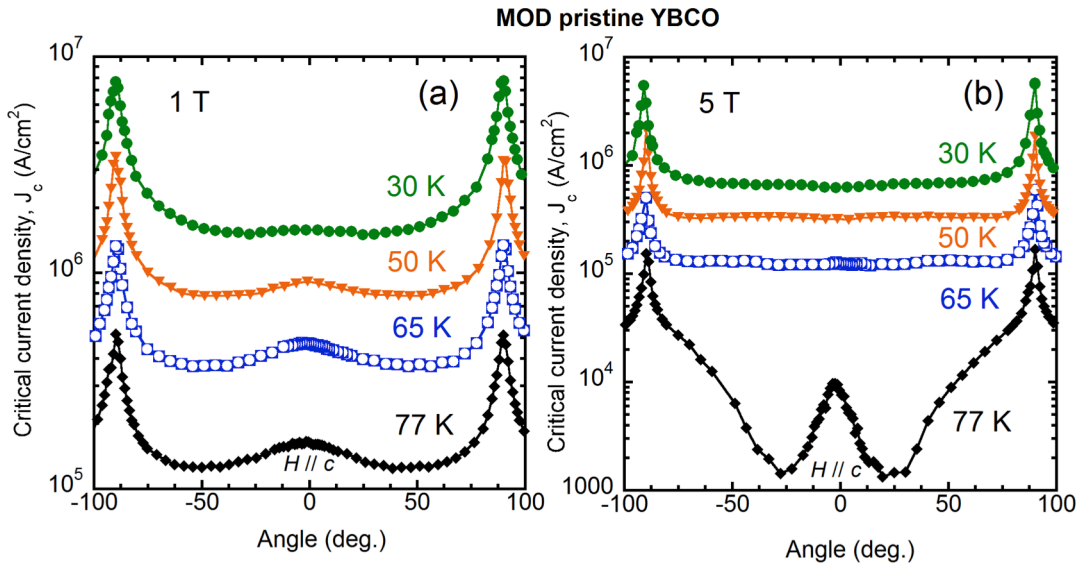

Fig. 3.22. Anisotropic behaviour of the critical current density at (a) 1 T and (b) 5 T for the MOD pristine YBCO sample.

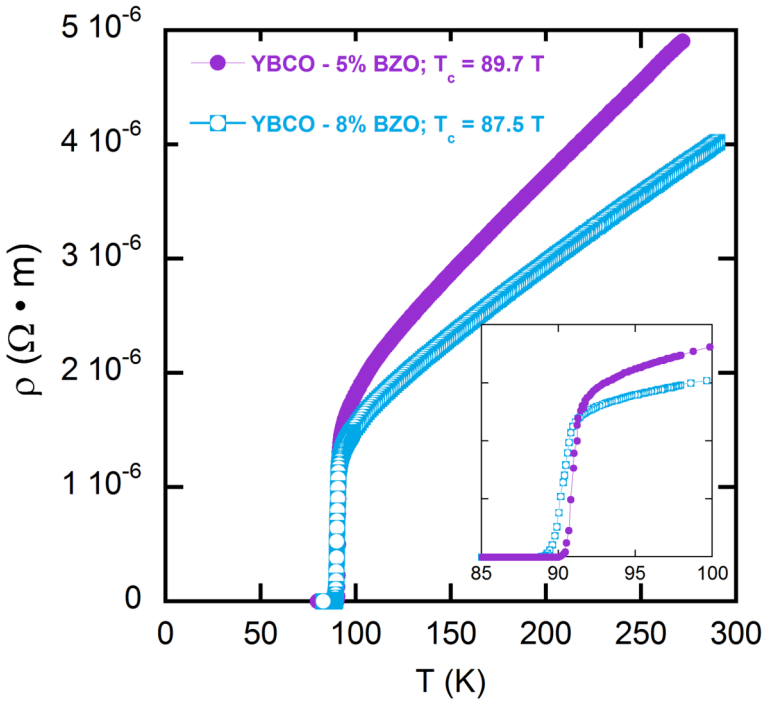

Fig. 3.23. Temperature dependence T of resistivity ρ measured for MOD 5% and 8% of YBCO films. T_c has been evaluated as zero resistance temperature. In the inset the resistive transition region has been magnified.

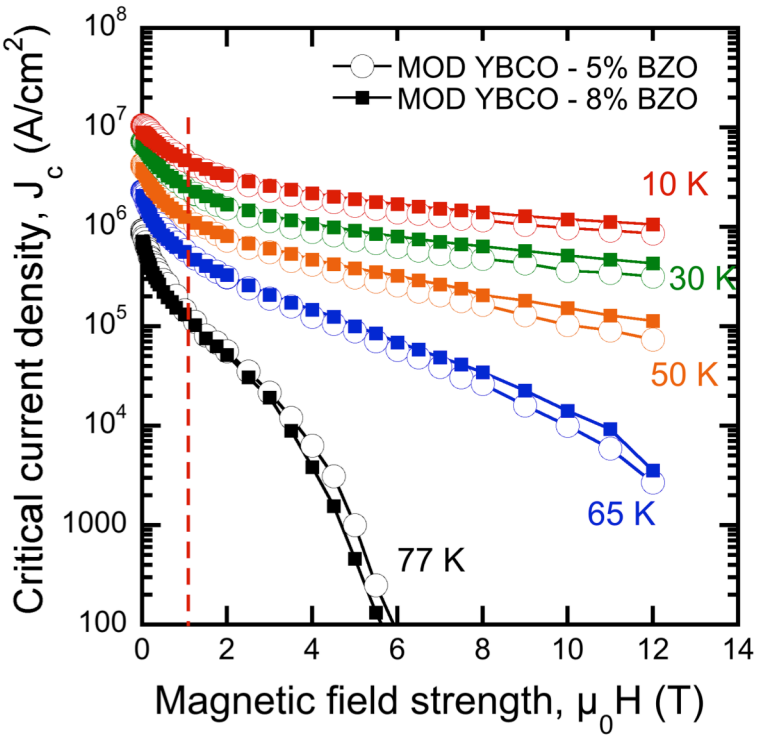

Fig. 3.24. Critical current density as a function of the applied magnetic field at several temperatures for MOD YBCO – 5% BZO (open circles) and YBCO – 8% BZO (full squares) films.

The anisotropy of the critical current density $J_c(\theta)$ at 1 T and 5 T (Fig. 3.22) shows the usual maximum at θ =90° due to the intrinsic pinning, arising from the layered structure of YBCO material. However, a second maximum exists at θ = 0°, clearly originating from some strong *c*-axis correlated pinning. This is consistent with the behaviour reported at relatively high temperatures (T > 50K) [69] in MOD films, with strong vortex pinning at magnetic field H //*c*-axis [82], [89], [90], [93]. This feature will be further discussed in Chapter 5.

3.4.2 MOD YBCO films with $BaZrO_3$ nano-inclusions

Two BZO-doped films were grown by MOD. Figure 3.23 reports the temperature dependence of resistivity ρ in the MOD YBCO – 5% BZO and YBCO – 8% BZO samples. The curves exhibit a linear dependence as a function of the temperature. Despite the fact of higher resistivity values prior to the transition, the transition of the sample with 5% BZO is steeper than that in YBCO – 8% BZO with a higher critical temperature T_c = 89.7 K in YBCO – 5% BZO as opposed to T_c = 87.5 K in YBCO –

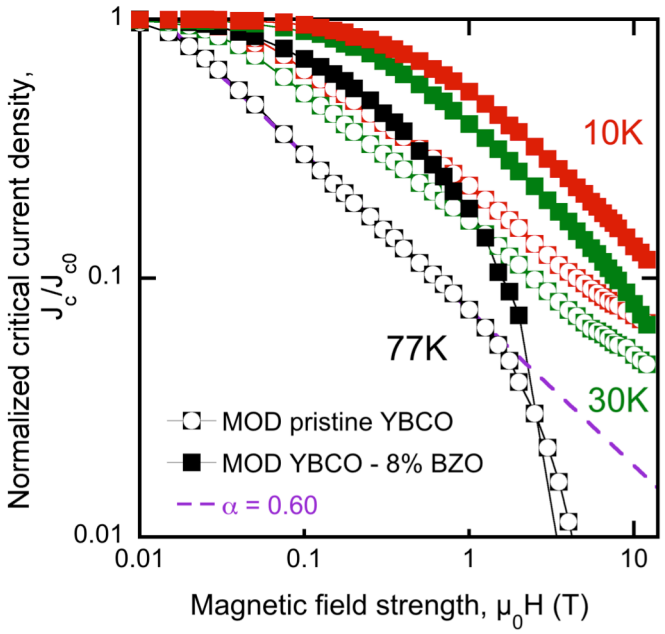

Fig. 3.25. Log-log plot of the normalized critical current density as a function of the magnetic field at several temperatures for the pristine MOD (open circles) and the YBCO – 8% BZO (full squares) samples.

8% BZO. In fact, the sample at 5% BZO exhibits a critical temperature value close to the pristine sample. These results indicate homogeneous and high-quality film.

Both samples show similar results for the critical current density as a function of the magnetic field (Fig. 3.24). After about 1 T (marked as a dashed line on Fig. 3.24) and at temperatures below 77 K, the YBCO - 8% BZO sample performs slightly, but consistently better than the sample at 5 % BZO. This is likely to be due to a better pinning efficiency of nanoparticles with higher density in the sample at 8% of doping.

The log-log plot of normalized critical current density as a function of magnetic field at several temperatures for the pristine MOD and the 8% BZO doped sample is presented in Figure 3.25. The comparison at 77 K shows that unlike the pristine MOD film, the BZO doped sample has non-power-law behaviour (this is also true in the YBCO – 5% BZO film). This feature has been observed in other chemically derived films [35], [83], [100], where defects are distributed homogeneously within the YBCO matrix and have a form of nanoparticles, as opposed to nano-columns in

PLD derived films, thus indicating the different pinning mechanism in MOD and PLD derived YBCO films.

The pinning force density (Fig. 3. 26) has a similar field dependence in both BZO doped samples; however at lower temperatures, the sample with 8% BZO performs slightly better at higher magnetic fields ($\mu_0 H > 3$ T).

Interestingly, neither of two doped samples show a sign of correlated pinning at field parallel to the *c*-axis orientation (Fig. 3.27): no peak in $J_c(\theta)$ at $\theta = 0°$ is detected. It is a clear sign the prevalence of random pinning due to 3D-type defects that are randomly incorporated inside the YBCO matrix. This was previously observed in other studies of YBCO doped films with nanoparticles [40], [83], [91].

A comparison between the BZO doped samples (Fig. 3.28) shows that the angular dependence $J_c(\theta)$ is quite similar in both samples, apart from the curves at 77 K: YBCO – 8% BZO has a lower J_c value in the area around $\theta = 0°$, which was earlier reflected in $J_c(H)$ dependence in Figure 3.24. Besides that, the 8% BZO doped sample has slightly better performance in a wide angular range.

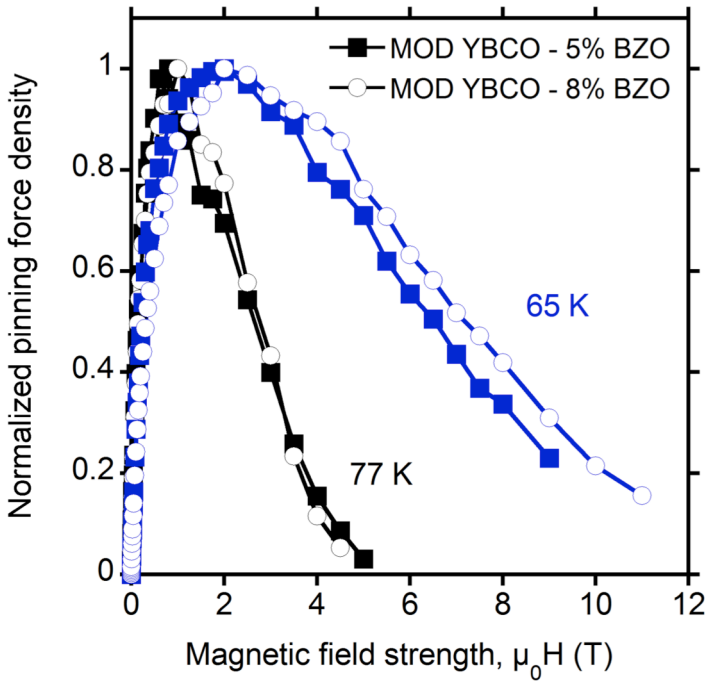

Fig. 3.26. Pinning force density dependence on applied magnetic field at 77 K and 65 K for YBCO film with 5% BZO (full squares) and 8% BZO (open circles).

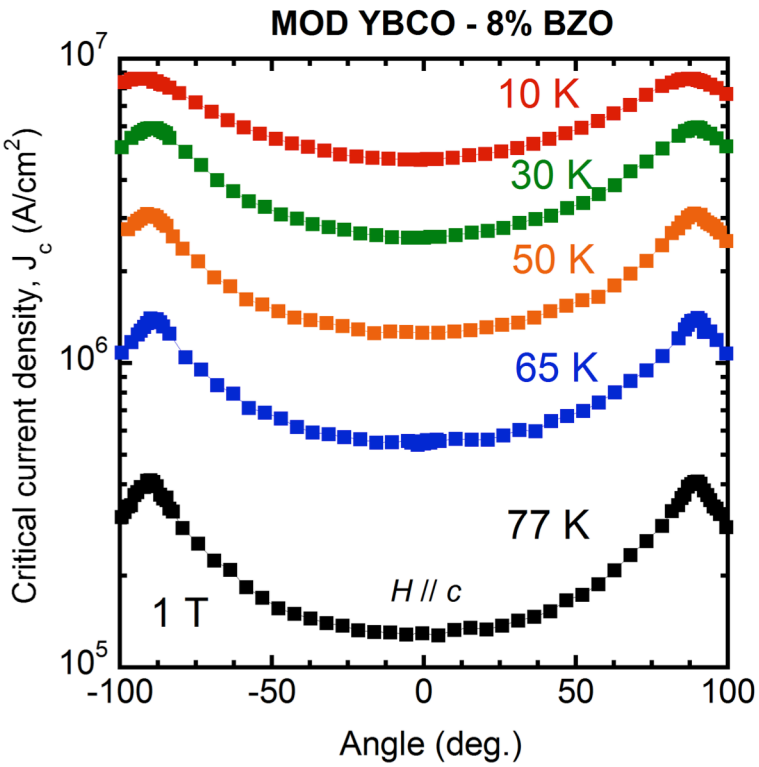

Fig. 3.27. Anisotropic behaviour of critical current density in YBCO – 8% BZO at 1 T.

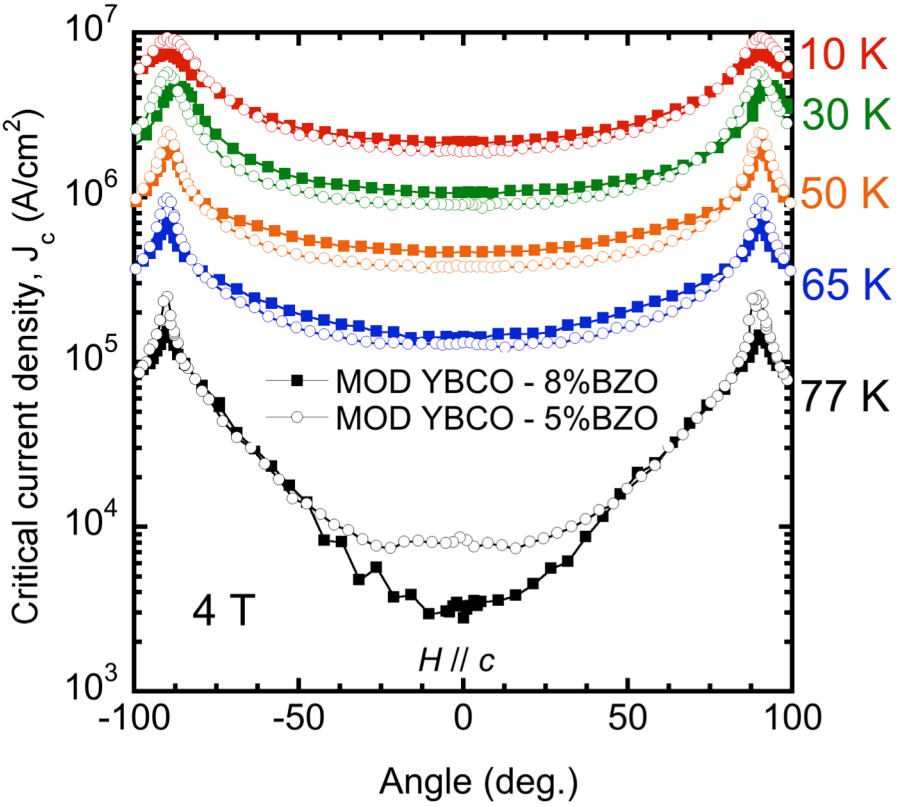

Fig. 3.28. Anisotropic behaviour of critical current density in YBCO – 5% BZO (open circles) and 8% BZO (full squares) MOD samples.

3.5 Summary

In this Chapter, I reported on the J_c (T, H, θ) for all the samples investigated, PLD and MOD.

The resistive transitions indicate homogeneous and high-quality films in all cases.

J_c in all the PLD grown samples exhibits three characteristic features of correlated APCs: a plateau, a kink (more evident at 77K and 65K) and, most importantly, a power-law dependence $J_c \propto H^{-\alpha}$, which in this case is due to the presence of nano-columns, as observed by TEM in Chapter 2. All three samples demonstrate the *c*-axis correlated pinning due to the introduced second phases, with the strongest performance in YBCO with BYNTO nano-columns. Different from the YBCO/BZO samples, the correlated pinning behaviour in YBCO/BYNTO sample is weakly dependent on temperature.

Interestingly, the critical current density in the MOD pristine sample also demonstrates three regions – a plateau, a kink (more evident at 77K), and a power-law dependence $J_c \propto H^{-\alpha,}$ thus showing evidence for the presence of correlated defects. In this case, the coefficient $\alpha \approx 0.6$ attains a value close to the theoretical value for 2D defects, and then it hints at the planar nature of correlated defects in this sample.

The comparison at 77 K shows that, unlike in pristine MOD film, BZO doped samples have non-power-law behaviour. Together with the absence of signatures for correlated pinning at field parallel to *c*-axis orientation in J_c *(θ),* it is an evidence for random pinning only. The pinning is then due to 3D-type defects (nanoparticles) that are randomly incorporated inside the YBCO matrix.

Further discussion on DC current transport properties will be given in Chapter 5.

Chapter 4

Microwave properties

It was shown that microwave measurements allow accessing the flux-flow resistivity at subcritical currents as well as other flux motion parameters. By exploiting the physical processes responsible for the dissipation in superconductors, a microwave measurement can act as a reliable, non-destructive test for HTS materials. This test is a valuable tool in the path toward optimization of the superconductors.

I will first describe the microwave measurement technique. I will then analyze the data of the microwave complex resistivity in presence of the external magnetic field taken in several YBCO films. Based on the field dependence of the pinning parameters derived from the microwave measurements, such as the pinning parameter r and the pinning constant k_p, I will discuss the vortex pinning regimes.

4.1 Motivation

This work shows that by exploiting the physical processes responsible for the dissipation in superconductors, the microwave measurements can act as a reliable, non-destructive material test for High Temperature Superconductors (HTS). This technique is a valuable tool in the path toward optimization of the superconductors, for both samples on single crystal substrates (laboratory scale), and for coated conductors.

Microwave measurements are a useful technique for in-depth study of pinning induced by nano-inclusions, and of the balance between material degradation and pinning increase, especially when compared with the standard DC transport measurements.

With the DC technique (resistivity, critical current density, magnetization), one probes the long-range vortex motion (in the nonlinear regime) when the leading mechanism is the complete depinning of the flux lines and their drag along relatively large distances, so that the depth of the pinning wells dictates the dynamics. By contrast, short-range oscillations at microwave frequencies probe the steepness of the potential wells as a first approximation. Thus, a microwave investigation can shed light on the steepness, as well as the depth, of the pinning wells and the microwave response allows to extract a wealth of information on the vortex dynamics [101]-[103]. Thus, microwave measurement method is a perspective complementary technique to the DC electric transport measurements for the vortex pinning investigation and efficient characterisation of the in-field performance and the role of the structural defects in the superconducting films.

4.2 Microwave measurement technique

The dielectric resonator technique at 47.7 GHz allows to measure contactless and with high sensitivity the microwave electrodynamic response of the films [104]. A single-mode, high-frequency dielectric resonator has been used for the measurement of the surface impedance on the films of typical dimensions 10 mm×10 mm. A cylindrical geometry and TE_{011} resonant mode are chosen to obtain the high quality factor Q. Moreover, being the TE_{011} one of the lowest frequency modes, it is usually well separated from other modes. The sketch of the resonator is reported in Fig. 4.1. The top and bottom plates are in contact with the sapphire rod. Sapphire, being one of the few commercially available dielectrics, is widely used not only because it is characterized by high permittivity, but also due to its extremely low dielectric losses at microwaves.

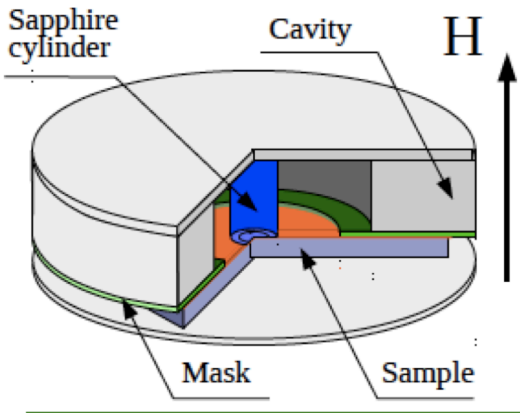

Fig. 4.1. The sketch of the dielectric resonator

Resonant systems are characterized by two parameters: the resonant frequency ν_0 at which the stable electromagnetic field configuration exists and the quality factor Q [105]. The Q-factor takes into account the losses in the resonant system with respect to the stored energy. Larger Q-factor implies that less power dissipated in the elements of the resonator like dielectrics and conductors. The resonant frequency ν_0 strongly depends on the geometry of the resonator and on the material properties. A typical frequency sweep is presented in Figure 4.2. In general, it can be accurately determined only as a variation with respect to external parameters. The variation of the parameters is made with respect to some base value (value at fixed temperature, field etc.). As a consequence, it will be described shortly that with a resonant technique one can access the measurement of the absolute value of the surface resistance and of the variations of the surface reactance.

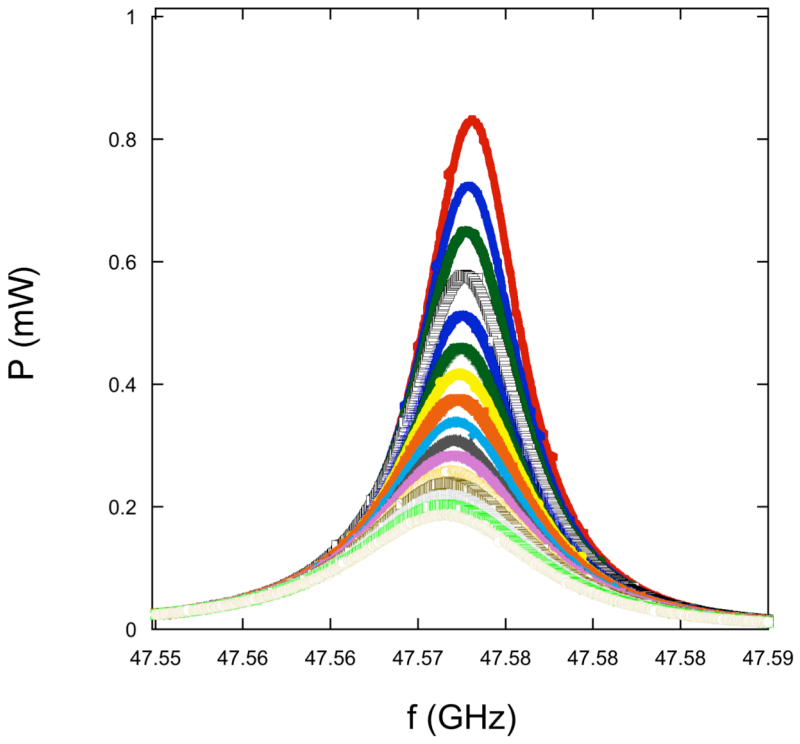

Fig. 4.2. A frequency sweep for a YBCO film.

In the microwave frequency range, the relevant experimental quantity is the surface impedance, which is defined through the ratio of the components of the impinging electric and magnetic fields on the material surface, by means of: $Z_s = E_\parallel / H_\parallel$, where the electric and magnetic field components are orthogonal to each other and parallel to the vacuum/superconductor boundary.

In a superconductor, Z_s can be written in terms of the complex conductivity σ [106]:

$$Z_s = R + iX = \sqrt{\frac{i\omega\mu_0}{\sigma}} \qquad (4.1)$$

where σ is the material complex conductivity, R and X are the surface resistance (the real part) and the surface reactance (the imaginary part), respectively. At zero external magnetic field, R represents the losses of the microwave power, and is due to the presence of quasi-particles ("non-superconducting charge carriers"). X represents the screening effects and it can be used for the determination of the London penetration depth, related to the superconducting order parameter. In presence of a static magnetic field, type II superconductors are driven in the mixed state, where the magnetic field partially penetrates in the superconductor volume in shape of fluxons. In applied magnetic field it is easier to measure variation of the surface impedance $\Delta Z = \Delta R + i\Delta X$: since thermal gradients affect repeatability, slow temperature variations are required. Moreover, the temperature variations of the microwave line response impose to detune the cavity quite often. Since one cannot exactly reposition the piston, little jumps in the cavity resonant frequency are produced every time the cavity is detuned and retuned. By measuring magnetic field-induced variations ΔZ (H) these problems disappear or reduce. More precisely, background is exactly cancelled while line calibration can be performed only once, since the system is kept at fixed temperature.

In this case, ΔR is mainly determined by the so-called flux flow resistivity, related to the quasi-particles excitations in the vortex cores, whereas ΔX is related to the effect

of the vortex pinning, which is important for the reduction of the vortex-motion-induced dissipation. These quantities can be obtained using the main resonator characteristics by means of the relations [81], [103], [107 -110]:

$$\Delta R(H) = G\left[\frac{1}{Q(H)} - \frac{1}{Q(0)}\right] \tag{4.2}$$

$$\Delta X(H) = -2G\left[\frac{\nu_0(H)-\nu_0(0)}{\nu_0(0)}\right], \tag{4.3}$$

where Q is the quality factor, ν_0 is the resonant frequency of the resonator mode and G is the calculated geometrical factor.

In thin films the probing electromagnetic field does not vanish in the volume, and a leakage arises. Thus, the substrate where the film is grown gives a substantial contribution to the measured surface impedance and the problem of the interpretation of the data in surface impedance measurements arises. The use of approximate expressions finds, in general, a set of ranges of frequency and film thickness where the error is below 1% with respect to the use of the full expression. This holds true also in the potentially critical case of superconducting films, where the conductivity is mainly imaginary. However, the identification of such ranges can be nontrivial, in particular in high-permittivity substrates. In case of YBCO films on STO substrate, the so-called thin film approximation could be applied: $Z_s^{(i)} \backsimeq Z_f = R_f + iX_f = \frac{1}{\widetilde{\rho_s}\ t_s}$, where $\tilde{\rho} = 1/\tilde{\sigma_s}$ is the frequency dependent complex resistivity of the film and t_s is the film thickness.

From the directly measured Q and ν_0 parameters and using the thin film approximation [111], [112], one obtains the vortex complex resistivity $\Delta\rho(H) = \Delta\rho_1(\mathrm{H}) + \mathrm{i}\Delta\rho_2(\mathrm{H})$ at a fixed temperature as following relation:

$$\Delta Z(H) = \frac{\Delta\rho_1 + i\Delta\rho_2}{t} = \frac{\rho_{v1}(H) + i\rho_{v2}(H)}{t}, \tag{4.4}$$

where $\rho_{v1} + i\rho_{v2}$ is the vortex motion resistivity and t is the thickness of the film.

The strength of the vortex pinning can be quantified through the relevant pinning parameter r [81], [109], [113], [114], indicating the balance between reactive and resistive response:

$$r(H,T) = \frac{\rho_{v2}(H)}{\rho_{v1}(H)} = \frac{\Delta X(H)}{\Delta R(H)} \tag{4.5}$$

According to the Gittleman and Rosenblum (GR) model (see Chapter 1), the dynamic equation for the balance of forces acting on a vortex is $\eta\vec{v} + k_p\vec{x} = \vec{J}\times\overrightarrow{\Phi_0}$, where $\vec{v}$ and $\vec{x}$ are the vortex velocity and displacement, respectively, η is the vortex viscosity and k_p is the pinning constant (Labusch parameter). In the London limit, $B = \mu_0 H$, and the resulting complex resistivity is [17], [115]:

$$\rho_{v1} + i\rho_{v2} = \frac{\Phi_0 B}{\eta}\frac{1}{1 - i\frac{kp}{2\pi\eta\nu}} \tag{4.6}$$

Within this model, $r = k_p/2\pi\eta\nu$, see Eq.s (4.5) and (4.6), and k_p can be easily obtained. It is stressed that this is a single-vortex model, where the physical meaning of k_p is the single vortex spring constant coming from the interaction with one or few pinning sites. The measurement on a large number of fluxons obviously yields an average value.

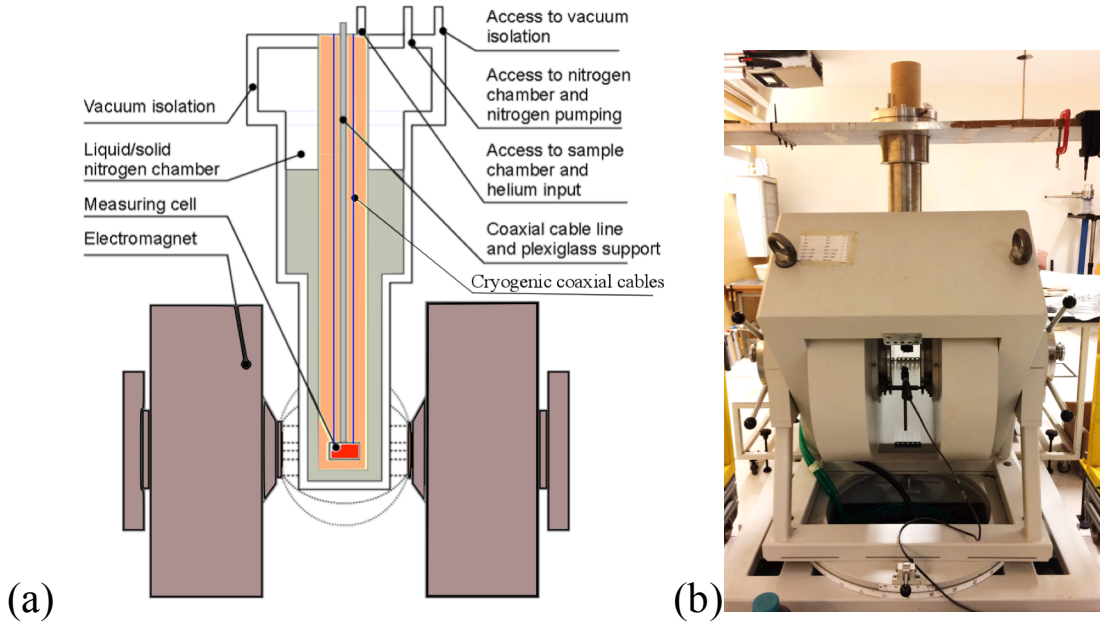

Fig. 4.3. (a) A schematic representation of the cryostat section. (b) A photograph of the cryostat at Roma Tre University.

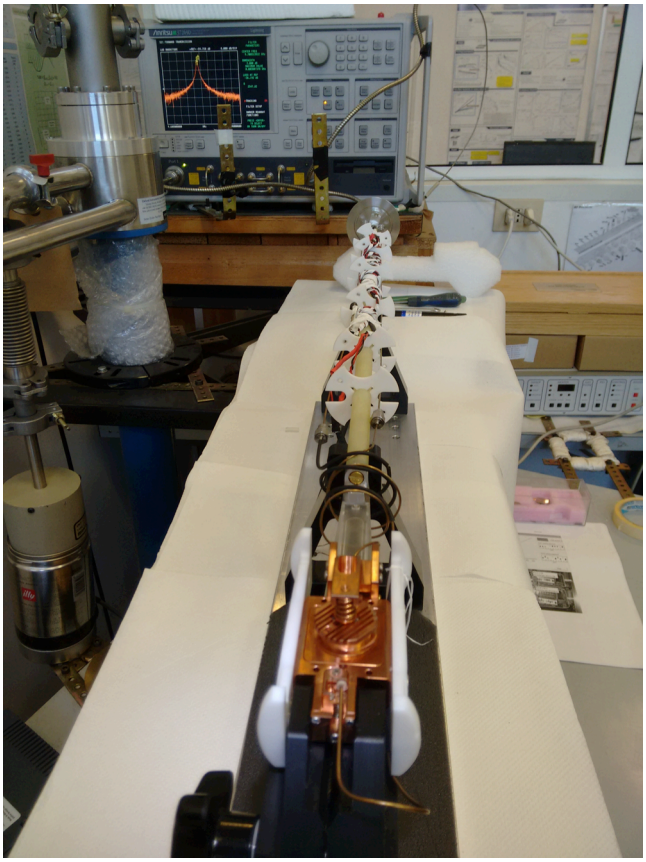

Fig. 4.4. A photograph of the microwave line.

Figure 4.3 shows the liquid nitrogen cryostat used for the measurements. In the outer chamber, thermal insulation is provided by a $5 \cdot 10^{-6}$ mbar vacuum. The intermediate chamber is filled with liquid nitrogen. The cryostat reaches the temperatures around 65 K by pumping the liquid nitrogen evaporation with a rotary pump. The inner (sample) chamber contains the cryogenic insert, which includes the resonator and the microwave line (Fig. 4.4), and the measuring cell. After filling of the cryostat, inside the sample chamber low-pressure helium atmosphere is created (around 0.2 mbar) to make thermal exchange with the nitrogen bath. The cryostat is inserted inside the air gap (~ 80 mm) of a conventional electromagnet (Bruker BE25V). This electromagnet allows to generate a static magnetic field up to $\mu_0 H_{max} = 0.7$ T. It is powered by the current source Bruker BSMPS-BIP1 with $I_{max} =$ 17 A. Besides the two main magnet coils, there are additional compensated coils to

reduce the residual magnetic field, which appears during the magnetic field cycles. The intensity of the magnetic field is detected by a Hall sensor (placed in the middle, between the magnet coils, on the level of the sample) and measured by a gaussmeter Walker MG-3D. The magnet is installed on the rotatable base, which allows varying the orientation of the magnetic field up to 360º.

Microwave measurements were performed on similarly processed samples as described in Chapter 2, but non-patterned. I used a sapphire cylindrical dielectric resonator operating at the frequency $\nu \sim 47.7$ GHz in the TE_{011} mode, which ensures planar circular currents on the film plane. Field sweeps were performed in DC magnetic field $\mu_0 H < 0.8$ T perpendicular to the surface of the samples (field aligned with the *c*-axis) at fixed temperatures to avoid the well-known deleterious effect of $SrTiO_3$ substrate resonances [107], [111].

4.3 Microwave properties of PLD films

4.3.1 PLD YBCO films with $BaZrO_3$ nano-columns

The field dependence of the change in the complex effective surface impedance is presented on Fig.4.5 for PLD YBCO – 5% BZO (Fig. 4.5 (a)) and PLD YBCO – 7% BZO (Fig. 4.5 (b)) at 77 K and 67 K. The lower directly measured resistive response ΔR value of the films at lower temperature (67 K) indicates the reduced dissipation in the vortex state with respect to the higher temperature (77 K) [81]. This

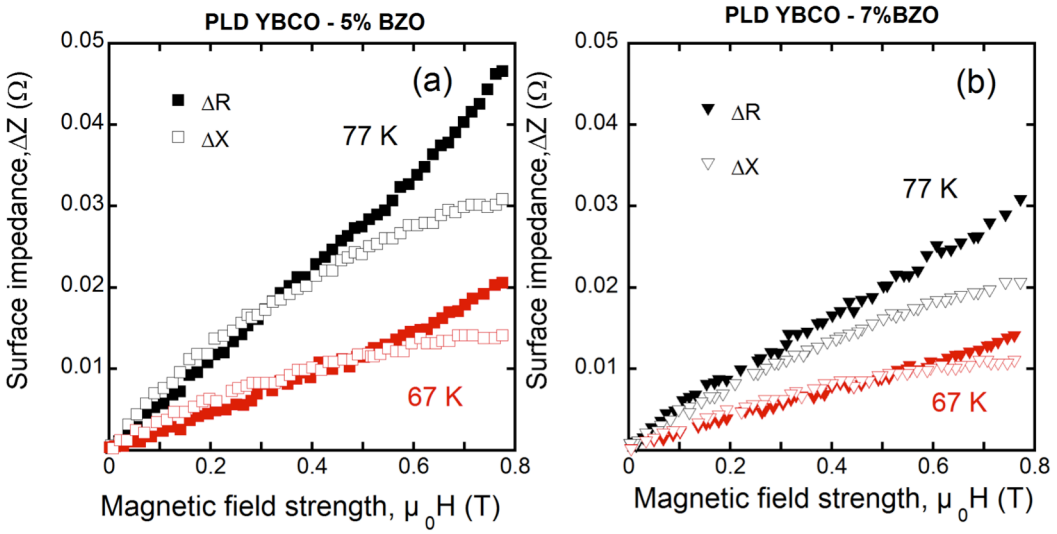

Fig. 4.5. Field-induced change of the complex surface impedance in (a) PLD YBCO – 5% BZO and in (b) PLD YBCO – 7% BZO. Only 50% of the data are shown to avoid crowding.

correlates with DC electric measurements as critical current density J_c values are increasing with decreasing the temperature (see Chapter 3.3.1). The vortex state microwave dissipation is lower for YBCO – 7% BZO with respect to the film with 5% of doping in all the field range, which indicates stronger pinning.

The pinning parameter r quantitatively confirms the strong pinning in the 5% BZO doped sample with larger values of r in magnetic fields $\mu_0 H < 0.5$ T at 77 K (Fig. 4.6 (a)). However, the parameter r in this sample decreases with T more sharply than in YBCO – 7% BZO, which has a gradual decrease. Resorting to the GR model (see Chapter 1 and Eq. 4.6), a further analysis can be carried on by comparing the pinning constant $k_p(H)$ (Fig. 4.6 (b)). The pinning constant in the YBCO – 5% BZO sample differs from the other sample, in that it shows a pronounced decrease with the field, while YBCO - 7% BZO has a weaker field dependence with higher k_p values. It emerges that the pinning wells in YBCO – 7% BZO keep their steepness better than in YBCO – 5% BZO in the measured magnetic field range. This proves that vortex pinning is getting more efficient with increasing the magnetic field and lowering the temperature in the sample with higher percentage of BZO inclusions [108].

4.3.2 PLD YBCO film with $Ba_2Y(Nb/Ta)O_6$ nano-columns

Field sweeps for PLD YBCO – 5% BYNTO film were performed at different temperatures in the range of 65-83 K. The trend in a change of the surface impedance

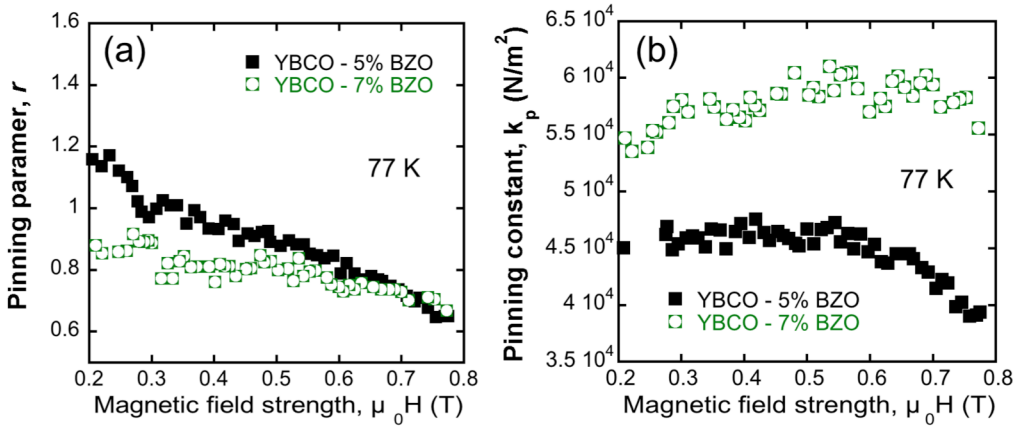

Fig. 4.6. (a) Pinning parameter r and (b) pinning constant k_p for PLD YBCO – 5% BZO (full squares) and in PLD YBCO – 7% BZO (open circles). Only 50% of the data are shown to avoid crowding. Data below $\mu_0 H \approx 0.2$ T are omitted due to large numerical scattering.

is shown in Figure 4.7. As it can be seen, the field dependent ΔR and ΔX parts progressively decrease with decreasing the temperature. Again, this indicates the reduction of the dissipation in the vortex state. The imaginary part ΔX is consistently larger than ΔR up to 80 K. Thus, the vortex elastic recall energy, related to pinning, is larger than the dissipation. Comparing the data of the Figure 4.7 to Figure 4.2, this is an indication for very steep pinning wells originating from BYNTO nano-columns.

A plot of the pinning parameter r (Fig. 4.8 (a)) and the pinning constant k_p (Fig. 4.8 (b)) demonstrates a weak field dependence for all the measured temperatures, with a smooth decrease in r at very low magnetic fields. k_p is approximately constant with the field. It emerges that the pinning wells in YBCO/BYNTO keep their steepness in the entire field range under study. Moreover, r and k_p are noticeably enhanced with respect to the previously reported studies for YBCO/BZO samples [81], [103], [113].

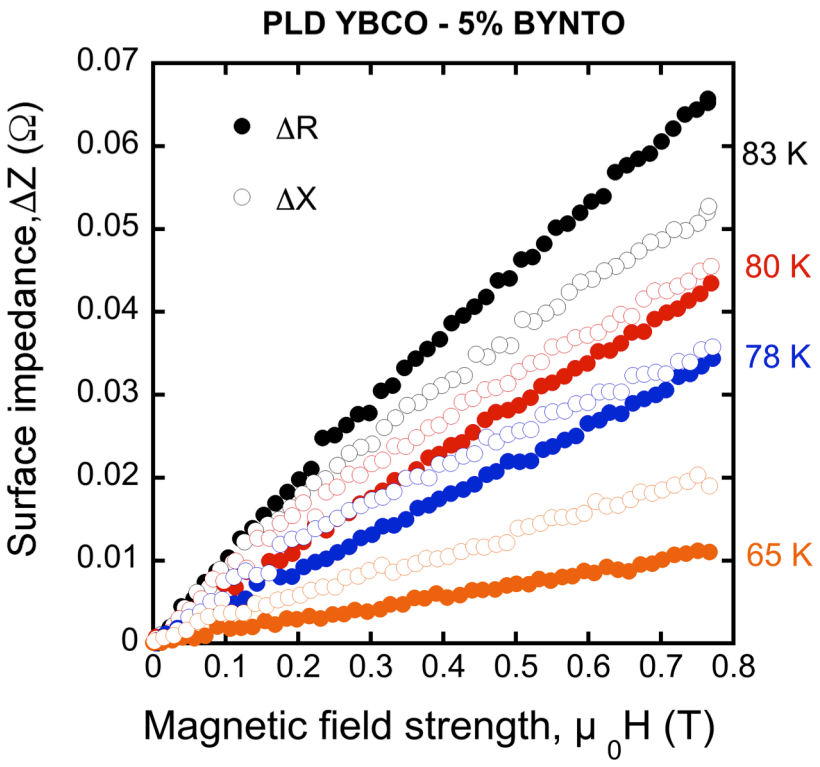

Fig. 4.7. Field-induced change of the complex surface impedance in PLD YBCO - 5% BYNTO. Only 50% of the data are shown to avoid crowding.

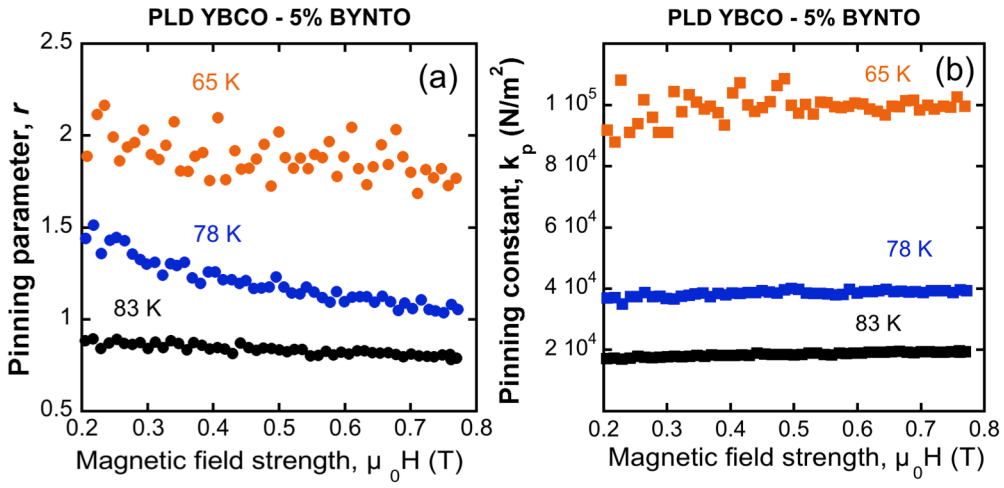

Fig. 4.8. (a) Pinning parameter r and (b) pinning constant k_p for PLD YBCO – 5% BYNTO measured at 83 K, 78 K and 65 K. Only 50% of the data are shown to avoid crowding. Data below $\mu_0 H \approx 0.2$ T are omitted due to large numerical scattering.

4.4 Microwave properties of MOD films

Microwave measurements for MOD derived films were performed only in pristine YBCO and YBCO – 5% BZO samples.

4.4.1 Pristine MOD YBCO film

Figure 4.9 presents the surface impedance dependence on the magnetic field at various temperatures. Different to the PLD samples, the field dependences of both the real (ΔR) and imaginary (ΔX) parts in MOD pristine film look very similar at higher temperatures, with a decrease only at 65 K. The imaginary part ΔX is always smaller than ΔR in this temperature range indicating rather broad pinning wells.

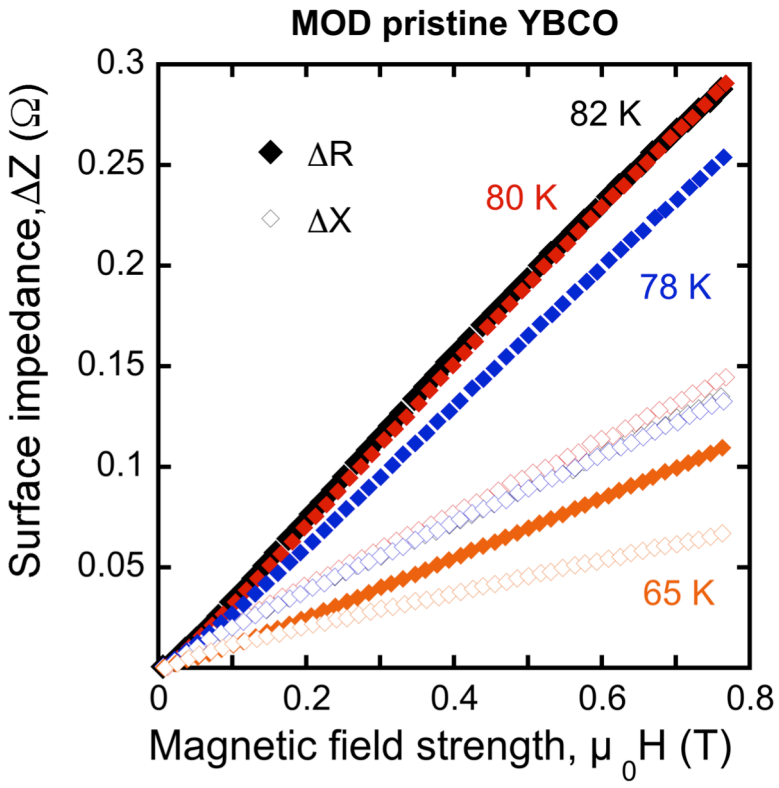

Fig. 4.9. Field-induced change of the complex surface impedance in MOD pristine YBCO film. Only 50% of the data are shown to avoid crowding.

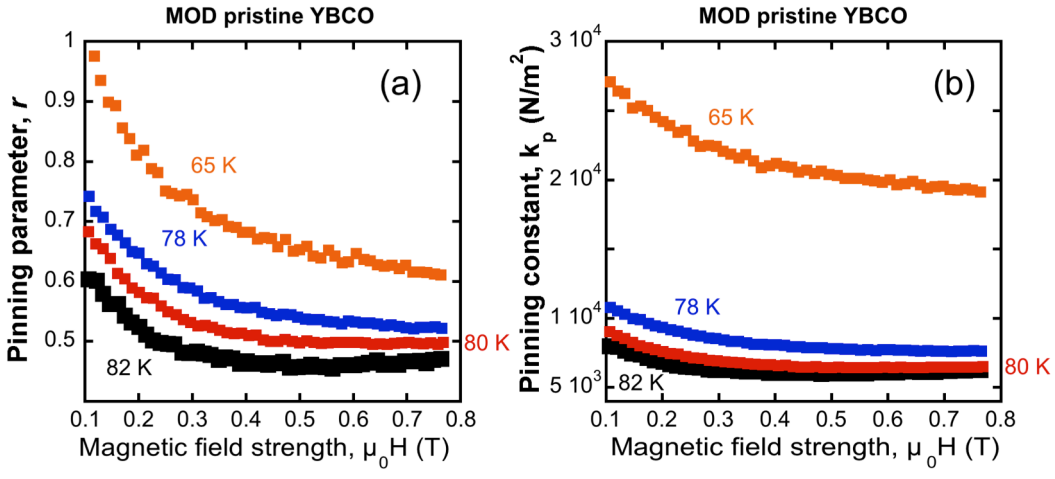

Fig. 4.10. (a) Pinning parameter r and (b) pinning constant k_p for the MOD pristine YBCO film measured at 82 K, 80 K, 78 K and 65 K. Only 50% of the data are shown to avoid crowding. Data below $\mu_0 H \approx 0.1$ T are omitted due to large numerical scattering.

The field dependence of r and k_p is reported on Fig. 4.10. It can be seen that at every temperature reported, $k_p\,(H)$ is a decreasing function in the lower field. This is in contrast with the observations in PLD-grown YBCO/BZO samples in this study and in previous works [102], where $k_p\,(H)$ is almost constant, or weakly field dependent. The latter feature has been connected to the columnar organization of BZO in PLD samples.

4.4.2 MOD YBCO films with $BaZrO_3$ nano-inclusions

The field-induced behaviour of the complex surface impedance obtained in MOD YBCO – 5% BZO film (Fig. 4.11) is similar to the behaviour in pristine sample, with a difference in the absolute values of the reactance (ΔX) and the resistance (ΔR). These values are as much as twice lower in 5%BZO film than in previous pristine YBCO.

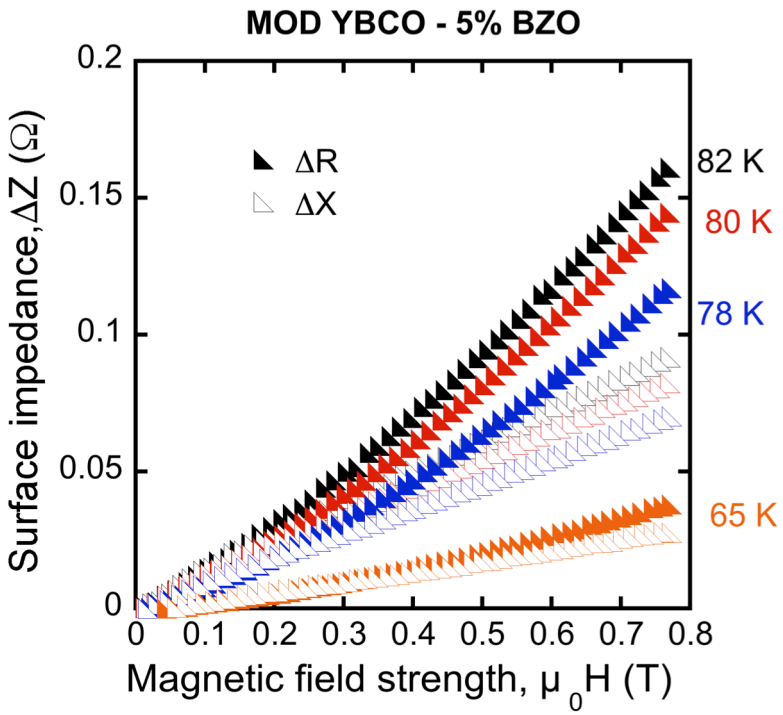

Fig. 4.11. Field-induced change of the complex surface impedance in MOD YBCO – 5% BZO film. Only 50% of the data are shown to avoid crowding.

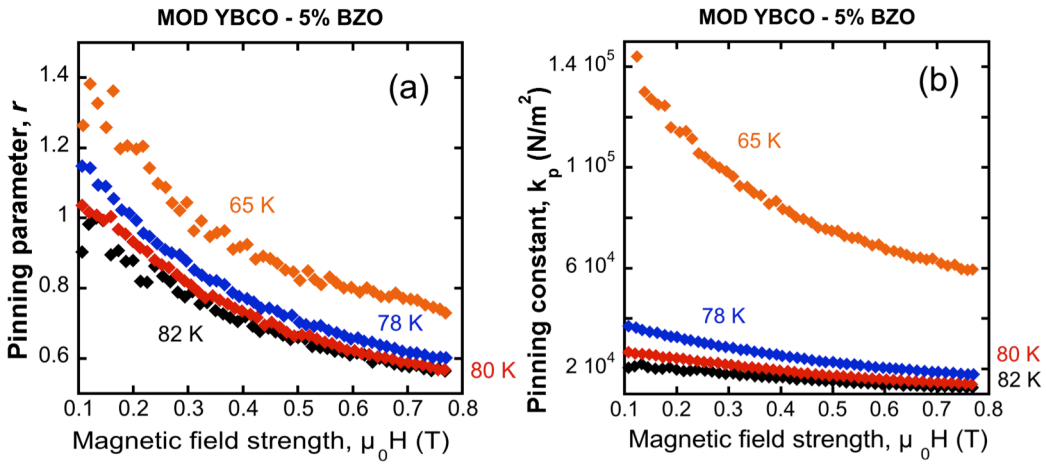

Fig. 4.12. (a) Pinning parameter r and (b) pinning constant k_p for MOD YBCO – 5% BZO film measured at 82 K, 80 K, 78 K and 65 K. Only 50% of the data are shown to avoid crowding. Data below $\mu_0 H \approx 0.1$ T are omitted due to large numerical scattering.

That is especially noticable at higher magnetic fields: $\Delta R \sim 0.15$ Ω and $\Delta R \sim 0.30$ Ω at 82 K, 0.75 T, respectively.

On a contrary with previously discussed doped PLD films, field dependence of r and k_p in MOD YBCO – 5% BZO film (Fig. 4.12) has a different behaviour: r and k_p constantly decrease with decreasing the field. This indicates the different pinning mechanisms coming from BZO nanoinclusions in MOD and PLD films. Nanoparticles in MOD YBCO do not have strong correlated contribution and do not act as strong pinning sites at low fields, which is opposite to the PLD BYNTO samples with almost constant field dependence of k_p due to strong pinning by the columnar defects.

4.5 Summary

This Chapter discussed the use of microwave measurement with a brief description of the technique, including some details about the evaluation of the main microwave observables – the complex surface impedance, the pinning parameter r and the pinning constant k_p. All these parameters were analyzed for most of the YBCO films.

A vortex state microwave dissipation is lower for YBCO – 7% BZO with respect to the film with 5% of doping in all the field range, which indicates stronger pinning. The vortex pinning is getting more efficient with increasing the magnetic field and lowering the temperature in the sample with higher percentage of BZO inclusions.

The imaginary part ΔX is consistently larger than ΔR in YBCO/BYNTO film up to 80 K. Thus, the vortex elastic recall energy, related to pinning, is larger than the dissipation. The pinning parameter r and the pinning constant k_p demonstrates a weak field dependence in this sample, with a smooth decrease in r at very low magnetic fields. k_p is approximately constant with the field. It emerges that the pinning wells in YBCO/BYNTO keep their steepness in the entire field range under study.

The imaginary part ΔX in MOD pristine YBCO is always smaller than ΔR in this temperature range indicating rather broad pinning wells. The field-induced behaviour of the complex surface impedance obtained in MOD YBCO – 5% BZO film is similar to the behaviour in pristine sample, with a difference in the absolute values of ΔX and ΔR. These values are as much as twice lower in 5%BZO film than in the pristine YBCO film.

Further comparison of microwave properties will be given in Chapter 5.

Chapter 5

Vortex flux pinning in YBCO thin films

Magnetic flux pinning and its mechanisms are under continuous study since the discovery of superconductivity. Even though a massive progress has been achieved in that study, in High-Temperature Superconductors (HTS) there is still room for a better understanding, leading to better performances. In fact, only advanced control of growth process, transport properties, architecture and fabrication will guarantee a secure and unaltered performance over long periods of time and according to the requirements for HTS application. Power applications, such as nuclear fusion magnets, demand very strong vortex pinning capable to yield high values of the critical current density (J_c) in high magnetic fields (H) and low temperatures (T).

Previous studies have shown a significant role of the defects, either intrinsic (intergrowths, twin boundaries and dislocations) [36], [85], [88], [91] or artificial (self-assembled nano-columnar inclusions or nano-particles e.g. $BaZrO_3$, BZO) [29], [34], [68], [116]-[121], in their interaction with flux motion in the YBCO transport properties and performance.

This Chapter discusses different aspects of vortex flux pinning in PLD and MOD YBCO films. The first aspect is the effect of twin boundaries on correlated pinning in pristine MOD YBCO (Chapter 5.1). The DC data to investigate this effect were partially presented in Chapter 3 but analysed from a different perspective. A boundary between vortex pinning and vortex channeling is determined. The second issue under study is the effect of different second phases in PLD films (Chapter 5.2). Some of the DC and microwave data were presented in Chapter 3 and Chapter 4 apart from the pristine PLD YBCO film, which were used as a reference sample to emphasize the effect of secondary phases. The most efficient second phase for vortex

pinning among PLD samples is reported and conclusions are made based on the obtained new graphs. The different concentration of APCs in MOD films is another aspect, which has been studied (Chapter 5.3). The DC and microwave data were partially presented in Chapter 3 and Chapter 4, but were analysed from secondary phases concentration point of view with deriving new dependences. Finally, the experimental correlation between the two measurement techniques, used in this study, is determined (Chapter 5.4).

5.1 Effect of Twin Boundaries in MOD pristine YBCO

The relevant role of twin boundaries (TBs) in flux pinning for a variety of different samples has been extensively studied over the last decades [28], [36], [37], [82], [122]-[124]. It was shown that the influence of TBs on vortex pinning has a complex character and that TBs can act as strong pinning centres, thus increasing the critical current, or as vortex channels, increasing the dissipation instead. TBs have a high impact on the critical current and depends on temperature, applied magnetic field, vortex motion direction, microstructure and TBs orientation [35], [36], [87], [122], [125]. Other defects present in a film, such as low angle grain boundaries, *a-b* planes, oxygen vacancies, add to the complexity of the superconductor structure [36], [126], [127]. As it was shown in [36], even the choice of the buffer layer can be an important factor in achieving the best configuration to obtain vortex pinning instead

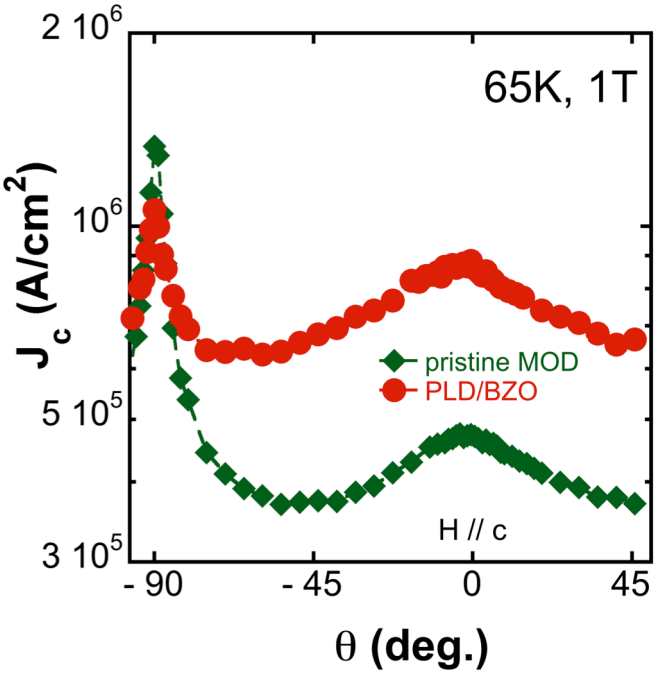

Fig. 5.1. Angular critical current density in pristine MOD (diamonds) and PLD/BZO (full circles) YBCO samples. TBs in MOD are acting as pinning centers, similar to nanocolumns in PLD films.

of channeling. It should be recalled that the effect of twin boundaries is directional: the effect, whether pinning or channeling, is most evident when the field is along the TB plane. Moreover, according to the model for vortex trapping by TBs by Blatter *et al*. [9], the vortex lattice adjusts to the twin planes when the angle between the magnetic field and the TBs is small (i.e. H //*c*-axis). Thus, an investigation of the angle-dependent properties is expected to help in understanding of the role of TBs.

In order to gain control and better understanding over the microstructure and the pinning properties of commercially interesting BZO-doped MOD samples, it is useful to study and compare better-controlled materials, such as samples grown by pulsed laser deposition, or undoped MOD samples. For this purpose, the angle (θ) and field (H) dependencies of J_c in the MOD pristine YBCO film have been compared to the behaviour of the PLD YBCO – 7% BZO as a reference for a correlated-pinning system.

Figure 5.1 presents $J_c(\theta)$ recorded at relatively high temperature ($T = 65$ K) and low field ($\mu_0 H = 1$ T). Both samples demonstrate a pronounced correlated pinning effect with a broad peak in $J_c(\theta)$ centred at $\theta = 0°$. The PLD sample shows the angular J_c behaviour typical of samples with strong correlated pinning due to BZO nano-coloumns, as was shown in Chapter 3 and other works [92], [101], [128], [129]. For what concerns the pristine MOD sample, a similar broad peak can be observed at $\theta = 0°$ indicating the presence of *c*-axis correlated defects, effective in a wide angular range. This is consistent with the behaviour of MOD films reported at relatively high temperatures ($T > 50$K) [33] in the presence of strong vortex pinning at magnetic field H //*c*-axis [35], [82], [89], [90]. The sharper peak at $\theta = 90^o$ (near *a*-*b* planes) in both samples is associated with the intrinsic pinning arising from the layered structure of YBCO material [93], [121] (see Chapter 1.4). One should conclude that twin planes (in the pristine MOD film) and nanocolumns (in the PLD 7% BZO film) act similarly. To investigate further this similarity, $J_c(H)$ at $\theta = 0°$ and different T were performed.

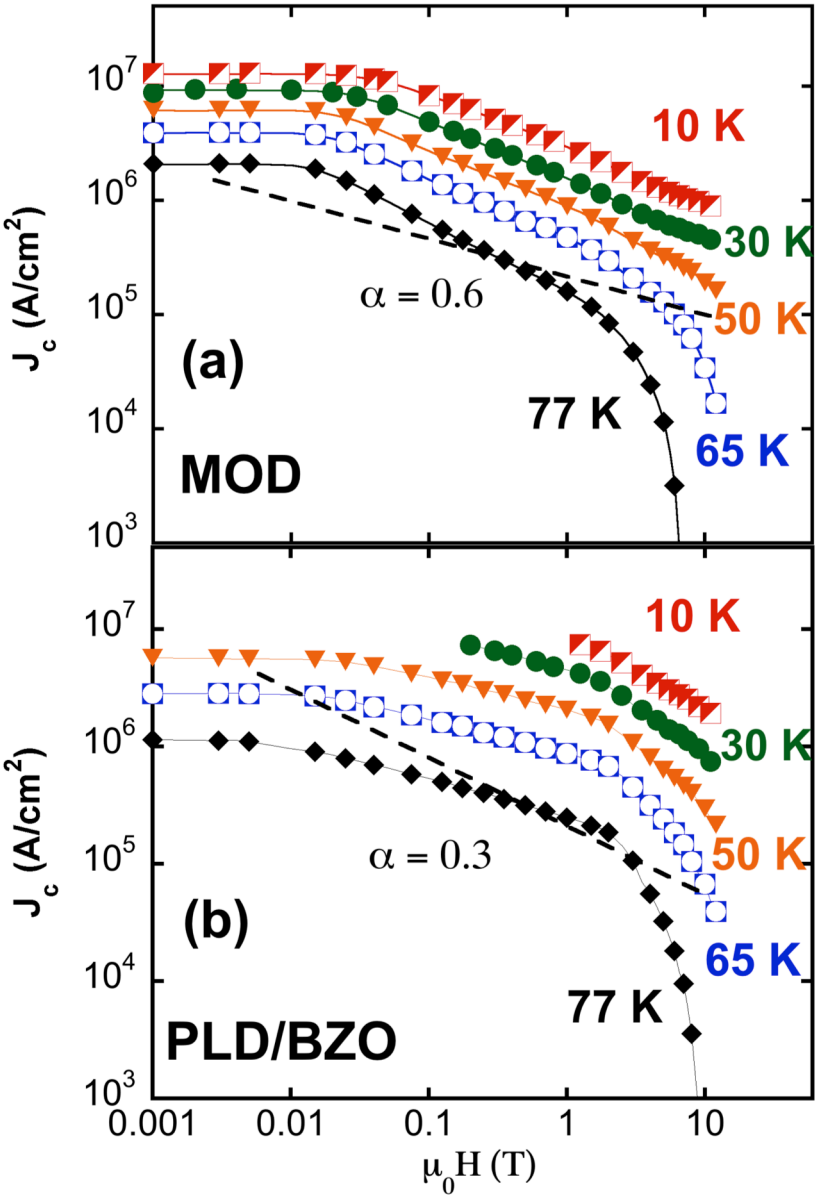

Fig. 5.2. Log-log plot of critical current density as a function of the applied magnetic field obtained for pristine MOD YBCO (a) and PLD YBCO - 7% BZO (b) samples at different temperatures in the range of 10 - 77 K, at $\theta = 0°$.

Figure 5.2 shows the magnetic field dependence of the critical current density in pristine MOD YBCO (Fig. 5.2 (a)) and PLD YBCO – 7% BZO (Fig. 5.2 (b)) films. The doped PLD sample exhibits the typical features of PLD YBCO described previously in Chapter 3: the plateau region up to about $\mu_0 H = 0.01$ T, followed by the power-law behaviour $J_c \sim H^{-\alpha}$, and then by the kink after 1 T with a sharper decrease

in J_c. In the present PLD YBCO/BZO sample, the coefficient $\alpha = [0.28\text{-}0.31]$ (see Chapter 3) and this indicates that nano-columns act as strong vortex pinning centres.

A similar J_c field dependence $J_c(H)$ exists in the MOD sample, with the same three behaviours – the plateau, the kink (more evident at 77K and 65K) and, most importantly, the power-law dependence (an indication of the presence of correlated defects). Crucial differences, nevertheless, exist: J_c in the MOD film decreases faster than J_c in PLD/BZO (larger α) with increasing magnetic field at all measured temperatures: in the MOD pristine sample α is close to the theoretical value $\alpha = 0.5$ ($\alpha = 0.6$ at 77 K, but approaches $\alpha = 0.5$ with decreasing the temperature) and hints to the planar nature of correlated defects. This difference in J_c retention (power-law decrease) is then related to the different pinning nature – planar in pristine MOD and columnar in PLD/BZO.

With increasing H and lowering T, a striking change in $J_c(\theta)$ is reported for pristine MOD YBCO sample only. As shown in Figure 5.3, the angular critical current density at high field (7 T) and low temperature (30 K) in the MOD YBCO sample exhibits a clear dip around $\theta = 0°$: the peak at high T transformed into a dip – an imprint of channeling. By contrast, the PLD/BZO sample still shows a peak at

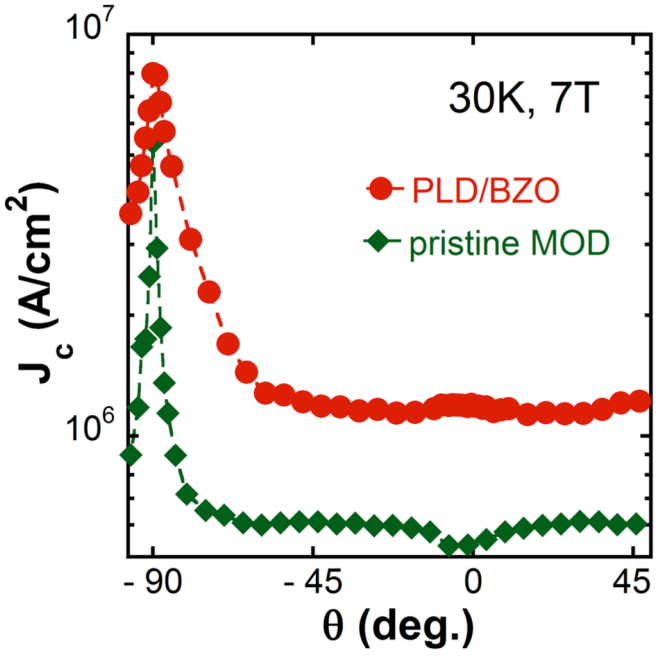

Fig. 5.3. $J_c(\theta)$ in pristine MOD YBCO (diamonds) and in PLD YBCO/BZO (full circles). Existence of vortex channeling at these field and temperature in MOD YBCO is clear (compare to Fig. 5.1), as well as the persistence of directional pinning in PLD – 7% BZO sample.

$\theta = 0°$: albeit of much reduced height with respect to high T, the correlated pinning is still strong.

Extended defects transform then differently in the different materials at low temperature (T < 50K) and high fields. The measurements show that at low T and high H TBs favour vortex channeling, consistently with previous findings [33], [36], [82]. The J_c dip observed in the MOD film can be described by the flux cutting model [82], [130]: according to that model, once pinning centres become strong enough (i.e. when field increases and temperature decreases) to pin one or several vortices while the latter are moving in the flux, vortex segments could be cut out of these vortices and cross-join each other thus creating free loops within a weak pinning plane (Fig. 5.4). This release of vortex segments without depinning the whole vortices creates current losses and one has a dip in J_c curves, which is indeed observed in the present pristine MOD film.

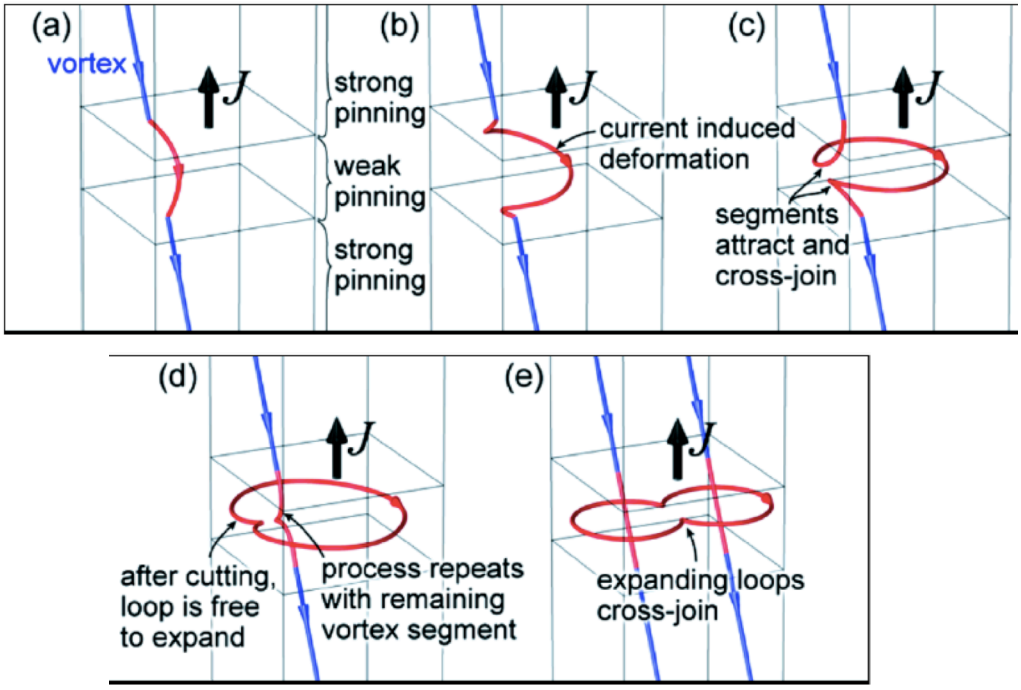

Fig. 5.4. A schematic diagram of the vortex distortions necessary for continuous dissipation, as taken from [131].

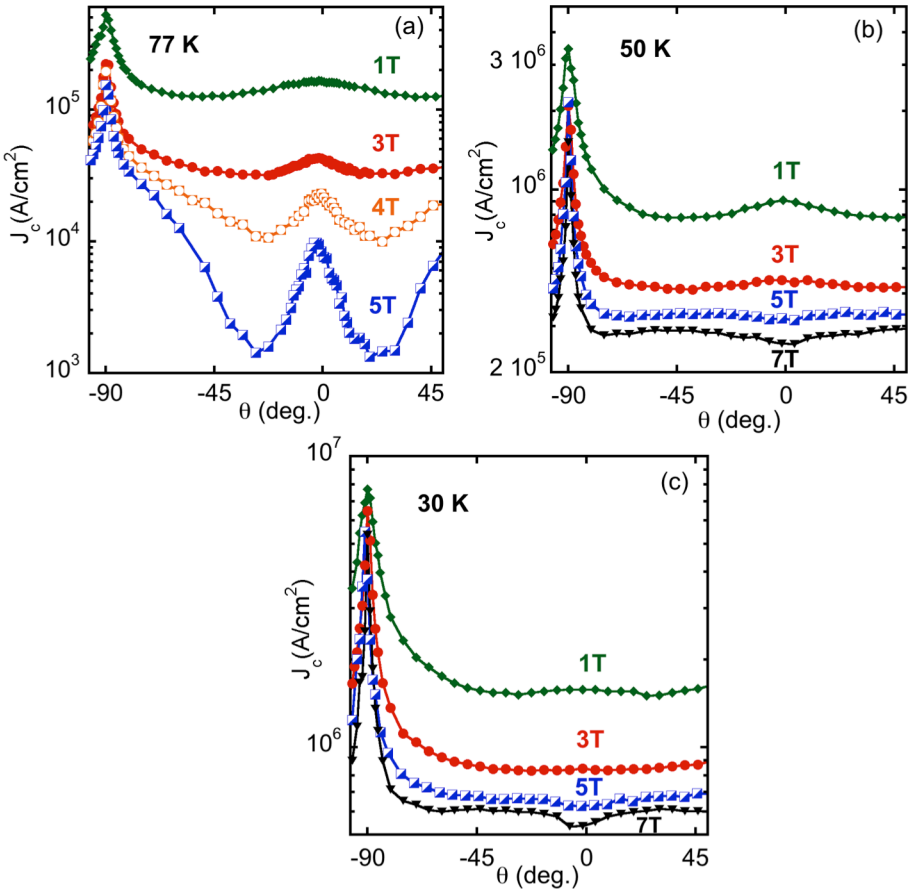

Fig. 5.5. Angular dependence of J_c for pristine MOD film measured at (a) 77K, (b) 50K, and (c) 30K with different applied magnetic fields. The crossover from directional pinning and vortex channeling with increasing field is evident at 50 K and 30 K: the peak at θ = 0° transforms into a dip. Note the different J_c scales for each plot.

A complete characterization of this feature at $\theta = 0°$ with a change in field and temperature and special attention to the crossover from directional pinning to vortex channeling, is reported in Figure 5.5. At 77K (Fig. 5.5 (a)) clear directional pinning is observed, with TBs acting as strong pinning sites enhancing J_c at $\theta = 0°$ up to 5 T. Remarkably, the enhancement of $J_c(0°)$ increases with increasing the applied magnetic field. At lower temperatures (T = 50K, Fig. 5.5 (b)) the trend is completely different: with increasing the magnetic field the peak in J_c at $\theta = 0°$ decreases, then vanishes and ultimately transforms into a dip between 3 T and 5 T. At even lower temperature (T=30 K, Fig. 5.5 (c)) the trend is the same, but the dip deepens. In general, the channeling minimum gets more prominent with increasing the magnetic field and decreasing the temperature.

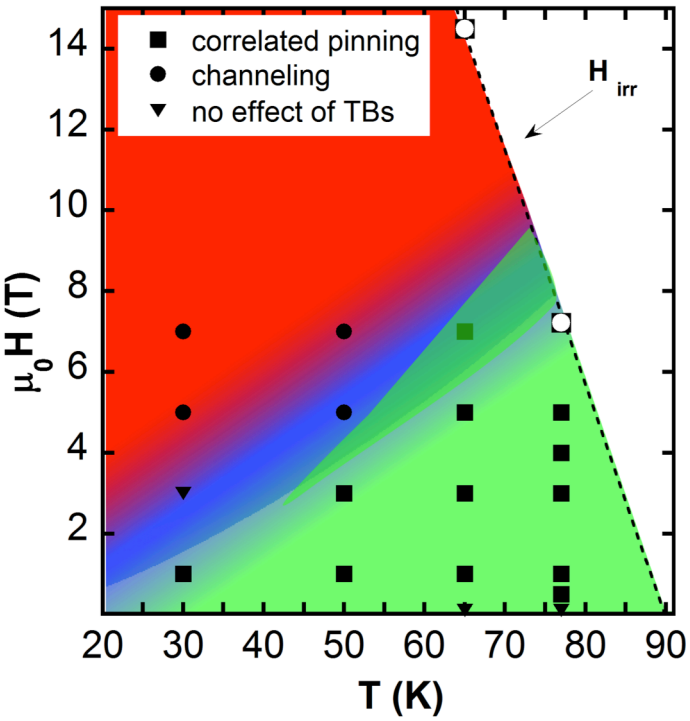

Fig. 5.6. The *H-T* diagram indicating correlated pinning and channeling areas based on twin boundaries contribution to the critical current density in pristine MOD YBCO thin film.

Based on the obtained results, the role of TBs can be determined in $H - T$ diagram for the pristine MOD YBCO sample: the boundary between vortex pinning and vortex channeling regimes can be identified (Fig. 5.6).

The boundary region was determined as an area where competing effect on J_c values between pinning and channeling was found at certain magnetic fields and temperatures. The identification of the crossover line in the $H - T$ diagram is a useful tool to better understand the complex behaviour of vortex motion in REBCO, and to determine the performances of REBCO in application (channeling is deleterious to the performances).

A final important observation must be done with respect to Figure 5.6: in the high magnetic field range, the effectiveness of extended defects is progressively reduced by lowering the temperature, suggesting that at low temperatures the dominant pinning contribution arises from isotropic pinning centres [34].

After the correlated pinning contribution has been observed in pristine MOD sample, the logical way was to compare this pristime sample with another MOD film containing BZO nano-inclusions. The difference in J_c (θ) between MOD pristine and

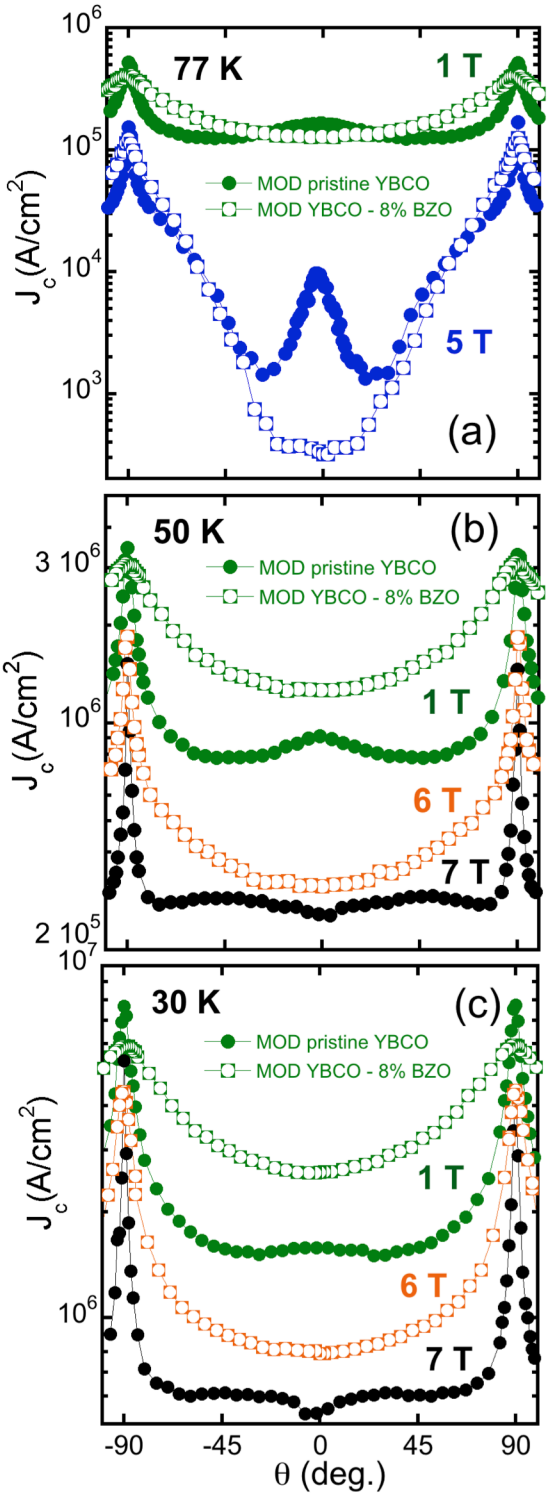

Fig. 5.7. Angular dependence of J_c for pristine MOD and MOD YBCO – 8% ZBO film measured at 77K (a), 50K (b), and 30K (c) with different applied magnetic fields. Note the different J_c scales for each plot.

the 8% doped sample is shown in Figure 5.7. One can notice not only the absence of any correlated pinning and of any evidence for channeling in YBCO – 8% BZO film, but also the enhancement of J_c in a wide angular range comparing to the pristine MOD as temperature goes down. Pristine sample dominates only around $\theta = 0°$ at 77 K.

From these features it emerges the essential role of the introduction of 3D APCs, such as $BaZrO_3$ nano-inclusions, in MOD YBCO films. Such form of isotropic pinning sites destroys almost completely the contribution of TBs, be it pinning or channeling. Althrough the J_c is decreased at high T, high H (Fig. 5.7 (a)), this is more than compensated by the much larger J_c at lower T.

5.2 Effect of different APCs in PLD YBCO thin films

Since perovskite-like $BaZrO_3$ nano-inclusions have proved to be effective APCs, other several nano-scale pinning additions as the double perovskite-like Ba_2YNbO_6 (BYNO), Ba_2YTaO_6 (BYTO) or their combination have been studied in the last decade [68], [80], [120]. One of the most intriguing features of such phases is the easy development of a complex landscape of defects by mixed doping. A proper combination of columnar, planar and nanoparticle defects in 2.5 mol.% BYTO + 2.5 mol.% BYNO doped-YBCO films has been reported as a very effective pinning source.

In this part of the Chapter, the transport and vortex pinning properties of the YBCO film grown by PLD with addition of $Ba_2Y(Nb/Ta)O_6$ (BYNTO) were compared to the BZO added YBCO using the DC (long-range vortex motion) and the microwave (small-displacement vortex motion) measurement techniques.

5.2.1 Comparison of DC electric transport properties

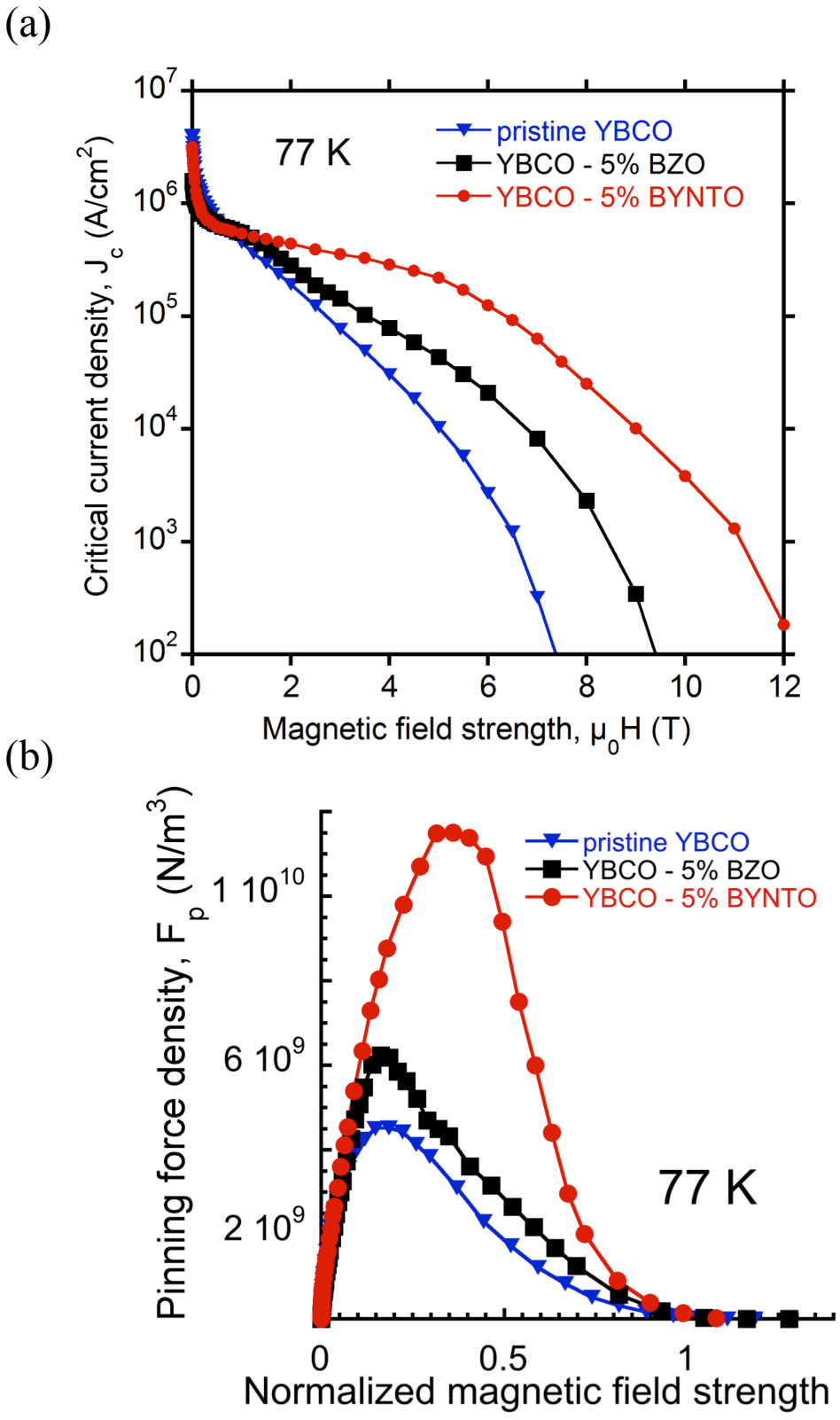

Fig. 5.8. (a) Critical current density as a function of the applied magnetic field and (b) the pinning force density as a function of the normalized field at 77 K for YBCO/BYNTO (red full circles), YBCO/BZO (black full squares). Pristine YBCO film (blue full triangles) in J_c *(H)* is used as a reference.

Figure 5.8 (a) presents the field dependences of the critical current density, $J_c(H)$, at 77 K for PLD YBCO/BZO and YBCO/BYNTO films, and for a PLD pristine YBCO film used as a reference. An overall increase of the in-field performances in doped samples with respect to the pristine YBCO is clearly observed and indicates the efficiency of the APCs. Whereas in the low-field region ($\mu_0 H \leq 2$ T) the J_c values and their behaviours are similar for both doped samples, the YBCO/BYNTO film has a much better J_c retention as the magnetic field increases. In fact the YBCO/BYNTO sample shows an extended plateau-like region up to around 5.2 T, whereas a kink with a pronounced J_c drop at about 1 T is observed in the YBCO/BZO film. Figure 5.8 (b) shows the pinning force density $F_p = J_c \times B$ as a function of the normalized magnetic field strength at 77 K for YBCO/BZO and YBCO/BYNTO samples. The BYNTO added YBCO film exhibits higher F_p with respect to the BZO doped sample with maximum values $F_p^{max} = 11.5$ GN/m^3 and $F_p^{max} = 6.2$ GN/m^3, respectively. The irreversibility field H_{irr} (evaluated by using the criterion $F_p(H_{irr}) = F_p^{max}/100$) in the BYNTO sample, $H_{irr} = 11.12$ T, is enhanced with respect to $H_{irr} = 8.61$ T obtained in the YBCO/BZO film. The different in-field behaviour between the two doped samples indicates that the introduction of BYNTO is particularly effective at higher magnetic fields. This is consistent with the larger density of BYNTO nano-columns as compared to BZO nanorods, as reported in Chapter 2.

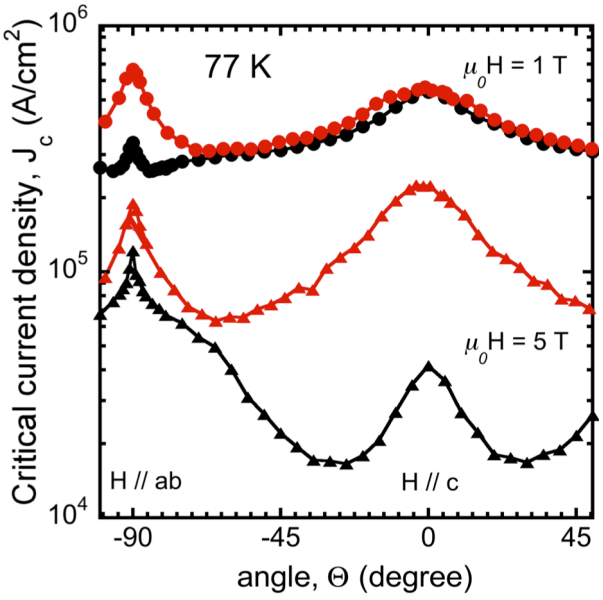

Fig. 5.9. Critical current density as a function of the applied field direction (0° corresponds to H // film c-axis) for the YBCO/BYNTO (red symbols) and YBCO/BZO (black symbols) at 77 K and magnetic field values of 1 T and 5 T.

Angular measurements of the critical current density are reported in Figure 5.9 at two different magnetic fields, 1 T and 5 T. A clear correlated pinning contribution from APCs is observed in both samples when the field is parallel to the columns ($\theta = 0^{\circ}$). The peak height and width are similar for both samples at $\mu_0 H = 1$ T and $\theta = 0^{\circ}$, while at 5 T a significant enhancement of J_c is present in YBCO/BYNTO. Not only the J_c magnitude is higher in BYNTO doped film at high fields ($\mu_0 H = 5$ T) but also the peak is much wider than in the YBCO/BZO film. The combination of *c*-axis aligned BYNTO continuous columns and Y_2O_3 nanoparticles (see Chapter 2) provides a pinning landscape, which results in the J_c improvement in a wider angular range in comparison with YBCO/BZO.

5.2.2 Comparison of microwave properties

A similar effect of the strong pinning in BYNTO doped sample has been observed in microwave measurements, which revealed a significant reduction in the directly measured resistive response ΔR indicating a reduced vortex state dissipation at very high frequency regimes in doped samples, as compared to the pristine YBCO (Fig. 5.10). One can notice that while in the pristine sample the resistance (ΔR) is always above the reactance (ΔX), doped samples have regions where ΔR and ΔX are of the same order. When ΔX is of the same order (or larger) to ΔR, it is an indication of a noticeable vortex pinning. Thus, the beneficial effect of APC is clearly observed

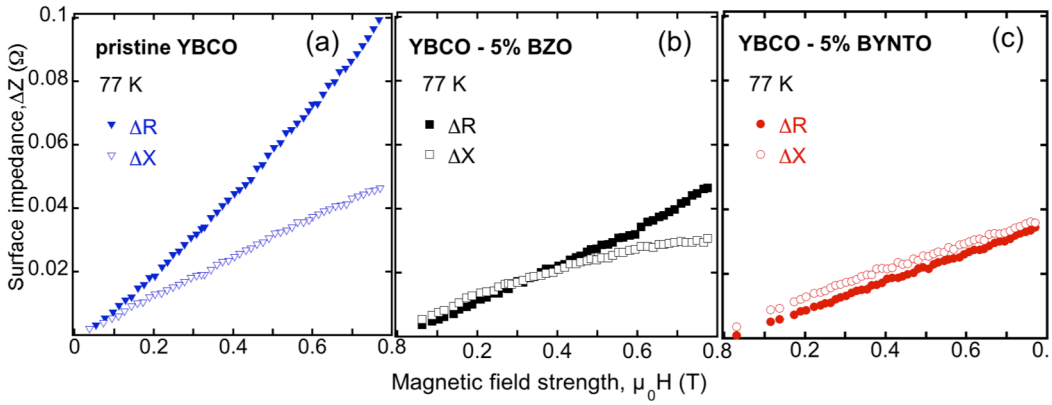

Fig. 5.10. Field variation of ΔZ *(H)* in (a) pristine YBCO; (b) YBCO/BZO and (c) YBCO/BYNTO films at $T = 77$ K: ΔR - full symbols; ΔX - empty symbols. Only 50% of the data are shown to avoid crowding.

in the films with introduced nano-columns. However, differences between the BZO and BYNTO doped samples exist. In YBCO/BYNTO, the imaginary part ΔX in Figure 5.10 (c) is not only of the same order, but even larger than ΔR. Thus, the vortex elastic recall energy, related to pinning, is larger than the dissipation. This is an indication for stronger pinning wells by BYNTO nano-columns with respect to BZO. The pinning parameter r quantitatively confirms the strong pinning in the doped samples with respect to the pristine film: in the YBCO BYNTO, $r > 1$ in all measured magnetic field range with a gradual decrease (Fig. 5.11 (a)). In the YBCO/BZO r has lower values and decreases more sharply, especially at higher fields.

Further analysis is based on the pinning constant $k_p(H)$ (Fig. 5.11 (b)), which elucidates the different nature of the pinning mechanism. The pinning constant in the pristine sample differs from the doped samples, showing a pronounced decrease with the field, whereas YBCO/BZO and YBCO/BYNTO have a much weaker field-dependence. Although the sample with BZO addition has higher k_p, it decreases with the field above 0.9 T, which means that the pinning wells broaden. By contrast, in YBCO/BYNTO one can notice a slight increase of k_p. It emerges that the pinning wells in YBCO/BYNTO keep their steepness at fields larger than in YBCO/BZO, with the crossover taking place at fields ~ 0.8 T. In both cases, r and k_p are noticeably improved with respect to the previously reported studies for YBCO/BZO samples [113], [131], [132].

The presented analysis revealed the effect of different second phases in PLD films. The comparison of PLD derived samples has shown that the combination of *c*-axis aligned BYNTO continuous columns and Y_2O_3 nanoparticles provides the strongest pinning source for vortices among all the samples. Additional information obtained from microwave measurements also proved the most effective pinning by BYNTO columns.

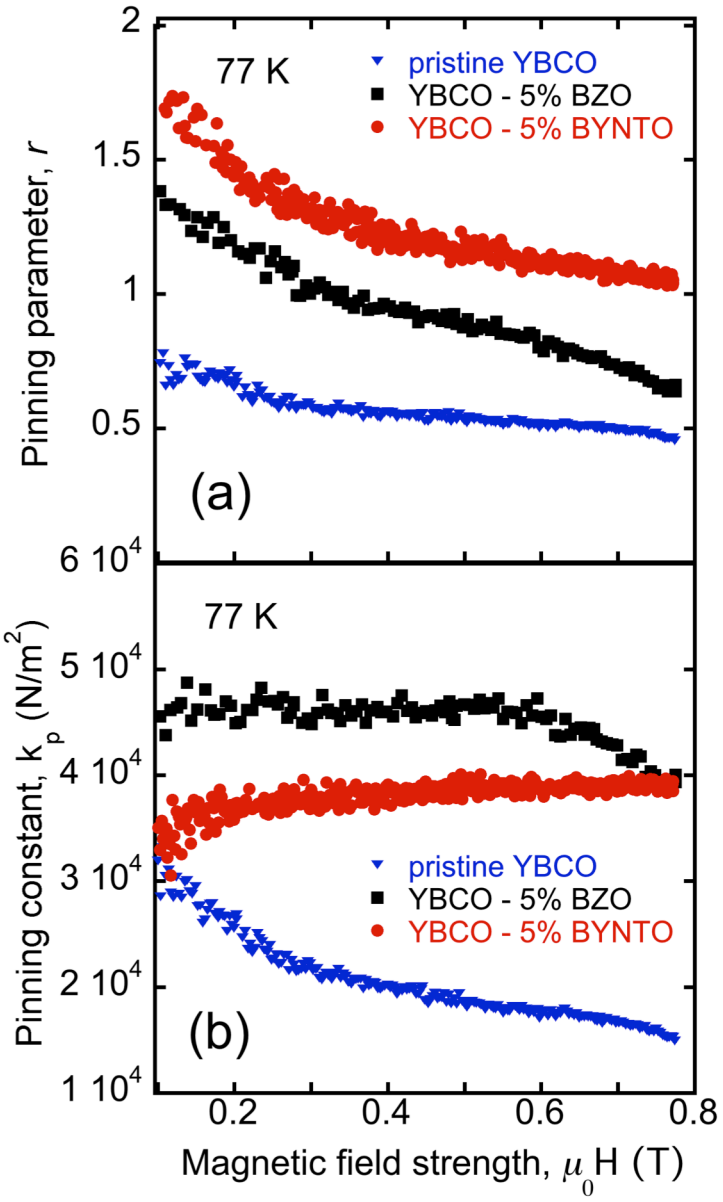

Fig. 5.11. (a) Pinning parameter *r* and (b) pinning constant *kp* for pristine YBCO (blue full triangles), YBCO/BZO (black full squares) and YBCO/BYNTO (red full circles) samples. Only 50% of the data are shown to avoid crowding. Data below $\mu_0 H \approx 0.1$ T are omitted due to large numerical scattering.

5.3 Effect of different APCs in MOD YBCO thin films

Chemically derived YBCO films for coated conductors have a high potential for achieving the required goals in terms of cost and performance in power applications, where development of cheaper conductors is required.

With the aim of understanding at microscopic level the vortex pinning mechanisms of such YBCO films, the transport properties of nanocomposite MOD pristine YBCO and YBCO with 5%BZO and 8% BZO samples have been analysed.

5.3.1 Comparison of DC electric transport properties

The field dependences of the critical current density for pristine YBCO and YBCO with 5% BZO and 8% BZO films are compared in Figure 5.12. One can identifies the *H* - *T* region (boundary given by the dashed black line on Fig. 5.12) where both BZO doped samples perform better and have higher J_c values than pristine film. Going

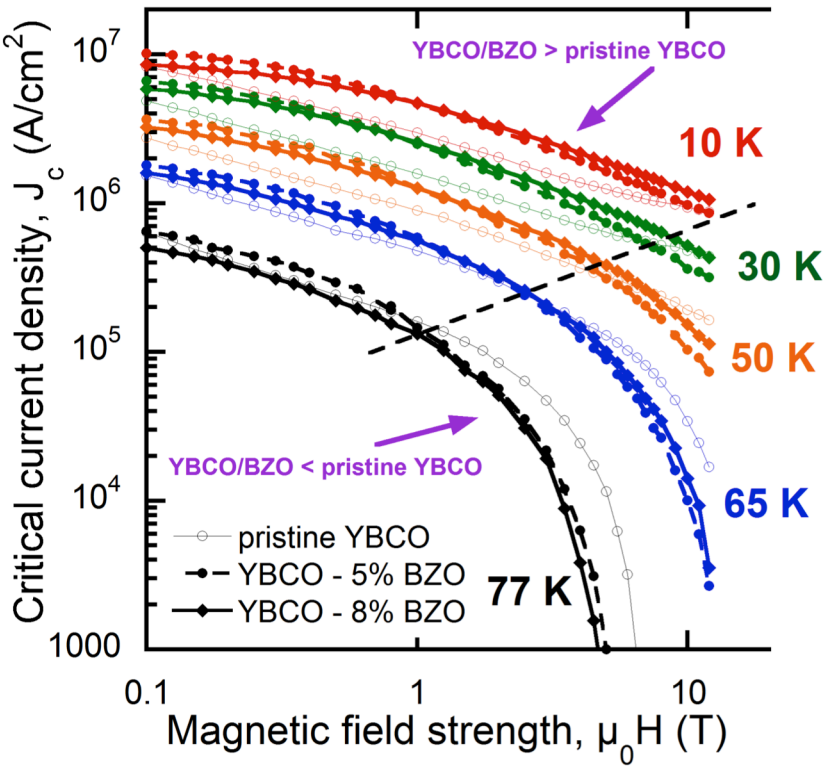

Fig. 5.12. Log-log plot of critical current density as a function of the applied magnetic field obtained for MOD derived pristine YBCO (open circles), YBCO - 5% BZO (full circles) and YBCO – 8% BZO (full diamonds) samples at different temperatures in the range of 77-10 K.

down with temperature this region becomes wider and at 10 K the doped samples have larger J_c than the pristine film almost in the whole measured magnetic field range. That means that at high temperatures APCs are effective only at low magnetic fields, while at low temperatures APCs act as strong pinning sites also at high magnetic fields up to 12 T. This is remarkable, since the opposite has been found in PLD grown samples with correlated columnar defects: in the high magnetic field range, the effectiveness of extended defects (TBs or APCs) is progressively reduced with lowering the temperature. That suggests that at low temperatures the dominant pinning contribution arises from isotropic pinning centres, which are the BZO nano-inclusions in the present MOD YBCO films. This is a positive result in terms of high power applications, which are expected to work at low temperature and in high magnetic fields.

The pinning force density at such conditions (low T – high H) is presented in Figure 5.13. $F_p(H)$ also shows better performance in BZO doped samples, particularly in YBCO with 8% BZO up to 12 T at 10 K (Fig. 5.13 (a)). Temperature dependence of F_p at high field (12 T, Fig. 5.13 (b)) demonstrates an improving trend in F_p values towards 10 K, especially for YBCO – 8% BZO film.

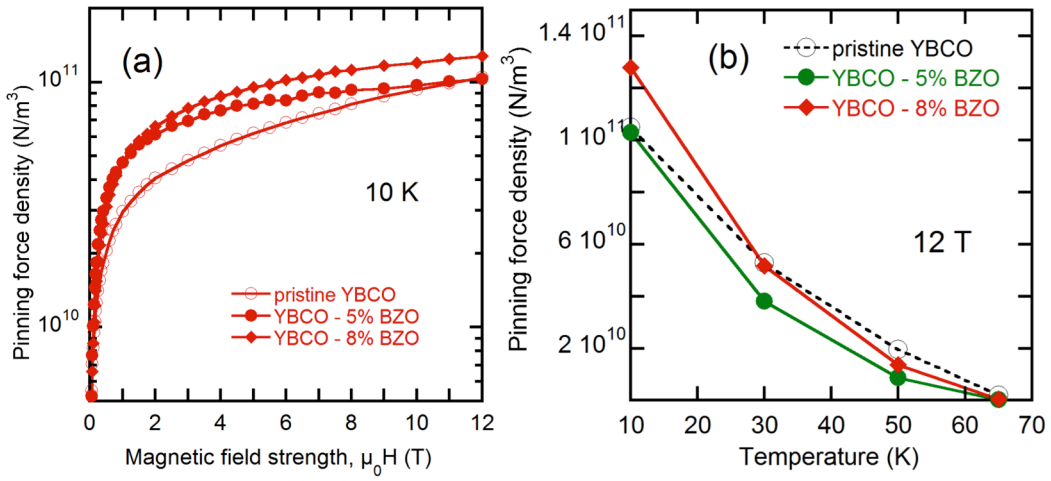

Fig. 5.13. The pinning force density as a function of (a) the magnetic field at 10 K and (b) the temperature at 12 Tfor pristine YBCO (open circles), YBCO – 5% BZO (full circles) and YBCO -8% BZO (full diamonds).

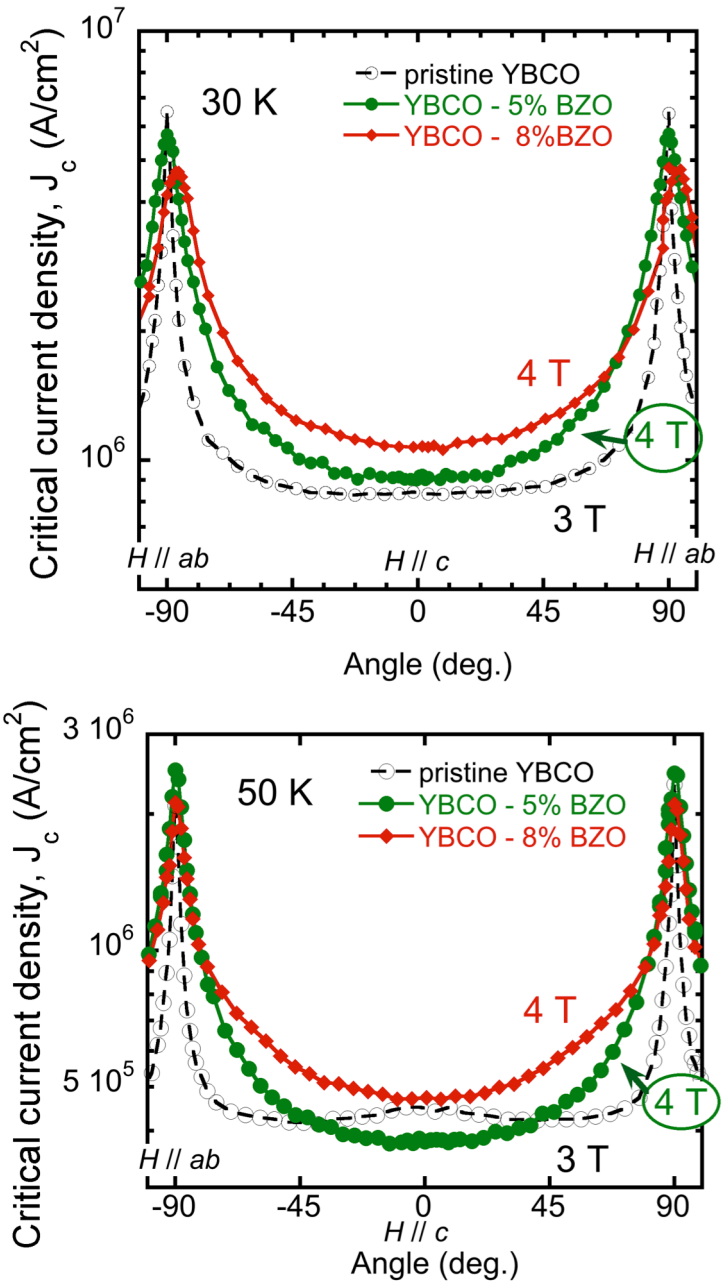

Fig. 5.14. Critical current density as a function of the applied field direction for the pristine YBCO (green symbols) and YBCO/BZO (red symbols) films.

The angular anisotropy of J_c is presented on Figure 5.14 at $T = 30$ K and $T = 50$ K. The YBCO – 8% BZO film has larger and more isotropic J_c with respect to the two other samples (since there is no data available for pristine YBCO at 4 T, the data presented here is at 3 T, certainly larger than at high T). In general case, these data would be higher than the data at 4 T because the values decreases with increasing the

magnetic field, but since BZO doped samples show stronger pinning properties, one can see the J_c (θ) curves of doped samples lay above pristine YBCO.

Thus, for power applications, demanding very strong vortex pinning capable to yield high values of J_c in high magnetic fields and low temperatures, MOD derived films with introduced APCs are the promising candidates.

5.3.2 Comparison of microwave properties

Since properties of YBCO – 5% BZO and YBCO – 8% BZO are very similar, the microwave analysis has been made for pristine YBCO and YBCO with 5% of doping.

The field dependence of the complex effective surface impedance for pure YBCO (a) and YBCO with BZO inclusions (b) is presented in Fig. 5.15. Lower ΔR values of YBCO/BZO film indicate the reduced dissipation in the vortex state with respect to the pure sample. This is reflected on the r parameter (Fig. 5.16, (a)). It indicates that the introduction of BZO increases the absolute value of the pinning parameter and drastically reduces the steepness of $r(H)$. Athrough there is appreciable similar vortex parameter $r \sim 1.25$ at low fields, $\mu_0 H$ = [0.01-0.1] T (Fig. 5.15), in the field range [0.1 - 0.8] T the effect of BZO nanoparticles clearly shows up [81], [103]. The results are consistent with higher J_c values (stronger pinning) for BZO doped samples measured by the DC electric method in the similar field range (0.1 - 1) T. Besides, the significant increase of r is achieved in comparison with published data [132] obtained in different MOD YBCO and YBCO/BZO samples, where $r \sim 0.6$ at 0.2 T for a YBCO-10%BZO sample, whereas for the YBCO/BZO in the present study $r \sim 1$ at 0.2 T. This is a direct demonstration of the improved sample preparation, with more efficient nanodefects.

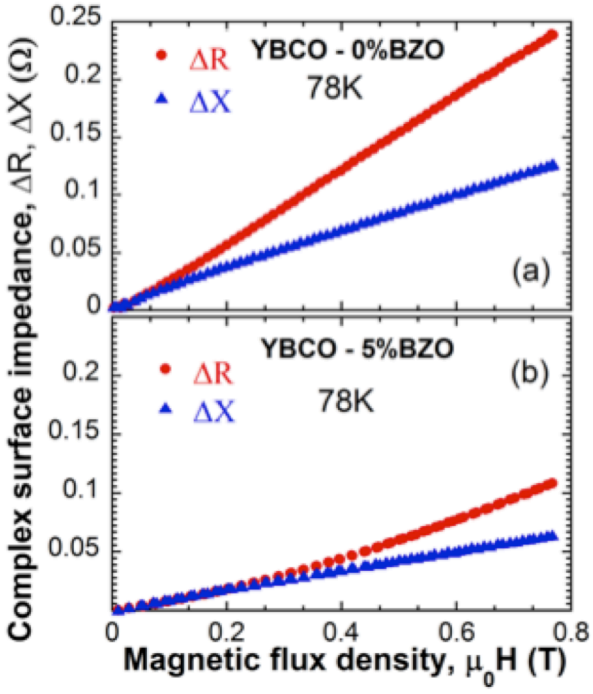

Fig. 5.15. Microwave data acquired on MOD derived samples at T=78 K. Field-induced change of the complex surface impedance in pristine YBCO (a) and in YBCO/BZO (b).

The field dependence of k_p for both samples is reported in Figure 5.16 (b). It can be seen that for both samples $k_p(H)$ is a decreasing function of the field, in striking contrast with what has been observed in PLD-grown YBCO/BZO samples [108], where $k_p(H)$ was almost constant in the same field range [0.1 - 0.8] T. The latter behaviour has been connected to the columnar organization of BZO in PLD samples. Therefore, the observation of a k_p decrease with the field in all MOD YBCO/BZO samples, as well as in pure YBCO, presumably indicates that BZO nano-inclusions do not produce columnar defects, or additional strong correlated pinning features, as occurs instead with $BaZrO_3$ nano-columns in PLD samples. The higher k_p values for MOD/BZO sample, studied in this thesis, can be explained by steeper pinning wells or by a higher density of pinning sites due to the introduction of BZO. But taking into account the J_c curves in the same field range [0 – 0.8] T, one can see that at low fields the pinning is weaker in the doped sample, and it gets stronger with the respect to the pure sample as the magnetic field increases. This is in favour of a larger amount of pinning sites, instead of stronger pins (stronger, steeper pins are expected

to cause high J_c values at low fields by effectively pinning each vortex). Based on these two observations, one can conclude that the increase of transport properties at the certain field range [0.1 – 1] T is likely to be due to the increased pinning sites density by the introduction of BZO nano-inclusions. Consistently, the similar field dependence of k_p in pristine YBCO and YBCO/BZO indicates that the pinning mechanisms did not change with the introduction of BZO.

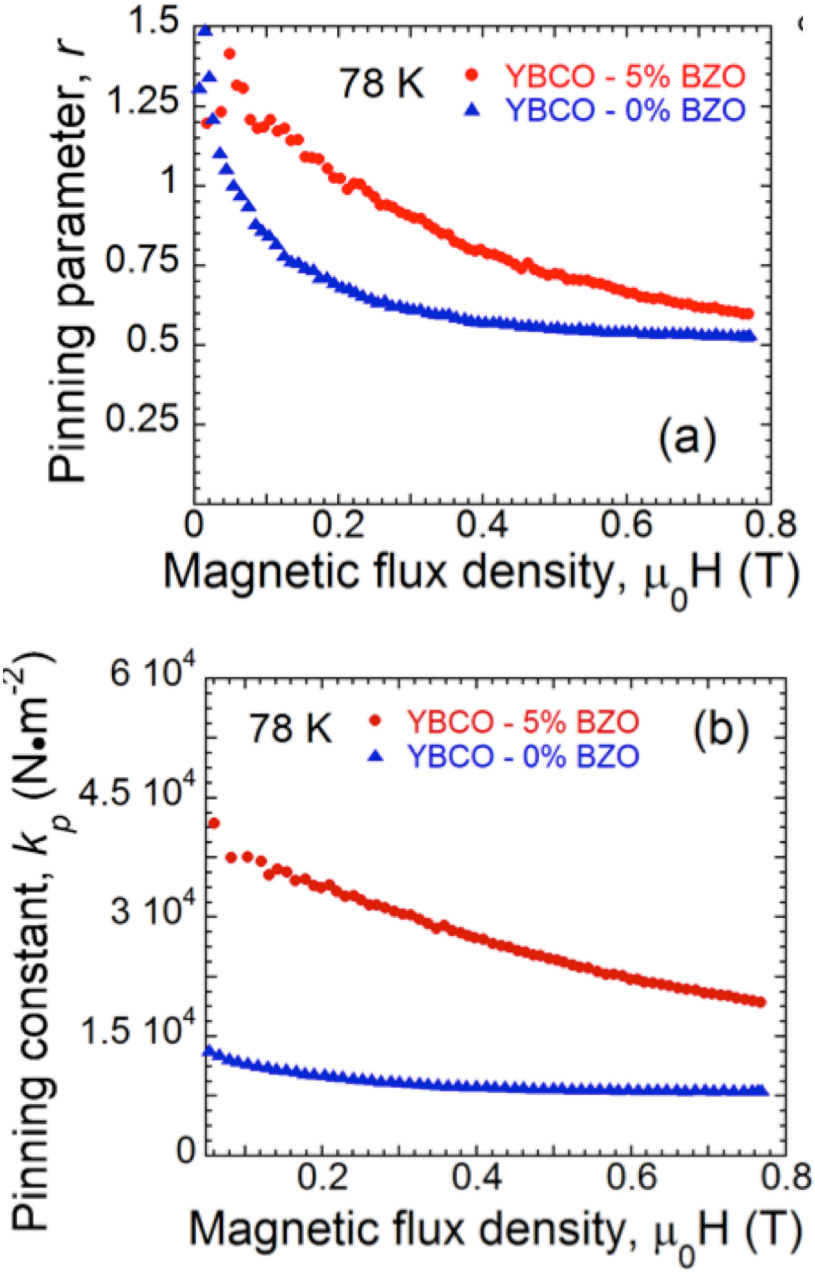

Fig. 5.16. Pinning parameter r (a) and pinning constant k_p (b) for pure (blue triangles) and YBCO/BZO (red circles) samples.

5.4 Experimental correlation between DC electric transport and microwave measurements

As was shown in this study, by exploiting the intrinsic processes responsible for the dissipation in superconducting thin films, the microwave measurement technique can act as a reliable, non-destructive and complimentary method to the DC electric measurements for quick HTS material characterization on laboratory-sized samples, but could also be applied to commercial coated conductors.

The combination of the microwave measurements with the standard DC transport measurements elucidates further the physics of vortex matter in YBCO as two techniques perform measurements in two different regimes (see Chapter 1): non linear regime with collective vortex-vortex interaction in DC measurements when the flux lines are depinned and dragged along relatively large distances, and linear regime of microwave measurements when a single vortex interacts with one or few pinning sites and the vortex displacement is small (less than 0.1 nm) at high microwave frequencies. Thus, the microwave measurements compared with the DC measurement results prove to gain insight into the nature of pinning induced by nano inclusions, as well as on the balance between material degradation and increased pinning, which would not be clear by using just one of these techniques.

To conclude the study and show the connection between the microwave measurements and the standard DC electric transport measurements, following [133] J_c and r were compared, since these parameters are directly measured and both represent intrinsic properties of the films. Measurements were taken at two temperatures T = 77 K and T = 65 K, as well as at two different magnetic fields, $\mu_0 H$ = 0.5 T and $\mu_0 H$ = 0.75 T, for all the samples in this study, i.e. YBCO thin films grown by two different techniques with different type and amount of doping. Figure 5.17 reports a plot of the pinning parameter vs. critical current density. It is evident that an experimental correlation exists between the microwave and the DC parameters. This fact is even more striking taking into account that the microwave measurements are performed firmly in the linear regime, while J_c is inherently a nonlinear property.

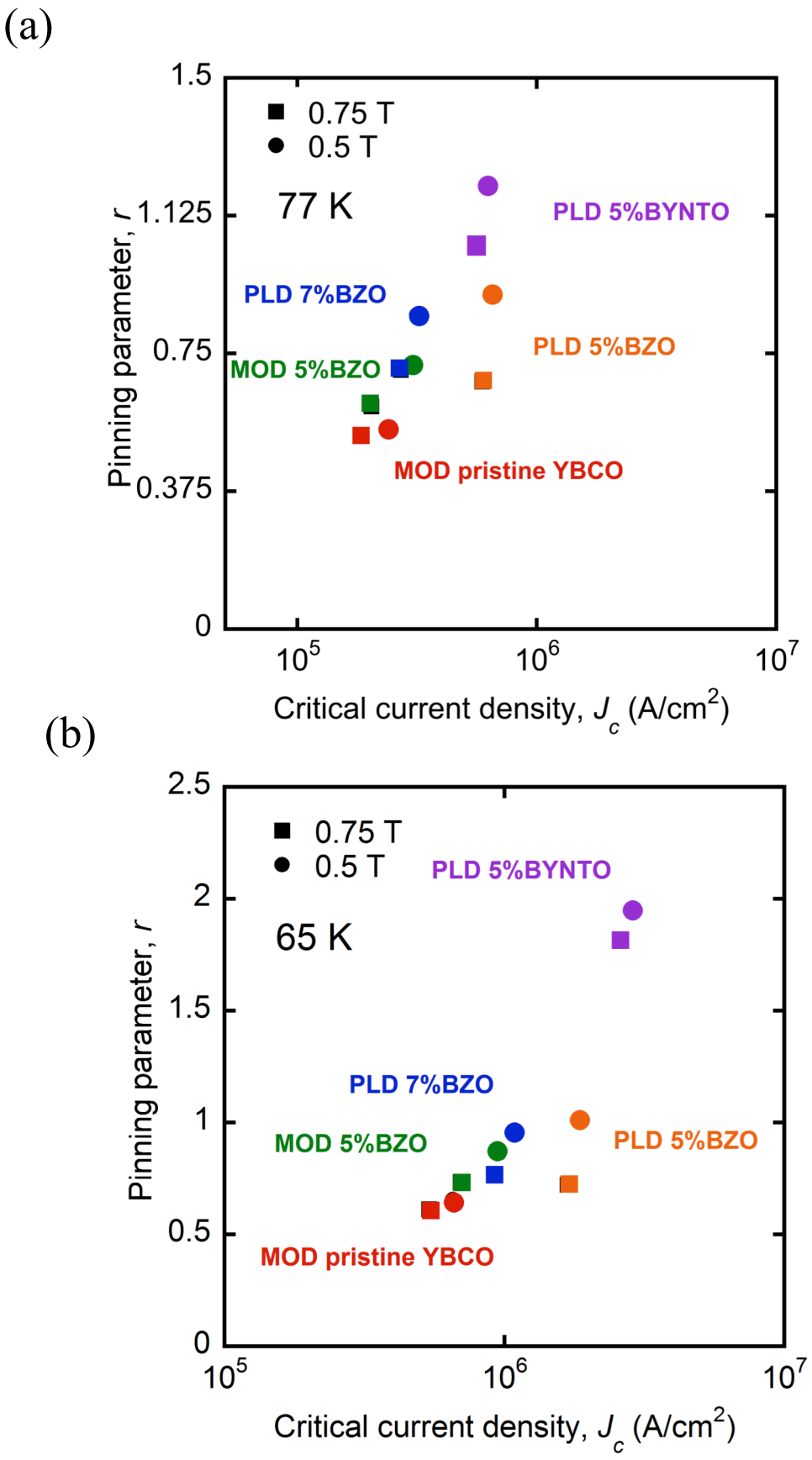

Fig. 5.17. The experimental correlation between the r parameter and the DC critical current density J_c, independently measured at (a) 77 K and (b) 65 K in different sample types. Note the different J_c and r scales for each plot.

The reason for the correlation resides in the common origin of both properties – vortex flux pinning. Nevertheless, fluxon dynamics is a complex field: a qualitative assessment of the properties of a superconducting material can be performed in the high-frequency microwave measurements, but the final evaluation on the finite assembly will require the DC electric transport measurements.

5.5 Summary

This Chapter discussed different aspects of vortex pinning in YBCO thin films. One of the aspects is the role of twin boundaries in the YBCO pristine sample grown by MOD technique and it was shown that twin boundaries can act as strong pinning centres, increasing the critical current, or vortex channels, increasing the dissipation instead. Based on the obtained results, a boundary between vortex pinning and vortex channeling for the pristine MOD YBCO sample was presented in a form of $H - T$ diagram. Another important observation was made: in the high magnetic field range, the effectiveness of extended defects is progressively reduced on lowering the temperature, suggesting that at low temperatures the dominant pinning contribution arises from isotropic pinning centres.

A second issue under study was the effect of different APCs in PLD films. The comparison of the PLD samples has shown that the combination of *c*-axis aligned BYNTO continuous columns and Y_2O_3 nanoparticles provides the strongest pinning source for vortices among all the samples. Additional information obtained from microwave measurements also proved that the most effective pinning is given by BYNTO columns.

Thirdly, an experimental analysis of the effects of different amount of doping in MOD derived films has shown that at high temperatures APCs are effective only at low magnetic fields, while at low temperatures APCs are acting as strong pinning sites also at high magnetic fields up to 12 T. Microwave analysis of these MOD samples revealed the similar field dependence of k_p in pristine YBCO and YBCO/BZO indicating that the pinning mechanisms did not change with the

introduction of BZO. However, the higher values of the pinning parameter and the pinning constant in the doped sample mean a more efficient pinning, presumably due to a large number of pinning sites arising from BZO nano-inclusions.

Finally, the experimental correlation between the microwave and the DC parameters has been presented among samples grown by different methods, with or without APCs at different temperatures and magnetic fields.

Conclusions

The aim of this thesis was a detailed experimental study of $YBa_2Cu_3O_{7-x}$ transport properties by combination of the two measurement techniques and vortex pinning investigation at the magnetic vortex regimes relevant for fusion applications of superconductors. The focus was on the understanding at a microscopic level of the vortex dynamics in different regimes in $YBa_2Cu_3O_{7-x}$ - the HTS material most promising for fusion application regimes. The measurements were performed at low temperatures (4 – 50 K) and high magnetic fields (up to 12 T). As the magnetic field specifications for future DEMOnstration Power Station (DEMO) lay at the range of 12-16 T [134], [135], one can possibly extrapolate to the higher magnetic fields the observed tendencies in structural and transport properties presented in this research. Further investigations are already ongoing at magnetic fields higher than 12 T, not only at the facility where the present study has been performed (now up to 18 T), but also on the international level worldwide.

The investigation of the vortex motion and pinning for the present study has been done by means of:

- *DC* resistivity $\rho\ (T)$, as a preliminary probe of sample quality (T_c);
- Critical current density $J_c\ (T, H, \vartheta)$ (strong nonlinear regime), to directly probe the performances of the studied samples;
- Microwave surface impedance $Z\ (H, T)$: at high-frequency (47 GHz), to probe the very-small-displacement vortex regime. The pinning parameters, the pinning parameter r and the pinning constant k_p, have been obtained.

Two methods have been used to grow the samples - Pulsed Laser Deposition (PLD) and Metal Organic Decomposition (MOD) techniques. The first technique has

proven to be a method of choice in the fabrication of very high quality high-T_c thin films, as the stoichiometric transfer of material from target to the film gives a precise control. The second method, MOD, has become one of the most promising alternatives towards successful development of long length YBCO coated conductors.

The structural analysis of the samples revealed that secondary phases, such as $BaZrO_3$ (BZO) and $Ba_2Y(Nb/Ta)O_6$ (BYNTO), were successfully introduced in YBCO films. Such nanoscale inclusions produced columnar defects or isotropic nanoparticles, in PLD and MOD films, respectively.

An extensive electrical characterisation of all the samples was performed by the DC current transport measurement technique to obtain the critical current density J_c. The effect of different APCs in the PLD films and the effects of different concentration of APCs in the MOD films have been reported. The comparison of the PLD samples with different second phases has shown that the combination of *c*-axis aligned BYNTO continuous columns provides the strongest pinning source for vortices among all the samples. The analysis of different amount of BZO doping in the MOD derived films has shown that at low temperatures the introduced nanoparticles act as strong pinning sites also at high magnetic fields up to 12 T, and that the pinning improves with increasing BZO content.

The analysis of anisotropy in the pristine MOD sample revealed a directional effect of twin boundaries on pinning. The boundary between vortex pinning and vortex channeling regimes in the $H-T$ diagram was identified. Interestingly, the introduction of BZO nanoparticles in MOD films removed any fingerprints of channeling or anisotropic pinning. This effect was accompanied by the enhancement of J_c in a wide angular range in comparison with the pristine sample. These features indicate a change in the pinning mechanism, beneficial towards the material optimization for power performances.

A clear correlated pinning contribution from APCs is observed in both PLD derived samples when the field is parallel to the BZO and BYNTO nanocolumns ($\theta = 0^{\circ}$). Nevertheless, the combination of *c*-axis aligned BYNTO continuous

columns provide stronger pinning source for vortices, which barely depends on the field: a strong peak in J_c (with H // c-axis) was observed even at high fields. That results in the J_c improvement in a wider angular range in comparison with YBCO/BZO.

High-frequency microwave measurements were consistent with DC results: the pinning parameter r quantitatively confirms the strong pinning in the PLD doped samples with respect to the pristine film. YBCO/BYNTO demonstrated an increase of the pinning constant k_p. It emerges that the pinning wells in YBCO/BYNTO keep their steepness more efficiently, particularly at fields larger than in YBCO/BZO.

Analysis of the DC obtained data for MOD films revealed that at high temperatures BZO nanoparticles are effective only at low magnetic fields, while at low temperatures BZO act as strong pinning sites also at high magnetic fields up to 12 T. That suggests that at low temperatures the dominant pinning contribution arises from isotropic pinning centres, which are the BZO nano-inclusions in the present MOD YBCO films. This is a positive result in terms of high power applications, which are expected to work at low temperature and at high magnetic fields. The lower values of complex surface impedance in MOD YBCO/BZO film indicate the reduced dissipation in the vortex state with respect to the pristine sample. This is quantified by the r parameter: the introduction of BZO nanoparticles increases the absolute value of the pinning parameter and drastically reduces the steepness of $r(H)$. The observation of the k_p decrease with the field in MOD YBCO/BZO sample presumably indicates that BZO nano-inclusions do not produce additional strong correlated pinning features, as occurs with BZO and BYNTO nano-columns in PLD samples. Instead, higher k_p values for MOD/BZO sample are due to the increased density of pinning sites. This is a striking difference between PLD and MOD samples, elucidated by the combination of the different transport measurement techniques.

Finally, the experimental correlation between the microwave and the DC parameters has been presented among all the studied samples grown by different methods, with or without APCs at different temperatures and magnetic fields.

The microwave measurement technique is a complementary non-destructive method for the vortex pinning investigation and for a complete characterisation of the in-field performance and of the role of the structural defects in the superconducting films. When a fusion-relevant neutron source for material testing, such as International Fusion Materials Irradiation Facility (IFMIF) will be available, the microwave technique could be a potential characterisation method of the HTS films before and after neutron irradiation to test material performance modifications under operative conditions.

The knowledge acquired during this 3 year long PhD course will constitute a background for the assessment of the potential in performance improvements of YBCO coated conductors, as a reference for the design of the HTS based magnet system for a fusion reactor.

The information contained within this thesis has contributed to several publications and the advancement of the research project within the framework of the EUROfusion Consortium.

Bibliography

[1] H. Kamerlingh Onnes, “Further Experiments with liquid Helium,” *Leiden Commun.*, vol. 120b, 122b, pp. 261–271, 1911.

[2] C. Senatore, “High Temperature Superconductors: The path from materials to technical conductors,” *Eur. Conf. Appl. Supercond. EUCAS 2017, Geneva, Swizterl.*, 2017.

[3] J. G. Bednorz and K. a. Muller, “Possible High Tc Superconductivity in the Ba - La - Cu - O System,” *Zeitschrift für Phys. B Condens. Matter*, vol. 64, pp. 189–193, 1986.

[4] M. Tinkham, “Introduction to Superconductivity,” *McGraw-Hill, Inc.*, 1996.

[5] R. D. Parks, Ed., *Superconductivity*. Marcel Dekker, Inc., 1969.

[6] L. N. Cooper, “Bound electron pairs in a degenerate Fermi gas,” *Phys. Rev.*, vol. 104, no. 4, pp. 1189–1190, 1956.

[7] M. Cyrot, “Ginzburg-Landau theory for superconductors,” *Reports Prog. Phys.*, vol. 36, 1973.

[8] A. A. Abrikosov, *Fundamentals of the theory of metals*. North Holland, 1988.

[9] G. Blatter, M. V. Feigel’Man, V. B. Geshkenbein, A. I. Larkin, and V. M. Vinokur, “Vortices in high-temperature superconductors,” *Rev. Mod. Phys.*, vol. 66, no. 4, pp. 1125–1388, 1994.

[10] F. Bouquet *et al.*, “An unusual phase transition to a second liquid vortex phase in the superconductor $YBa_2Cu_3O_{7.}$,” *Nature*, vol. 411, pp. 448–451, 2001.

[11] M. P. A. Fisher, “Vortex-glass superconductivity: A possible new phase in bulk high-Tc oxides,” *Phys. Rev. Lett.*, vol. 62, no. 12, pp. 1415–1418, 1989.

[12] D. S. Fisher, M. P. A. Fisher, and D. A. Huse, “Thermal Quctuations, quenched disorder, phase transitions, and transport in type-II superconductors,” *Phys. Rev. B*, vol. 43, no. 1, pp. 130–159, 1991.

[13] D. R. Nelson and V. M. Vinokur, “Boson localization and pinning by correlated disorder in high-temperature superconductors,” *Phys. Rev. Lett.*, vol. 68, no. 15, pp. 2398–2401, 1992.

[14] D. R. Nelson and V. M. Vinokur, “Boson localization and correlated pinning of superconducting vortex arrays,” *Phys. Rev. B*, vol. 48, no. 17, pp. 13060–13097, 1993.

[15] G. Blatter, V. B. Geshkenbein, and A. I. Larkin, “From isotropic to anisotropic superconductors: A scaling approach,” *Phys. Rev. Lett.*, vol. 68, no. 6, pp. 875–878, 1992.

[16] J. Bardeen and M. J. Stephen, “Theory of the motion of vortices in superconductors,” *Phys. Rev.*, vol. 140, no. 4A, p. A 1197-A 1207, 1965.

[17] M. Golosovsky, M. Tsindlekht, and D. Davidov, “High-frequency vortex dynamics in $YBa_2Cu_3O_7$,” *Supercond. Sci. Technol.*, vol. 9, pp. 1–15, 1996.

[18] C. Caroli, P. G. De Gennes, and J. Matricon, “Bound Fermion states on a vortex line in a type II superconductor,” *Phys. Lett.*, vol. 9, no. 4, pp. 307–309, 1964.

[19] J. M. Harris, Y. F. Yan, O. K. C. Tsui, Y. Matsuda, and N. P. Ong, “Hall Angle Evidence for the Superclean Regime in 60 K $YBa_2Cu_3O_{6+y}$,” *Phys. Rev. Lett.*, vol. 73, no. 12, pp. 1711–1714, 1994.

[20] P. W. Anderson and Y. B. Kim, “Hard superconductivity: Theory of the motion of abrikosov flux lines,” *Rev. Mod. Phys.*, vol. 36, no. 1, pp. 39–43, 1964.

[21] D. Dew-Hughes, “The critical current of superconductors: An historical review,” *Low Temp. Phys.*, vol. 27, no. 9–10, pp. 967–979, 2001.

[22] Robert E. Collin, *Foundations for Microwave Engineering, 2nd Edition*, vol. 13, no. 1. John Wiley & Sons, Inc., 2000.

[23] R. Marcon, R. Fastampa, M. Giura, and E. Silva, “Vortex-motion dissipation in high-T_c superconductors at microwave frequencies,” *Phys. Rev. B*, vol. 43, no. 4, pp. 2940–2945, 1991.

[24] M. W. Coffey and J. R. Clem, “Unified theory of effects of vortex pinning and flux creep upon the rf surface impedance of type-II superconductors,” *Phys. Rev. Lett.*, vol. 67, no. 3, pp. 386–389, 1991.

[25] K. W. Blazey, A. M. Portis, K. A. Muller, and F. H. Holtzberg, “Macroscopic FIux Quantization and Microwave Excitation in Single-Crystal $YBa_2Cu_3O_{7-\delta}$,” *Europhys. Lett.*, vol. 6, no. 5, pp. 457–462, 1988.

[26] J. I. Gittleman and B. Rosenblum, “The pinning potential and high-frequency studies of type-II superconductors,” *J. Appl. Phys.*, vol. 39, no. 6, pp. 2617–2621, 1968.

[27] V. Breit *et al.*, “Evidence for chain superconductivity in near-stoichiometric $YBa_2Cu_3O_x$ single crystals,” *Phys. Rev. B*, vol. 52, no. 22, pp. 727–730, 1995.

[28] S. R. Foltyn *et al.*, “Materials science challenges for high-temperature superconducting wire.,” *Nat. Mater.*, vol. 6, pp. 631–642, 2007.

[29] X. Obradors and T. Puig, “Coated conductors for power applications: materials challenges,” *Supercond. Sci. Technol.*, vol. 27, no. 4, p. 44003, Apr. 2014.

[30] L. Civale, “Vortex pinning and creep in high-temperature superconductors with columnar defects,” *Supercond. Sci. Technol.*, vol. 10, pp. A11–A28, 1997.

[31] J. L. MacManus-Driscoll *et al.*, "Strongly enhanced current densities in superconducting coated conductors of $YBa_2Cu_3O_{7-x}$ + $BaZrO_3$," *Nat. Mater.*, 2004.

[32] A. Goyal *et al.*, "Irradiation-free, columnar defects comprised of self-assembled nanodots and nanorods resulting in strongly enhanced flux-pinning in $YBa_2Cu_3O_{7-\delta}$ films," *Supercond. Sci. Technol.*, vol. 18, no. 11, pp. 1533–1538, 2005.

[33] P. Mele *et al.*, "Ultra-high flux pinning properties of $BaMO_3$-doped $YBa_2Cu_3O_{7-x}$ thin films (M = Zr, Sn)," *Supercond. Sci. Technol.*, vol. 21, no. 3, p. 32002, 2008.

[34] A. Augieri *et al.*, "Pinning analyses on epitaxial $YBa_2Cu_3O_{7-\delta}$ films films with $BaZrO_3$ inclusions," *J. Appl. Phys.*, vol. 108, pp. 1–5, 2010.

[35] G. Blatter, J. Rhyner, and V. M. Vinokur, "Vortex pinning by twin boundaries in copper oxide superconductors," *Phys. Rev. B*, vol. 43, no. 10, pp. 7826–7830, 1991.

[36] V. Rouco *et al.*, "Role of twin boundaries on vortex pinning of CSD YBCO nanocomposites," *Supercond. Sci. Technol.*, no. 27, 2014.

[37] J. Gazquez, M. Coll, N. Roma, F. Sandiumenge, T. Puig, and X. Obradors, "Structural defects in trifluoroacetate derived $YBa_2Cu_3O_7$ thin films," *Supercond. Sci. Technol.*, vol. 25, no. 6, p. 65009, 2012.

[38] A. Palau, T. Puig, J. Gutierrez, X. Obradors, and F. de la Cruz, "Pinning regimes of grain boundary vortices in $YBa_2Cu_3O_{7-x}$ coated conductors," *Phys. Rev. B*, vol. 73, p. Art. no. 132508, 2006.

[39] A. Diaz, L. Mechin, P. Berghuis, and J. E. Evetts, "Evidence for Vortex Pinning by Dislocations in $YBa_2Cu_3O_{7-\delta}$ Low-Angle Grain Boundaries," *Phys. Rev. Lett.*, vol. 80, no. 17, pp. 3855–3858, 1998.

[40] V. F. Solovyov *et al.*, "High critical currents by isotropic magnetic-flux-pinning centres in a 3 μm-thick $YBa_2Cu_3O_7$ superconducting coated conductor," *Supercond. Sci. Technol.*, vol. 20, pp. L20–L23, 2007.

[41] P. Mele *et al.*, "Insertion of nanoparticulate artificial pinning centres in $YBa_2Cu_3O_{7-x}$ films by laser ablation of a Y_2O_3-surface modified target," *Supercond. Sci. Technol.*, vol. 20, pp. 616–620, 2007.

[42] P. Mele, R. Guzman, J. Gazquez, and T. Puig, "High pinning performance of $YBa_2Cu_3O_{7-x}$ films added with Y_2O_3 nanoparticulate defects," *Supercond. Sci. Technol.*, vol. 28, no. 2, p. 24002, 2015.

[43] C. Senatore, C. Barth, M. Bonura, M. Kulich, and G. Mondonico, "Field and temperature scaling of the critical current density in commercial REBCO coated conductors," *Supercond. Sci. Technol.*, vol. 29, no. 1, p. 14002, 2016.

[44] J. M. Rey *et al.*, "HTS dipole insert developments," *IEEE Trans. Appl. Supercond.*, vol. 23, p. Art. no. 4601004, 2013.

[45] W. D. Markiewicz *et al.*, "Progress in the Development of a Superconducting 32 T Magnet With REBCO High Field Coils," *IEEE Trans. Appl. Supercond.*, vol. 22, no. 3, p. Art. no. 4300704, 2012.

[46] C. Senatore, M. Alessandrini, A. Lucarelli, R. Tediosi, D. Uglietti, and Y. Iwasa, "Progresses and challenges in the development of high-field solenoidal magnets based on RE123 coated conductors," *Supercond. Sci. Technol.*, vol. 27, no. 10, p. 103001, 2014.

[47] S. Miura *et al.*, "Strongly enhanced irreversibility field and flux pinning force density in $SmBa_2Cu_3O_y$ coated conductors with well-aligned $BaHfO_3$ nanorods," *Appl. Phys. Express*, vol. 10, p. Art. no. 103101, 2017.

[48] D. Uglietti, N. Bykovsky, K. Sedlak, B. Stepanov, R. Wesche, and P. Bruzzone, "Test of 60kA coated conductor cable prototypes for fusion magnets," *Supercond. Sci. Technol.*, vol. 28, p. Art. no. 124005, 2015.

[49] J. Knaster, A. Moeslang and T. Muroga, "Materials research for fusion," *Nat. Phys.*, vol.12, pp. 424-434, 2016.

[50] P. Garin et al., "IFMIF specifications from the users point of view", *Fusion Eng. Des.,* vol. 86, pp. 611–614, 2011.

[51] M. Chudy, R. Fuger, M. Eisterer, and H. W. Weber, "Characterization of Commercial YBCO Coated Conductors After Neutron Irradiation," *IEEE Trans. Appl. Supercond*, vol. 21, no. 3, pp. 3162-3165, 2011.

[52] H. Weber, "Radiation effects on superconducting fusion magnet components", *Int. J. Mod. Phys. E*, vol. 20, no. 6, pp. 1325–1378, 2011

[53] F. M. Sauerzopf, et al., "Fast neutron irradiation and flux pinning in single crystalline high temperature superconductors," *Cryogenics*, vol. 33, no. 1, pp. 8-13, 1993.

[54] H. W.Weber, H. P.Wiesinger, W. Kritscha, and F. M. Sauerzopf, "Critical currents in neutron irradiated YBCO and BiSCCO single crystals," *Supercond. Sci. Technol.*, vol. 4, pp. 103–105, 1991.

[55] M. Okada and T. Kawakubo, "Effects of neutron irradiation on superconducting properties of orthorhombic Y–Ba–Cu oxides", *Radiat. Eff. Defects Solids*, vol. 108, pp. 137–144, 1989.

[56] H. Kupfer, et al., "Critical current and relaxation of oriented grained $YBa_2Cu_3O_{7-x}$ after fast neutron irradiation," *IEEE Trans. Magn.*, vol. 27, no. 2, pp. 1369 – 1374, 1991

[57] T. Aoki et al., "Effect of Neutron Irradiation on High-Temperature Superconductors," *IEEE Trans. Appl. Supercond*, vol. 21, no. 3, pp. 3200-3202, 2011.

[58] J. M. Phillips, "Substrate selection for high-temperature superconducting thin films," *J. Appl. Phys.*, vol. 79, no. 4, pp. 1829–1848, 1996.

[59] G. A. Farnan, M. P. Mccurry, C. C. Smith, R. J. Turner, and D. G. Walmsley, "Growth of $YBa_2Cu_3O_{7-\delta}$ thin films in pulsed laser deposition : influence of target, substrate and deposition rate," *Supercond. Sci. Technol.*, vol. 13, no. 25, pp. 262–272, 2000.

[60] R. K. Singh and J. Narayan, "Pulsed-laser evaporation technique for deposition of thin films: Physics and theoretical model," *Phys. Rev. B*, vol. 41, no. 13, pp. 8843–8859, 1990.

[61] J. M. Lackner *et al.*, "Pulsed laser deposition : a new technique for deposition of amorphous SiOx thin films," *Surf. Coatings Technol.*, vol. 163–164, pp. 300–305, 2003.

[62] G. Ercolano *et al.*, "State-of-the-art flux pinning in YBa2Cu3O7 − δ by the creation of highly linear , segmented nanorods of Ba2(Y/ Gd)(Nb/Ta)O6 together with nanoparticles of (Y/Gd)2O3 and (Y/Gd)Ba2Cu4O8," *Supercond. Sci. Technol.*, vol. 24, p. 95012, 2011.

[63] M. Malmivirta *et al.*, "The Angular Dependence of the Critical Current of $BaCeO_3$ Doped $YBa_2Cu_3O_{6+x}$ Thin Films," *IEEE Trans. Appl. Supercond.,* vol. 25, no. 3, pp. 3–7, 2015.

[64] M. Sieger *et al.*, "Tailoring microstructure and superconducting properties in thick $BaHfO_3$ and $Ba_2Y(Nb/Ta)O_6$ doped YBCO films on technical templates," *IEEE Trans. Appl. Supercond.*, vol. 27, no. 4, p. 6601407, 2017.

[65] H. M. Christen and G. Eres, "Recent advances in pulsed-laser deposition of complex oxides," *J. Phys. Condens. Matter*, vol. 20, no. 26, p. 264005, 2008.

[66] A. Crisan, V. S. Dang, and P. Mikheenko, "Nano-engineered pinning centres in YBCO superconducting films," *Phys. C Supercond. its Appl.*, vol. 533, pp. 118–132, 2017.

[67] V. Galluzzi *et al.*, "$YBa_2Cu_3O_{7-\delta}$ Films With $BaZrO_3$ Inclusions for Strong-Pinning in Superconducting Films on Single Crystal Substrate," *IEEE Trans.*

Appl. Supercond., vol. 17, no. 2, pp. 3628–3631, 2007.

[68] L. Opherden *et al.*, "Large pinning forces and matching effects in $YBa_2Cu_3O_{7-\delta}$ thin films with $Ba_2Y(Nb/Ta)O_6$ nano-precipitates," *Sci. Rep.*, vol. 6, no. 1, p. 21188, 2016.

[69] X. Obradors *et al.*, "Growth, nanostructure and vortex pinning in superconducting $YBa_2Cu_3O_7$ thin films based on trifluoroacetate solutions," *Supercond. Sci. Technol.*, vol. 25, no. 12, p. 123001, 2012.

[70] A. Gupta, R. Jagannathan, E. I. Cooper, E. A. Giess, J. I. Landman, and B. W. Hussey, "Superconducting oxide films with high transition temperature prepared from metal trifluoroacetate precursors," *Appl. Phys. Lett.*, vol. 52, no. 24, pp. 2077–2079, 1988.

[71] J. Farjas, J. Camps, P. Roura, S. Ricart, T. Puig, and X. Obradors, "Thermal decomposition of barium trifluoroacetate thin films," *Thermochim. Acta*, vol. 544, pp. 77–83, 2012.

[72] T. Araki and I. Hirabayashi, "Review of a chemical approach to $YBa_2Cu_3O_{7-x}$ coated supercondcutors- metalorganic deposition using trifluoroacetates," *Supercond. Sci. Technol*, vol. 16, pp. R71–R94, 2003.

[73] A. A. Armenio *et al.*, "Characterization of epitaxial $YBa_2Cu_3O_{7-\delta}$ films deposited by metal propionate precursor solution," *Supercond. Sci. Technol.*, vol. 21, p. 125015, 2008.

[74] L. H. Jin *et al.*, "Optimization of fluorine content in TFA-MOD precursor solutions for YBCO film growth," *Supercond. Sci. Technol.*, vol. 29, no. 1, p. Art. no. 15001, 2016.

[75] W. Bian *et al.*, "Effect of F/Ba ratio of precursor solution on the properties of solution-processed YBCO superconducting films," *Ceram. Int.*, vol. 43, no. 11, pp. 8433–8439, 2017.

[76] V. Pinto *et al.*, "Aging of Precursor Solutions Used for YBCO Films Chemical

Solution Deposition : Study of Mechanisms and Effects on Film Properties," *IEEE Trans. Appl. Supercond.*, vol. 26, no. 3, p. 7500405, 2016.

[77] A. A. Armenio *et al.*, "Deposition and Characterization of Metal Propionate Derived Epitaxial $YBa_2Cu_3O_{7-x}$ Films for Coated Conductor Fabrication," *IEEE Trans. Appl. Supercond.*, vol. 19, no. 3, pp. 3204–3207, 2009.

[78] A. A. Armenio *et al.*, "Structural and chemical evolution of propionate based metal – organic precursors for superconducting $YBa_2Cu_3O_{7-\delta}$ epitaxial film growth," *Supercond. Sci. Technol.*, vol. 24, p. 115008, 2011.

[79] A. A. Armenio *et al.*, "Analysis of the Growth Process and Pinning Mechanism of Low-Fluorine MOD $YBa_2Cu_3O_{7-\delta}$ Films With and Without $BaZrO_3$ Artificial Pinning Centers," *IEEE Trans. Appl. Supercond.*, vol. 25, no. 3, p. 6605205, 2015.

[80] S. H. Wee, Y. L. Zuev, C. Cantoni, and A. Goyal, "Engineering nanocolumnar defect configurations for optimized vortex pinning in high temperature superconducting nanocomposite wires," *Nat. Sci. reports*, vol. 3, p. 2310, 2013.

[81] E. Silva *et al.*, "Measurement of vortex parameters and pinning in $YBa_2Cu_3O_{7-x}$ with $BaZrO_3$ nanoinclusions," *IEEE Trans. Appl. Supercond.*, vol. 25, no. 3, p. Art. no. 6601205, 2015.

[82] A. Palau *et al.*, "Crossover between Channeling and Pinning at Twin Boundaries in $YBa_2Cu_3O_7$ Thin Films," *Phys. Rev. Lett.*, vol. 97, p. 257002, 2006.

[83] M. Miura *et al.*, "Mixed pinning landscape in nanoparticle-introduced $YGdBa_2Cu_3O_y$ films grown by metal organic deposition," *Phys. Rev. B*, vol. 83, p. 184519, 2011.

[84] T. Petrisor Jr *et al.*, "The Vortex Path Model Analysis of the Field Angle Dependence of the Critical Current Density in Nanocomposite $YBa_2Cu_3O_{7-x}$ – $BaZrO_3$ Films Obtained by Low Fluorine Chemical Solution Deposition," *J.*

Supercond. Nov. Magn., vol. 27, pp. 2493–2500, 2014.

[85] J. Gazquez, M. Coll, N. Roma, F. Sandiumenge, T. Puig, and X. Obradors, "Structural defects in trifluoroacetate derived $YBaCu_3O_7$ thin films," *Supercond. Sci. Technol.*, vol. 25, p. 65009, 2012.

[86] M. Miura, M. Yoshizumi, T. Izumi, and Y. Shiohara, "Formation mechanism of $BaZrO_3$ nanoparticles in $Y_{1-x}Sm_xBa_2Cu_3O_y$ -coated conductors derived from trifluoroacetate metal – organic deposition," *Supercond. Sci. Technol.*, vol. 23, p. 14013, 2010.

[87] P. Paturi, M. Irjala, H. Huhtinen, and A. B. Abrahamsen, "Modeling flux pinning in thin undoped and $BaZrO_3$ -doped YBCO films," *J. Appl. Phys.*, vol. 105, p. 23904, 2009.

[88] S. R. Foltyn, L. Civale, Q. X. Jia, B. Maiorov, H. Wang, and M. Maley, "Materials science challenges for high-temperature superconducting wire," *Nat. Mater.,* pp. 631–642, 2007.

[89] A. Gurevich and L. D. Cooley, "Anisotropic flux pinning in a network of planar defects," *Phys. Rev. B*, vol. 50, no. 18, p. 13 563-13 576, 1994.

[90] L. A. Dorosinskii, V. I. Nikitenko, A. A. Polyanskii, and V. K. Vlasko-Vlasov, "Influence of twins on the critical current in YBaCuO single crystals," *Phys. C Supercond. its Appl.*, vol. 219, no. 1–2, pp. 81–86, 1994.

[91] J. Gutierrez *et al.*, "Strong isotropic flux pinning in nanocomposite superconductor films," *Nat. Mater.*, vol. 6, no. 200, pp. 367–373, 2007.

[92] A. Augieri *et al.*, "Transport Property Improvement by Means of BZO Inclusions in PLD Grown YBCO Thin Films," vol. 19, no. 3, pp. 3399–3402, 2009.

[93] J. Z. Wu *et al.*, "The effect of lattice strain on the diameter of $BaZrO_3$ nanorods in epitaxial $YBa_2Cu_3O_{7-\delta}$ films," *Supercond. Sci. Technol.*, vol. 27, no. 4, p. 44010, 2014.

[94] R. Willa, A. E. Koshelev, I. A. Sadovskyy, and A. Glatz, “Strong pinning regimes by spherical inclusions in anisotropic type-II superconductors,” *arXiv:1708.01653 [cond-mat.supr-con]*, pp. 1–21, 2017.

[95] M. Peurla *et al.*, “Effects of nanocrystalline target and columnar defects on flux pinning in pure and $BaZrO_3$ -doped $YBa_2Cu_3O_{6+x}$ films in fields up to 30 T,” *Phys. Rev. B - Condens. Matter Mater. Phys.*, vol. 75, no. 18, pp. 2–7, 2007.

[96] S. Kang *et al.*, “Flux-pinning characteristics as a function of density of columnar defects comprised of self-assembled nanodots and nanorods in epitaxial $YBa_2Cu_3O_{7-\delta}$ films for coated conductor applications,” *Phys. C*, vol. 457, pp. 41–46, 2007.

[97] S. H. Wee, Y. Zuev, C. Cantoni, and A. Goyal, “Engineering nanocolumnar defect configurations for optimized vortex pinning in high temperature superconducting nanocomposite wires,” *Sci. Rep.*, vol. 3, p. 2310, 2013.

[98] L. Civale *et al.*, “Angular-dependent vortex pinning mechanisms in $YBa_2Cu_3O_7$ coated conductors and thin films,” *Appl. Phys. Lett.*, vol. 84, no. 12, pp. 2121–2123, 2004.

[99] T. Petrisor *et al.*, “The Vortex Path Model Analysis of the Field Angle Dependence of the Critical Current Density in Nanocomposite $YBa_2Cu_3O_{7-x}$ – $BaZrO_3$ Films Obtained by Low Fluorine Chemical Solution Deposition,” *J. Supercond. Nov. Magn.*, vol. 27, no. 11, pp. 2493–2500, 2014.

[100] V. F. Solovyov *et al.*, “High critical currents by isotropic magnetic-flux-pinning centres in a 3 μm-thick $YBa_2Cu_3O_7$ superconducting coated conductor,” *Supercond. Sci. Technol.*, vol. 20, no. 4, pp. L20–L23, 2007.

[101] N. Pompeo, A. Augieri, K. Torokhtii, V. Galluzzi, G. Celentano, and E. Silva, “Anisotropy and directional pinning in $YBa_2Cu_3O_{7-x}$ with $BaZrO_3$ nanorods,” *Appl. Phys. Lett.*, vol. 103, p. Art. no. 22603, 2013.

[102] N. Pompeo, R. Rogai, E. Silva, A. Augieri, V. Galluzzi, and G. Celentano,

"Strong reduction of field-dependent microwave surface resistance in $YBa_2Cu_3O_{7-x}$ with submicrometric $BaZrO_3$ inclusions," *Appl. Phys. Lett.*, vol. 91, p. Art. no. 182507, 2007.

[103] K. Torokhtii *et al.*, "Measurement of Vortex Pinning in YBCO and YBCO / BZO Coated Conductors Using a Microwave Technique," *IEEE Trans. Appl. Supercond. Trans. Appl. Supercond.*, vol. 26, no. 3, p. 8001605, 2016.

[104] N. Pompeo, K. Torokhtii, E. Silva, D. Ingegneria, U. R. Tre, and V. Navale, "Dielectric Resonators for the Measurements of the Surface Impedance of Superconducting Films," *Meas. Sci. Rev.*, vol. 14, no. 3, pp. 164–170, 2014.

[105] D. Kajfez and P. Guillon, "Dielectric Resonators," *SciTech Publ.*, 1998.

[106] M. Hein, "High-temperature-superconductor thin films at microwave frequencies (Springer Tracts in Modern Physics)," *Springer-Verlag Berlin Heidelb.*, 1999.

[107] N. Pompeo, L. Muzzi, V. Galluzzi, R. Marcon, and E. Silva, "Measurements and removal of substrate effects on the microwave surface impedance of YBCO films on $SrTiO_3$," *Supercond. Sci. Technol.*, vol. 20, pp. 1002–1008, 2007.

[108] N. Pompeo, R. Rogai, A. Augieri, V. Galluzzi, G. Celentano, and E. Silva, "Reduction of the field-dependent microwave surface resistance in $YBa_2Cu_3O_{7-\delta}$ with sub-micrometric $BaZrO_3$ inclusions as a function of $BaZrO_3$ concentration," *J. Appl. Phys.*, vol. 105, p. Art. no. 13927, 2009.

[109] E. Silva, N. Pompeo, and K. Torokhtii, "Microwave measurements to assess the properties of superconducting materials for applications .," Proceedings of the 20th IMEKO TC-4 International Symposium 18th International Workshop on ADC Modelling and Testing Research on Electric and Electronic Measurement for the Economic Upturn, Benevento, Italy, 15-17 Sept., 2014, ISBN-14: 978-92-990073-2-7.

[110] K. Torokhtii *et al.*, “Microwave Measurements of Pinning Properties in Chemically Deposited YBCO / BZO Films,” *IEEE Trans. Appl. Supercond.*, vol. 27, no. 4, p. Art. no. 8000405, 2017.

[111] N. Pompeo, K. Torokhtii, and E. Silva, “Surface impedance measurements in thin conducting films: Substrate and finite-thickness-induced uncertainties,” *I2MTC 2017 - 2017 IEEE Int. Instrum. Meas. Technol. Conf. Proc.*, no. 3, pp. 0–4, 2017.

[112] N. Klein *et al.*, “The effective microwave surface impedance of high T_c thin films,” *J. Appl. Phys.*, vol. 67, no. 11, pp. 6940–6945, 1990.

[113] N. Pompeo *et al.*, “Effect of $BaZrO_3$ Inclusions on the Microwave Surface Impedance of YBCO Films in a Magnetic Field,” *IEEE Trans. Appl. Supercond.*, vol. 19, no. 3, pp. 2917–2920, 2009.

[114] J. Halbritter, “Granular superconductors and their intrinsic and extrinsic surface impedance,” *J. Supercond.*, vol. 8, no. 6, pp. 691–703, 1995.

[115] N. Pompeo and E. Silva, “Reliable determination of vortex parameters from measurements of the microwave complex resistivity,” *Phys. Rev. B*, vol. 78, p. Art. no. 94503, 2008.

[116] D. C. Van Der Laan *et al.*, “Record current density of $344 Amm^{-2}$ at 4.2K and 17T in CORC ® accelerator magnet cables,” *Supercond. Sci. Technol.*, vol. 29, p. 55009, 2016.

[117] M. Miura, B. Maiorov, J. O. Willis, T. Kato, M. Sato, and T. Izumi, “The effects of density and size of $BaMO_3$ (M = Zr, Nb, Sn) nanoparticles on the vortex glassy and liquid phase in (Y, Gd) $Ba_2Cu_3O_y$ coated conductors,” *Supercond. Sci. Technol.*, vol. 35008, no. 26, 2013.

[118] S. A. Harrington *et al.*, “Self-assembled , rare earth tantalate pyrochlore nanoparticles for superior flux pinning in $YBa_2Cu_3O_{7-\delta}$ films,” *Supercond. Sci. Technol* , vol. 22, 22001.

[119] G. Ercolano *et al.*, "Strong correlated pinning at high growth rates in $YBa_2Cu_3O_{7-x}$ thin films with Ba_2YNbO_6 additions Strong correlated pinning at high growth rates in $YBa_2Cu_3O_{7-x}$ thin films," *J. Appl. Phys.*, vol. 116, p. 33915, 2014.

[120] F. Rizzo *et al.*, "Enhanced 77 K vortex-pinning in $YBa_2Cu_3O_{7-x}$ films with Ba_2YTaO_6 and mixed Ba_2YTaO_6+Ba_2YNbO_6 nano-columnar inclusions with irreversibility field to 11 T Enhanced 77 K vortex-pinning in $YBa_2Cu_3O_{7-x}$ films," *APL Mater.*, vol. 4, p. 61101, 2016.

[121] T. Puig *et al.*, "Vortex pinning in chemical solution nanostructured YBCO films," *Supercond. Sci. Technol.*, vol. 21, p. Art. no. 34008, 2008.

[122] V. K. Vlasko-Vlasov, L. A. Dorosinskii, A. A. Polyanskii, and V. I. Nikitenko, " Study of the influence of Individual Twin Boundaries on the Magnetic Flux Penetration," *Phys. Rev. Lett.*, vol. 72, no. 20, pp. 3246–3250, 1994.

[123] P. Paturi, M. Peurla, K. Nilsson, and J. Raittila, "Crystalline orientation and twin formation in YBCO thin films laser ablated from a nanocrystalline target," *Supercond. Sci. Technol.*, vol. 17, pp. 564–570, 2004.

[124] H. Safar *et al.*, "ab-plane anisotropy of the critical currents in twinned $YBa_2Cu_3O_{7-\delta}$ superconductors ab-plane anisotropy of the critical currents in twinned $YBa_2Cu_3O_{7-\delta}$ superconductors," *Appl. Phys. Lett.*, vol. 68, no. 13, pp. 1853–1855, 1996.

[125] R. J. Wijngaarden and R. Griessen, "Influence of twin planes in $YBa_2Cu_3O_7$ on magnetic flux movement and current flow," *Phys. Rev. B*, vol. 55, no. 5, pp. 3268–3275, 1997.

[126] T. Horide and K. Matsumoto, "Evaluation of vortex pinning across low angle grain boundary in $YBa_2Cu_3O_7$ film," *Appl. Phys. Lett.*, vol. 101, no. 11, p. 112604, 2012.

[127] Y. Zhu, M. Suenaga, J. Tafto, and D. O. Welch, "Variable nature of twin boundaries in $YBa_2Cu_3O_{7-\delta}$ and its alloys," *Phys. Rev. B*, vol. 44, no. 6, pp. 2871–2876, 1991.

[128] B. Maiorov *et al.*, "Synergetic combination of different types of defect to optimize pinning landscape using $BaZrO_3$-doped $YBa_2Cu_3O_7$," *Nat. Mater.*, vol. 8, no. 5, pp. 398–404, 2009.

[129] P. Paturi, "The vortex path model and angular dependence of Jc in thin YBCO films deposited from undoped and $BaZrO_3$ -doped targets," *Supercond. Sci. Technol.*, vol. 23, p. 25030, 2010.

[130] L. Civale *et al.*, "Identification of Intrinsic ab-Plane Pinning in $YBa_2Cu_3O_7$ Thin Films and Coated Conductors," *IEEE Trans. Appl. Supercond* , vol. 15, no. 2, pp. 2808–2811, 2005.

[131] A. Palau, R. Dinner, J. H. Durrell, and M. G. Blamire, "Vortex Breaking and Cutting in Type II Superconductors," *Phys. Rev. Lett.*, vol. 101, p. 97002, 2008.

[132] M. Sieger *et al.*, "Tailoring Microstructure and Superconducting Properties in Thick $BaHfO_3$ and $Ba_2Y(Nb/Ta)O_6$ Doped YBCO Films on Technical Templates," *IEEE Trans. Appl. Supercond.*, vol. 27, no. 4, 2017.

[133] N. Pompeo, V. Galluzzi, R. Rogai, G. Celentano, and E. Silva, "Change of strength of vortex pinning in YBCO due to $BaZrO_3$ inclusions," *Phys. C*, vol. 468, pp. 745–748, 2008.

[134] P. V. Gade, et al., "Conceptual Design of a Toroidal Field Coil for a Fusion Power Plant Using High Temperature Superconductors", *IEEE Trans. Appl. Supercond*, vol. 24, no. 3, p. Art. no. 4202705, 2014.

[135] G. Federici, et al., "European DEMO design strategy and consequences for materials", *Nucl. Fusion,* vol. 57, p. Art. no. 092002, 2017.

List of publications

1. A. Frolova, N. Pompeo, F. Rizzo, K. Torokhtii, A. Augieri, V. Galluzzi, A. Mancini, A. Vannozzi, A. Rufoloni, G. Celentano and E. Silva, "Critical Current And Vortex Flux Pinning Properties in $YBa_2Cu_3O_{7-x}$ Films with $Ba2YTaO_6$ + Ba_2YNbO_6 and $BaZrO_3$ Nano-inclusions By DC Transport And Microwave Measurements," IEEE Transactions on Applied Superconductivity, vol. 28 (4), 2018; doi: 10.1109/TASC.2018.2808438

2. Kostiantyn Torokhtii, Nicola Pompeo, Anna Frolova, Valentina Pinto, Achille Angrisani Armenio, Laura Piperno, Giuseppe Celentano, Traian Petrisor, Lelia Ciontea, Ramona B. Mos, Mircea Nasui, Giovanni Sotgiu, and Enrico Silva, "Microwave Measurements of Pinning Properties in Chemically Deposited YBCO/BZO Films", IEEE Transactions On Applied Superconductivity, vol. 27 (4), 2017. Art.ID 8000405; doi: 10.1109/TASC.2016.2634328

3. A.Frolova, N. Pompeo, F. Rizzo, K. Torokhtii, E. Silva, A. Augieri, G. Celentano, V. Pinto, A. Angrisani Armenio, A. Mancini, A. Rufoloni, A. Vannozzi, G. Sotgiu, L. Ciontea, and T. Petrisor, "Analysis of Transport Properties of MOD YBCO Films with $BaZrO_3$ as Artificial Vortex Pinning Centres," IEEE Transactions On Applied Superconductivity, vol. 26 (3), 2016. Art.ID 8001205; doi: 10.1109/TASC.2016.2542274

4. V. Pinto, A. Angrisani Armenio, L. Piperno, A. Mancini, F. Rizzo, A. Vannozzi, A. Rufoloni, A. Augieri, V. Galluzzi, A. Frolova, G. Sotgiu, E. Silva, F. Fabbri, R. Lamanna, and G. Celentano, "Aging of Precursor Solutions Used for YBCO Films Chemical Solution Deposition: Study of Mechanisms and Effects on Film Properties", IEEE Transactions On Applied Superconductivity, vol. 26 (3), 2016. Art.ID 7500405; doi: 10.1109/TASC.2016.2542587

Acknowledgments

I would like to acknowledge all the people that have been involved in this work.

First and foremost, I would like to express my sincere gratitude to my supervisor Prof. Enrico Silva for the continuous support of my Ph.D study and related research, for allowing me to grow professionally within his research group, for his patience, motivation, valuable discussions and immense knowledge. His guidance helped me in all the time of research and writing of this thesis. I could not have imagined having a better supervisor and mentor for my Ph.D study.

My sincere gratitude also goes to Dr. Giuseppe Celentano, for his constant help in the experimental work and for the constructive suggestions and discussions, for his guidance, great support and kind advice throughout my PhD research. It was a real privilege and honour for me to share of his exceptional scientific knowledge.

I also would like to thank to my co-tutor Dr. Nicola Pompeo for his constant support, availability and constructive suggestions, which were determinant for the accomplishment of the work presented in this thesis.

My special thanks go to Dr. Kostiantyn Torokhtii, for teaching me the miscrowave measurement technique, for providing so pleasurable and friendly working atmosphere, and for all the help and assistance that made it possible for me to adapt living in Rome.

I am also very grateful to Dr. Francesco Rizzo, who passed to me his knowledge and skills of the DC transport measurements and the data analysis, along with Dr. Andrea Augieri, who also contributed in teaching of this technique, for their valuable suggestions and comments on my research and the scientific papers. I also thank them for providing the PLD samples together with Dr. Valentina Galuzzi. Special

thanks to Dr. Valentina Pinto, Dr. Achille Angrisani Armenio and Laura Piperno for growing the MOD samples for this research.

I would also like to thank the whole Superconductivity Section of ENEA Research Center, and Dr. Antonio della Corte in particular, who provided me with an opportunity to join their research group and gave access to the laboratory and research facilities.

I thank all my colleagues at the ENEA Research Center for the stimulating discussions and suggestions, especially about the best “pasticcerie” in Rome. Completing this work would have been all the more difficult were it not for the support and friendship provided by them.

On a more personal note, I would like to thank my family and friends for their unconditional support, encouragement and love without which I would not have come this far. Finally, I would like to thank my other half. Words cannot express my gratitude for everything you have done. Thank you for accompanying me on this adventure and I look forward to our next one!